Neutron Scattering Studies of Excitations in Spin Chains

Author(s):
Hirtenlechner, Eva E.

Publication Date:
2014

Permanent Link:

https://doi.org/10.3929/ethz-a-010398248 →

DISS. ETH No. 22303

Neutron Scattering Studies of Excitations in Spin Chains

A thesis submitted to attain the degree of
DOCTOR OF SCIENCES of ETH ZURICH
Dr. sc. ETH Zurich

presented by
Eva Elisabeth Hirtenlechner

MSc Physics ETH

born January 01, 1987
citizen of
Austria

accepted on the recommendation of
Prof. Dr. Joël Mesot, examiner
Prof. Dr. Christian Rüegg, co-examiner
Dr. Mechthild Enderle, co-examiner

2014

To my Dad,

who inspired my curiosity in nature

and encouraged me to be the best I can be

Abstract

Many phenomena in magnetism can be described using classical models, yet magnetism is a quantum mechanical effect. In addition to thermal fluctuations, quantum fluctuations arise due to the quantum uncertainty of the ground state. These fluctuations are enhanced by low dimensionality and low spin. Spin chains show interesting excitations associated with quasiparticles. Model materials for spin chains can be realized in compounds where the interchain interactions are weak enough. This thesis presents neutron scattering studies of two model materials for spin chains with different spin symmetry.

The spin-$\frac{1}{2}$ Heisenberg antiferromagnetic chain $\mathbf{CuSO_4{*}5D_2O}$ has a main exchange of $J \sim 3$ K, which permits to study its excitation spectrum up to temperatures of ten times the exchange. The spin-$\frac{1}{2}$ Heisenberg magnet has been studied widely both theoretically and experimentally. The excitation spectrum of the spin-$\frac{1}{2}$ Heisenberg antiferromagnet consists of quasiparticles called spinons, and calculations for it exist for T = 0 and as a function of temperature. A quantitative comparison between experimental data and theoretical models across a range of temperatures is presented. The excitation spectrum of $CuSO_4{*}5D_2O$ is excellently described by the excitation spectrum of a spin-$\frac{1}{2}$ Heisenberg antiferromagnetic chain at finite temperatures. Energy-temperature scaling is observed at temperatures up to $2J$. For these temperatures the Luttinger liquid description of the spin-$\frac{1}{2}$ Heisenberg antiferromagnetic chain is valid. A spinon continuum is confirmed at all measured temperatures. Therefore, even at ten times the main exchange ($T \approx 10\ J$), $CuSO_4{*}5D_2O$ shows the behavior of a quantum magnet, and not of a classical system at infinite temperatures, for which one would expect single spin flips.

The Ising chain is one of the most studied models in magnetism, one model compound for it is $\mathbf{RbCoCl_3}$. Optical spectroscopy measurements suggest a lower gap than for similar compounds, which makes it better suited for high resolution neutron spectroscopy. Magnetic correlations along the chains arise in $RbCoCl_3$ below 80 K. A gapped continuum is observed, which arises from isolated antiferromagnetic Ising chains. Below the first magnetic ordering temperature $T_{N_1} \approx 28$ K bound states are observed, which arise due to correlations which form between the chains. Strong diffuse scattering leads to the conclusion that disorder is still present. At the second magnetic ordering transition, at $T_{N_2} \approx 14$ K, the bound states split as the correlations between the chains change. Fits indicate that the correlations change continuously as a function of temperature. Above T_{N_2} the excitation spectrum of $RbCoCl_3$ can be described by a spin-$\frac{1}{2}$ Ising chain with an XY-component which is treated as a perturbation. Below T_{N_2} the main features are reproduced correctly, but deviations from the details indicate that additional terms in the Hamiltonian may be necessary.

This thesis was carried out at the Institut Laue-Langevin, the Laboratory for Neutron Scattering and Imaging at the Paul Scherrer Institute and ETH Zürich.

Kurzfassung

Obwohl viele Phänomene im Magnetismus anhand klassischer Modelle beschrieben werden können ist Magnetismus ein quantenmechanischer Effekt. Zusätzlich zu thermischen Fluktuationen können Quantenfluktuationen auftreten, welche von der Unsicherheit des Grundzustandes herrühren. Diese Fluktuationen werden durch niedrige Dimensionalität und Spinquantenzahl verstärkt. Spinketten zeigen interessante Anregungen, die in Zusammenhang mit Quasiteilchen stehen. Modellmaterialien für Spinketten können in Verbindungen mit ausreichend schwacher Zwischenkettenwechselwirkung realisiert werden. Diese Doktorarbeit präsentiert die Ergebnisse der Untersuchung zweier Modellmaterialien für Spinketten unterschiedlicher Spinsymmetrie mittels Neutronenstreuung.

Der eindimensionalen Spin-$\frac{1}{2}$ Heisenberg-Antiferromagnet $\mathbf{CuSO_4{*}5D_2O}$ hat eine Wechselwirkungsenergie von $J \sim 3$ K, was Untersuchungen des Anregungsspektrums bis zu Temperaturen von zehn mal der Wechselwirkungsenergie ($T \approx 10\ J$) möglich macht. Spin-$\frac{1}{2}$ Heisenberg-Magnete wurden theoretisch und experimentell umfassend untersucht. Das Anregungsspektrum eines Spin-$\frac{1}{2}$ Heisenberg Antiferromagneten besteht aus Quasiteilchen die Spinonen genannt werden, und theoretische Ergebnisse dafür existieren für $T = 0$ und als Funktion der Temperatur. Ein vollständiger quantitativer Vergleich zwischen experimentellen Daten und theoretischen Modellen wird präsentiert. Das Anregungsspektrum von $CuSO_4{*}5D_2O$ wird hervorragend durch das Anregungsspektrum einer Spin-$\frac{1}{2}$ Heisenberg antiferromagnetischen Kette bei endlichen Temperaturen beschrieben. Energie-Temperatur Scaling wird bis $2J$ beobachtet. In diesem Bereich ist die Beschreibung der Spin-$\frac{1}{2}$ Heisenberg antiferromagnetischen Kette als Luttinger-Flüssigkeit gültig. Ein Spinonenkontinuum ist bei allen gemessen Temperaturen vorhanden. Deshalb zeigt $CuSO_4{*}5D_2O$ sogar bei zehn mal der Wechselwirkung ($T \approx 10\ J$) das Verhalten eines Quantenmagneten, und nicht das eines klassischen Systems bei unendlichen Temperaturen, für welches man das Umklappen einzelner Spins erwarten würde.

Die Isingkette ist eines der wohl am meisten untersuchten Modelle des Magnetismus, eine Modellverbindung dafür ist $\mathbf{RbCoCl_3}$. Optische Spektroskopie zeigt eine kleinere Energielücke als für ähnliche Verbindungen, was dieses Material besser geeignet für hochauflösende Neutronenspektroskopie macht. Unter 80 K treten magnetische Korrelationen entlang der Ketten auf. Ein Kontinuum mit einer Lücke wird beobachtet, welches von isolierten antiferromagnetischen Ising-Ketten herrührt. Unterhalb der ersten magnetischen Ordnungstemperatur $T_{N_1} \approx 28$ K werden gebundene Zustände beobachtet, welche aus den Korrelationen zwischen den Ketten resultieren. Starke diffuse Streuung führt zu der Schlussfolgerung dass noch immer Unordnung vorhanden ist. Beim zweiten magnetischen Ordnungsübergang bei $T_{N_2} \approx 14$ K spalten sich die gebundenen Zustände auf, da sich die Korrelationen zwischen den Ketten ändern. Fits deuten darauf hin dass sich die Korrelationen kontinuierlich als Funktion der Temperatur ändern. Oberhalb von T_{N_2} kann das Anregungsspektrum

von $RbCoCl_3$ durch eine Spin-$\frac{1}{2}$ Isingkette mit einer XY-Komponente, welche als Störung behandelt wird, beschrieben werden. Unterhalb von T_{N_2} werden die groben Eigenschaften korrekt wiedergegeben, Abweichungen von Details deuten aber darauf hin, dass mehr Terme im Hamiltonian gebraucht werden.

Diese Doktorarbeit wurde am Institut Laue-Langevin, dem Labor für Neutronenstreuung und Imaging am Paul Scherrer Institut und der ETH Zürich durchgeführt.

Contents

List of Figures

List of Tables

Introduction

Spin chains are particularly suited to study manifestations of quantum mechanics at a macroscopic level, since they are "simple" enough to be accessible for theoretical analysis and at the same time show a wide variation of interesting behavior. Ideal spin chains do not show order, but have an exotic excitation spectrum consisting of fractional excitations. The isotropic Heisenberg Hamiltonian is the basis for such studies. The low dimensionality and the quantum nature of spin-$\frac{1}{2}$ enhance quantum fluctuations, which are present even at T = 0. These fluctuations suppress order, and enhancing them can lead to quantum phase transitions. These transitions take place at quantum critical points, and are driven by parameters other than temperature, e.g. by pressure or magnetic field. One of the simplest examples of a quantum phase transition is the Ising chain in a transverse magnetic field [1].

Neutron scattering is a powerful probe to study the spin correlations and excitations in model materials. Neutrons are uncharged, a bulk probe, and are scattered by nuclear forces. The neutron energy is also of the same order as many excitations in condensed matter. Furthermore, neutrons have a magnetic moment so that they also interact with the magnetic moment of unpaired electrons in atoms. Neutrons are specially suited to investigate the magnetic properties of materials, since they directly capture the Fourier transformation of the spin-spin correlation function, and inelastic neutron scattering reflects the correlated fluctuations of a sample [2].

It is a big challenge to find good model materials for spin chains. In real materials, one deviation from the ideal one-dimensional model is a weak magnetic exchange J' in the other two dimensions. This deviation from ideal one-dimensionality can lead to three-dimensional order at low temperatures. The ratio J'/J can be used as a measure of the low-dimensionality of a system. For temperature dependent studies, the main exchange J should be of a size that enables studies over a big enough temperature range without needing to worry about crystallographic phase transitions or thermal expansion. Crystal anisotropy leads to deviations from the isotropic Heisenberg model. It can lower spin symmetry, and lead to the XY- and Ising-cases.

Inelastic neutron scattering requires big single crystals. The feasibility of growing such crystals is an additional constraint on possible model compounds. Only a few "simple" and "pure" model materials for quantum magnets are known [3].

$CuSO_4$*$5D_2O$ is an excellent model material for the spin-$\frac{1}{2}$ Heisenberg antiferro-

magnetic chain. It has spin-$\frac{1}{2}$ and low anisotropy. The low ratio of interchain to in-chain interaction makes it very nearly one-dimensional, and its low main exchange $J \sim 3$ K allows measurements up to temperatures of 10 times the main exchange without having to worry about thermal expansion effects. In this thesis the continuous excitation spectrum of $CuSO_4$*$5D_2O$, which consists of fractional excitations called spinons, is studied as a function of temperature.

The second model material studied in this thesis is $RbCoCl_3$. In this compound large crystal field anisotropy reduces spin dimensionality. $RbCoCl_3$ is an Ising-like quasi-one dimensional compound. It has been studied less than related compounds, and optical spectroscopy predicted a lower energy scale. Studying the excitation spectrum of $RbCoCl_3$ as a function of temperature helps to determine the Hamiltonian and the corresponding parameters, describe the bound states arising in the ordered phase, and answering the question if the quantum critical point can be reached experimentally.

Thesis Outline

This thesis is composed of five chapters.

Chapter 1 is a brief introduction to the theory of magnetism and introduces the concept of quantum magnetism.

Chapter 2 is an introduction to neutron scattering, the technique used in this thesis, and presents the types of neutron scattering instruments used.

Chapter 3 is a study of the excitation spectrum of the spin-$\frac{1}{2}$ Heisenberg antiferromagnetic chain $CuSO_4$*$5D_2O$ as a function of temperature. It also contains an introduction to the theory of excitations in a Heisenberg chain.

Chapter 4 is a study of the magnetic structure and excitations of the Ising-like antiferromagnetic chain $RbCoCl_3$. In this chapter also the theory of excitations in Ising-like antiferromagnetic chains is treated.

Chapter 5 contains a summary and outlook.

Chapter 1

Magnetism

Magnetism is a fundamental quantum mechanical effect, yet many observed phenomena can be understood using classical models. In the case of low-dimensional and frustrated spin-$\frac{1}{2}$ antiferromagnets, novel types of macroscopic ground states develop due to the quantum nature of the spin-$\frac{1}{2}$. These are entangled ground states without an ordered moment, but with well-defined magnetic excitations, and cannot be explained by classical models.

This chapter is a short introduction to magnetism. Before quantum magnetism is introduced, the origin of the magnetic moments, magnetic exchange and order is described.

This chapter follows the book by Blundell [4]. This book is the main source for this chapter, and where no other citation is given in this chapter, the book by Blundell was used.

1.1 A short introduction to magnetism

The most fundamental object in magnetism is the magnetic moment. A current I going around a loop of area $d\mathbf{S}$ induces a magnetic moment $\boldsymbol{\mu}$:

$$\boldsymbol{\mu} = \int d\boldsymbol{\mu} = I \int d\mathbf{S} = \gamma \mathbf{L},$$

where γ is the gyromagnetic ratio. The gyromagnetic ratio for the electron is $\gamma = -\frac{e}{2m_e}$. A current going around a loop can be seen as a charge (e.g. an electron) moving on an orbit which coincides with this loop. $\mathbf{L}$ is the angular momentum of such a charge. Since the magnetic moment is perpendicular to the plane of the loop, it is either parallel or antiparallel to the angular momentum of the charge going around the loop. The magnetic moment of the electron is called the Bohr magneton and is given by

$$\mu_B = \frac{e\hbar}{2m_e} = 9.274 \times 10^{-24} \mathrm{Am}^2,$$

Since the electron has a negative charge, its magnetic moment is antiparallel to its angular momentum. The component of the angular momentum along a fixed axis (usually one chooses the z-axis) is $m_{\mathrm{l}}\hbar$, which is the eigenvalue of the z-component of $\mathbf{L}$. Then the magnetic moment along the z-axis is $\mu_{\mathrm{l}} = -m_{\mathrm{l}}\mu_{\mathrm{B}}$.

The electron also possesses an intrinsic magnetic moment which is called the "spin", characterized by the spin quantum number s. For electrons s is equal to $\frac{1}{2}$. Since the value of any component of the angular momentum can only take $2s+1$ possible values, the component of angular momentum along a particular axis for $s = \frac{1}{2}$ is $\frac{\hbar}{2}$ or $-\frac{\hbar}{2}$. These alternatives are often referred to as "up"and "down". The magnetic moment associated with the spin angular moment is $\mu_{\mathrm{s}} = -g\mu_{\mathrm{B}}m_{\mathrm{s}}$, where g is a constant close to 2 called the g-factor. The energy of an electron in a magnetic field B is

$$E = g\mu_{\mathrm{B}}m_{\mathrm{s}}B = -\mu_{\mathrm{s}}B.$$

This means that the energy levels of an electron in a magnetic field are split (Zeeman splitting).

The total spin and orbital angular momentum, $\mathbf{S} = \sum_i \mathbf{s}_i$ and $\mathbf{L} = \sum_i \mathbf{l}_i$, are zero for filled electron shells. The spin-orbit interaction couples the spin and orbital angular momentum to the total angular momentum. The ground state configuration of electrons in an atom is predicted by Hund's rules. Hund's rules make no prediction about excited states. Also, the ground state may differ because of the environment of the magnetic ion.

Magnetic susceptibility

The magnetization $\mathbf{M}$ of a material and the applied magnetic field $\mathbf{H}$ are related by the magnetic susceptibility χ. It is a measure of the ability of a material to become magnetized. If $\chi < 0$, a material is diamagnetic. This means that an applied magnetic field induces a magnetic moment which opposes the applied field. This effect is weakly present in all materials. A material with $\chi > 0$ is paramagnetic. This means that an applied magnetic field aligns non-zero magnetic moments in the material. Paramagnetism is usually much stronger than diamagnetism.

Magnetic exchange

To establish long range order, a magnetic exchange J is needed. If one considers the coupling between two electrons, their combined wave functions can either be a spin singlet state with $s = 0$, or a spin triplet state with $s = 1$. The exchange integral

$$J = -\frac{\mathrm{E_S} - \mathrm{E_T}}{2} = -\int \phi_1^*(\mathbf{r}_1)\phi_2^*(\mathbf{r}_2)\mathrm{H}\phi_1(\mathbf{r}_2)\phi_2(\mathbf{r}_1)d\mathbf{r}_1 d\mathbf{r}_2, \tag{1.1}$$

where H is an effective Hamiltonian given in equation 1.2, ϕ_1 and ϕ_2 are the wave functions of the two electrons, and $\mathbf{r}_1$ and $\mathbf{r}_2$ their spatial coordinates, calculates the energy difference between the energy of the spin singlet state $\mathrm{E_S}$ and the spin triplet case $\mathrm{E_T}$.

The difference between a singlet and a triplet state can be parametrized using $\mathbf{S}_1 \cdot \mathbf{S}_2$, and the Hamiltonian can be written as

$$\mathrm{H} = \frac{1}{4}\left(\mathrm{E_S} + 3\mathrm{E_T}\right) - \left(\mathrm{E_S} - \mathrm{E_T}\right)\mathbf{S}_1 \cdot \mathbf{S}_2. \tag{1.2}$$

Using equation (1.1) the spin-dependent part of the Hamiltonian can be simplified to

$$\mathrm{H} = 2J\mathbf{S}_1 \cdot \mathbf{S}_2. \tag{1.3}$$

With the interaction in (1.3) applied to all neighboring spins, one obtains the Heisenberg Hamiltonian

$$\mathrm{H} = \sum_{i,j} J_{i,j}\mathbf{S}_i \cdot \mathbf{S}_j,$$

where $J_{i,j}$ is the exchange constant between two spins i and j. A negative J leads to alignment of spins (where the triplet state $s = 1$ is favored), and a positive J leads to anti-alignment of spins (where the singlet state $s = 0$ is favored). There are several kinds of exchange interactions: **Direct exchange** arises from the overlap of neighboring magnetic orbitals. Often there is not enough overlap between neighboring magnetic orbitals, so some kind of indirect exchange is needed. **Superexchange** is an indirect exchange between non-neighboring magnetic ions mediated by non-magnetic ions. Because superexchange depends strongly on the overlap of the orbitals between the magnetic and non-magnetic ions, its sign depends on the angle of the bond. The **RKKY interaction**, or itinerant exchange, occurs in metals. A localized magnetic moment polarizes conduction electrons, which polarize a neighboring magnetic moment. **Double exchange** occurs in systems with mixed valency. If electrons hop between magnetic ions, it is favorable for the spins to be aligned. The **Dzyaloshinsky-Moriya (DM) interaction** is an exchange interaction between the excited states of one ion and the ground state of another ion. It usually gives rise to a small ferromagnetic component in an antiferromagnetically ordered system.

Magnetic order

With decreasing temperature thermal fluctuations become smaller, and below a characteristic temperature the magnetic interactions are strong enough to establish a magnetic long range order. Some magnetic structures are: **Ferromagnetism**: $J < 0$. In this state all spins are aligned parallel. This causes a spontaneous magneti-

zation even in the absence of an external magnetic field. **Antiferromagnetism**: $J > 0$. In this state, the spins are aligned antiparallel, and no net magnetization occurs. It can be considered as consisting of two magnetic sublattices where the spins on each sublattice are parallel to each other, but the magnetizations of the two sublattices are opposite. A special case of antiferromagnetism is **ferrimagnetism**. Here the two sublattices have unequal magnetic moments, and the system has a net magnetization. Another ordered structure is **helimagnetism**, where spins are aligned neither parallel nor antiparallel, but with an angle $\neq \pi$ between them.

Order parameters

When the system enters an ordered phase at a temperature T_C, it is said to undergo a phase transition. Often a certain physical property, called the order parameter, is different above and below T_C. The order parameter is zero for $T > T_C$ and non-zero for $T < T_C$. The order parameter for ferromagnetism is the magnetization.

The order parameter has a dimensionality D, which is in this case the dimensionality of the spins themselves. It is important not to confuse the dimensionality d of the lattice and D of the order parameter.

Systems with $D = 3$ are called Heisenberg magnets, $D = 2$ are called XY magnets, and $D = 1$ are called Ising magnets. For Ising systems the Hamiltonian is $H = \sum_{i,j} J_{i,j} S_i^z S_j^z$.

Spin waves

Spin waves are collective excitations in simple, long-range ordered three dimensional Heisenberg magnets which are quantized as magnons. Spin waves can be described by linear spin wave theory [5, 6]. Magnons are Goldstone bosons and have spin-1 [5, 7, 8]. This means that a single magnon can interact with a neutron in an inelastic neutron scattering experiment [4]. Magnons were first observed by Brockhouse [9] using neutron scattering.

1.2 Quantum magnetism

Even though many phenomena in magnetism can be understood using classical models, it is a quantum mechanical effect. In addition to thermal fluctuations, quantum fluctuations need to be considered. Quantum fluctuations arise from the quantum uncertainty of the ground state, and can be enhanced by, for example, low spin, low dimensionality, or frustration [1]. The materials studied in this thesis have low spin and low dimensionality, and are examples of quantum magnets.

Low dimensional magnetism

The Mermin-Wagner theorem states that for dimensions smaller than three, thermal fluctuations prohibit magnetic long range order in an isotropic system at finite temperatures [10]. The one dimensional spin-$\frac{1}{2}$ Heisenberg antiferromagnetic chain shows no long range order even at 0 K. What makes one dimensional systems interesting are their excitations.

One dimensional magnetic systems, also known as spin chains, can be realized in crystals with sufficiently weak interchain interaction. These can be Heisenberg, XY or Ising-systems. These systems show three dimensional order at finite temperatures if the interchain interactions are strong enough. Still, above the temperature where three dimensional order sets in, the behavior of one dimensional magnetic systems can be observed in spin chain materials. An overview of some magnetic model systems is given by de Jongh and Miedema in reference [11].

The spin number and spin dimensionality depends on the ion carrying the unpaired spin. A recent example is $SrX_2V_2O_8$ where X = Co, Mn. While $SrCo_2V_2O_8$ is an antiferromagnetic Ising chain with effective spin-$\frac{1}{2}$, $SrMn_2V_2O_8$ is a Heisenberg antiferromagnetic chain with spin-$\frac{5}{2}$ [12]. Cobalt is a good source for Ising like interactions. Other Ising chains are for example members of the $ACoX_3$ family with A = Rb, Cs, Tl and X = Br, Cl [11]. Ising chains are interesting, because an Ising chain in a transverse magnetic field is a simple realization of a quantum phase transition. One example is the ferromagnetic Ising chain $CoNb_2O_6$[13] discussed in the following section about quantum phase transitions.

Examples of spin-$\frac{1}{2}$ Heisenberg antiferromagnetic chains are $KCuF_3$ [14, 15], $CuCl_2$*$2N(C_5D_5)$ [16, 17] or $SrCuO_2$ [18, 19]. The excitation spectra of these chain materials have been probed using neutron scattering.

Quantum phase transitions

When phase transitions are driven by temperature, thermal fluctuations destroy the order. But it is also possible that phase transitions occur at zero temperature. Such phase transitions are called quantum phase transitions, and are driven by variables other than temperature, e.g. by pressure or magnetic field. The fluctuations which destroy the order are then quantum fluctuations. A quantum critical point is the point where a quantum phase transition will occur. The probably simplest theoretical model for a quantum phase transition is the Ising chain in a magnetic field transverse to the Ising axis [20], for example the ferromagnetic Ising chain $CoNb_2O_6$ [13]. At a certain critical field strength the magnetic order is destroyed, and the spins align with the magnetic field. In this example the critical field is the quantum critical point.

The dimer system $TlCuCl_3$ is an example where a quantum phase transition can be induced by pressure [21]. Recently spin excitations across the quantum critical point have been studied using neutron scattering, where it was observed that quan-

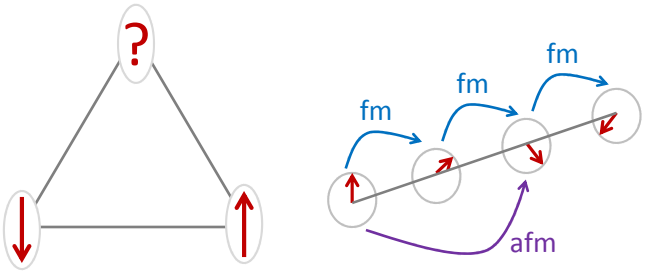

Figure 1.1: **Two examples of frustration.** Left: geometric frustration on a triangular antiferromagnetic lattice. Right: Frustration due to competing nearest neighbor and next nearest neighbor exchange on a spin chain.

tum and thermal fluctuations behave "*largely independently near a quantum critical point*" [22].

An example of a two-dimensional system is the frustrated spin ladder $BiCu_2PO_6$. In this material a quantum phase transition can be triggered by introducing non-magnetic impurities, i.e. substituting the Cu^{2+} (S = 1/2) ions by Zn^{2+} (S = 0) [23].

Other examples of systems undergoing quantum phase transitions are cuprate superconductors [24] and the transition from a superfluid to a Mott-insulator [25].

Frustration

In some lattices the ground state is not unique, because it is impossible to satisfy all interactions. Geometric frustration arises due to the geometry of the lattice, a common example for geometric frustration is a triangular lattice with antiferromagnetic nearest neighbor interaction, see Figure 1.1. Examples are $CuFeO_2$ [26–28] or $CsVCl_3$ [29–32] and VX_2 (X = Cl,Br,I) [29, 33]. There exists no ground state which satisfies all constraints [4]. Frustration can also occur in three dimensions. One example is the pyrochlore lattice with nearest neighbor antiferromagnetic interactions [34], e.g. in $ZnCr_2O_4$ [35, 36].

Another well known example for geometric frustration is the Kagome lattice with antiferromagnetic interactions as e.g. $SrCr_8Ga_4O_{19}$ [37] or herbertsmithite $ZnCu_3(OH)_6Cl_2$ [38], where recently a spinon continuum was observed using neutron scattering [39].

Frustration can also arise due to competing nearest and next nearest neighbor interactions, as is the case for a spin chain with ferromagnetic nearest neighbor and antiferromagnetic next nearest neighbor coupling, see Figure 1.1. This may lead to a helical structure as for example in $LiCuVO_4$ [40], or the Heisenberg two-leg ladder $BiCu_2PO_6$ which is frustrated by strong antiferromagnetic next nearest neighbor coupling along the legs [41].

Frustration can lower the ordering temperature and even suppress long range order. It has been connected to spin ice, as in the pyrochlore $Dy_2Ti_2O_7$ [42]. Frustrated

materials often show non-collinear configurations at low temperatures, which makes them good candidates for magnetoelectric materials. Examples are $CuFeO_2$ [43], or $TbMnO_3$ [44, 45] and $LiCuVO_4$ [46].

Excitations in spin chains

Spin chains only show order if the interchain interactions are strong enough. What makes them interesting is not their ground state but their excitations. In Ising chains an excitation is associated with flipping a spin. Flipping a spin creates two domain walls, one on each side of the flipped spin.

The excitation spectrum does not only depend on the dimensionality of the spin, but also on the spin quantum number. Haldane predicted that one dimensional Heisenberg antiferromagnets of integer spin have an excitation gap, while the excitation spectrum of a one-dimensional half-integer spin Heisenberg antiferromagnet is gapless [47, 48]. This Haldane gap has been observed in the spin-1 antiferromagnetic Heisenberg chain $CsNiCl_3$ using neutron scattering [49, 50]. In this compound a multiparticle continuum has been observed using unpolarized neutron scattering [51, 52]. The origin of this continuum is still under investigation.

The excitation spectra of a spin-$\frac{1}{2}$ Heisenberg antiferromagnetic chain are not gapped. Haldane stated that all one dimensional magnets with a gapless linear spectrum are Tomonaga-Luttinger liquids (TLL) [53]. A Tomonaga-Luttinger liquid (often called Luttinger liquid) is a theoretical model which describes interacting fermions in a one dimensional system [54, 55]. The ground state of a TLL is quantum critical, and TLL theory predicts universal properties for the great variety of one-dimensional systems. The physical properties measured in an experiment can be calculated using conformal field theory. But these theoretical predictions are only valid at sufficiently low energy and temperature [56, 57]. It was shown by Lake *et al.* that the Heisenberg spin-$\frac{1}{2}$ antiferromagnetic chain $KCuF_3$ can be described as a Luttinger liquid for an extensive range of temperature, energy and momentum. The work on $KCuF_3$ shows the limits of conformal field theory, and how the dynamics of this spin-$\frac{1}{2}$ Heisenberg antiferromagnetic chain are captured by the description as a TLL [57, 58].

On the other hand the excitation spectra of Ising chains are gapped, independent of the spin quantum number, because of the anisotropy. Such a gapped spectrum was for example observed in the Ising like chain $CsCoCl_3$ [59, 60]. These excitations are called solitons.

Solitons

The domain wall introduced above is a "semi-classical"picture, and if this domain wall satisfies certain conditions it is called a soliton. "*Essentially, solitons are quantized excitations of a classical, continuous system which are not scattered by* `[other]` *solitons or other quasi-particles: they can be retarded or accelerated during the col-*

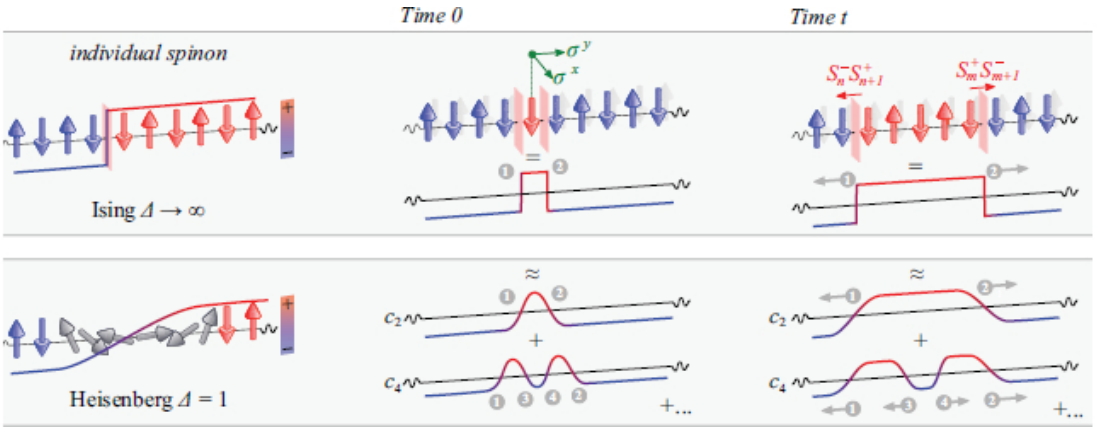

Figure 1.2: **Schematic representations of spinons** in a spin-$\frac{1}{2}$ antiferromagnetic Ising and Heisenberg chain. An incident neutron acts on the singlet state and flips a spin which is surrounded by two domain walls. Each of these walls is a spinon carrying spin-$\frac{1}{2}$. For better visibility in the Heisenberg case the two- and four spinon cases are drawn separately and labeled by $c_{2,4}$. Δ is the anisotropy, $\sigma^{x,y}$ are the Pauli spin matrices. Figure courtesy of M. Mourigal [73].

lision, but the velocity (and shape) at the end of the collision is the same as before " [61]. Solitons have been studied in several Ising chains, amongst others in several members of the family $ACoX_3$, with A = {Rb, Cs, Tl} and X = {Br, Cl}, for example $CsCoBr_3$ [59, 62–64], $CsCoCl_3$ [59, 60] and $TlCoCl_3$ [65–67]. The in-chain coupling of these compounds is around $2J$ = 12.8 - 14.7 meV. In this thesis another member of this family, $RbCoCl_3$, is studied. It has been studied less, and optical spectroscopy measurements have indicated the energy scale $2J$ to be lower [3]. The lower energy scale of $RbCoCl_3$, and the better resolution of high resolution neutron spectroscopy, is expected to lead to a better understanding of the excitation spectrum of the Ising-like antiferromagnetic chain. Solitons are studied in the spin-$\frac{1}{2}$ Ising chain $RbCoCl_3$ in chapter 4, where a more thorough description of solitons is given.

Spinons

Spinons are a special case of solitons reserved for spin-$\frac{1}{2}$ chains [1]. Each of these domain walls corresponds to a spinon carrying spin-$\frac{1}{2}$. Spinons are semions [2] [71, 72].

In Heisenberg spin chains spinons are gapless. The kink is not as sharp as for an Ising chain. Therefore, in the Heisenberg limit the spin flip consists of a series of

[1]The quasiparticles arising from excitations in the spin-$\frac{1}{2}$ Ising-like chain $RbCoCl_3$ are also spinons, but in order to conform with the terminology used in the literature and avoid confusion the term solitons is used for these excitations.

[2]Semions are anyons. Anyons have fractional statistics, so they are neither fermions nor bosons. Anyons are quasiparticles which only occur in physical systems with less than three dimensions [68–70].

two, four and higher even numbered spinons [72]. A sketch of spinons in the Ising and Heisenberg limit is shown in Figure 1.2.

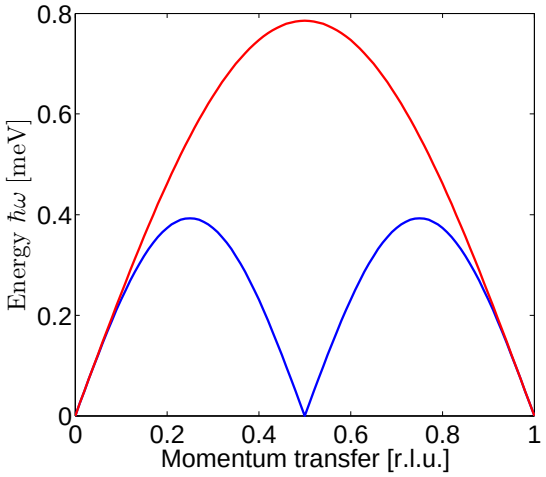

Figure 1.3: **Boundaries for the two-spinon continuum**. Because only pairs of spinons can be observed by neutron scattering, a continuum between the lower boundary (blue) and upper boundary (red) is observed [4, 74].

An inelastic magnetic neutron scattering experiment gives rise to excitations with a total spin of 1, so two spinons interact with a neutron in an inelastic neutron scattering experiment. This means that only pairs of spinons can be observed by neutron scattering. Therefore experimental data show a continuum between the lower and upper two-spinon boundaries $\hbar\omega = \frac{\pi}{2}\left|J\sin(2\pi q)\right|$ and $\hbar\omega = \pi\left|J\sin\left(\frac{2\pi q}{2}\right)\right|$ shown in Figure 1.3 [4, 74].

Spinons are, for example, the basic excitations of $KCuF_3$ and have been studied at finite temperatures up to 200 K, which is about half the in-chain coupling [58, 75]. But spinons have been observed before, a continuum assumed to arise from spinon excitations has already been observed in the seventies in the spin-$\frac{1}{2}$ Heisenberg antiferromagnetic chain $CuCl_2$*$2N(C_5D_5)$ [16, 17].

Mourigal *et al.* established, by absolute normalization of their data and by comparing them to the excitation spectrum of the two- and four-spinon structure factor calculated by Caux [76], that two- and four-spinon states account for 99(8) % of the measured spectral weight [72]. These measurements were done at 100 mK.

In this thesis the excitation spectrum of $CuSO_4$*$5D_2O$ is studied at temperatures from the Millikelvin range up to ten times the exchange. The results by Mourigal *et al.* allow a normalization of the data even at finite temperatures, thus enabling the quantitative and qualitative comparison of experimental data with theoretical calculations. Additional advantages of $CuSO_4$*$5D_2O$ over other known model systems for the spin-$\frac{1}{2}$ Heisenberg antiferromagnetic chain are its good one dimensionality, low main exchange and vanishing anisotropy [11, 72, 77, 78]. Spinons in $CuSO_4$*$5D_2O$ are studied in chapter 3, there exact calculations for the excitation spectrum of the

spin-$\frac{1}{2}$ Heisenberg antiferromagnetic chain are introduced as well.

In this thesis the excitation spectrum of two spin-$\frac{1}{2}$ chains is studied using neutron scattering.
$CuSO_4$*5D_2O is an excellent model material for the spin-$\frac{1}{2}$ Heisenberg antiferromagnetic chain. Its low exchange interaction permits measurements at temperatures up to ten times the exchange. Earlier results by Mourigal *et al.* [72] make absolute comparison between experiment and theory possible. The excitation spectrum of $CuSO_4$*5D_2O, which consists of fractional excitations called spinons, is studied as a function of temperature.
$RbCoCl_3$ is a quasi-one dimensional spin-$\frac{1}{2}$ Ising system. It has been studied less than other members of the $ACoX_3$ family, and optical spectroscopy measurements indicate a lower energy scale $2J$. A lower energy scale is connected to a lower critical magnetic field. The magnetic structure and excitation spectrum of $RbCoCl_3$ are studied. Open questions are if the energy scale is low enough to reach the quantum critical point, and to understand the excitation spectrum, especially the bound states arising in the ordered phase.

Chapter 2

Neutron scattering

Neutrons carry no electric charge and are therefore a good bulk probe. Thermal neutrons, at 293 K, have an energy, 25.2 meV, and a wavelength, $\lambda = 1.8$ Å, similar to many excitations in condensed matter. Neutron scattering can discriminate between isotopes of the same element, and is sensitive to light atoms, even in the vicinity of heavier ones. Because of their magnetic moment, neutrons are well suited to study magnetic materials and can also be polarized.

The main disadvantage of neutron scattering is the low available neutron flux. This results in long counting times and the need for large single crystals as samples.

This chapter is inspired by books about neutron scattering by Lovesey [79, 80], Squires [81] and Sivia [82]. These books also offer more detail than this short introduction.

2.1 Neutron Scattering Cross-Section

In a neutron scattering experiment, an incoming neutron with wave vector $\mathbf{k}_i$ is scattered into a final state with wave vector $\mathbf{k}_f$. The scattering process is illustrated by the scattering triangle shown in Figure 2.1.

The wave vector transfer $\mathbf{Q}$ is given by

$$\mathbf{Q} = \mathbf{k}_i - \mathbf{k}_f, \qquad Q^2 = k_i^2 + k_f^2 - 2cos(2\theta)k_i k_f.$$

For elastic scattering there is no energy transfer between sample and neutron, and $\hbar\omega = 0$ and $\mathrm{k}_i = \mathrm{k}_f$. For inelastic scattering the energy transfer is given by

$$\hbar\omega = E_i - E_f = \frac{(\hbar k_i)^2}{2m_n} - \frac{(\hbar k_f)^2}{2m_n},$$

where m_n is the mass of the neutron. The fundamental quantity measured in such an experiment, the cross section σ, is defined as the rate of scattered neutrons per unit of incident flux Ψ.

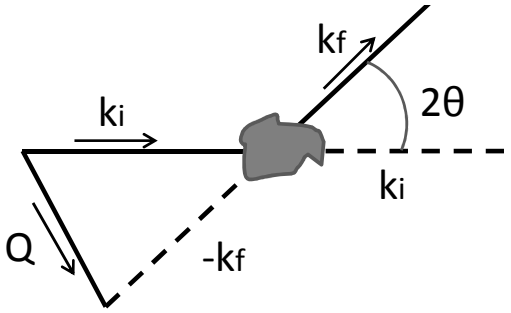

Figure 2.1: **The scattering process.** An incoming neutron with wave vector $\mathbf{k}_i$ is scattered by the sample into an outgoing neutron with a wave vector $\mathbf{k}_f$. The scattering process is illustrated by the scattering triangle. $\mathbf{Q}$ is the wave vector transfer.

The partial differential cross-section is denoted by

$$\frac{d^2\sigma}{d\Omega dE_f}.$$

It gives the fraction of neutrons with incident energy E_i scattered into an element of solid angle $d\Omega$ with an energy between E_f and E_f+dE_f. Its dimension is area per unit energy.

The partial differential cross-section can be written as

$$\left(\frac{d^2\sigma}{d\Omega dE_f}\right)_{\lambda_i\to\lambda_f} = \frac{k_f}{k_i}\left(\frac{m_n}{2\pi\hbar^2}\right)^2 \left|\langle \mathbf{k}_f\lambda_f \left|V(\mathbf{Q})\right| \mathbf{k}_i\lambda_i\rangle\right|^2 \delta\left(\hbar\omega - (E_f - E_i)\right),$$

where $|\lambda_i\rangle$ and $|\lambda_f\rangle$ are the states of the sample before and after scattering. $V(\mathbf{Q})$ is the Fourier transform of the scattering potential.

When the incoming neutron beam is unpolarized, and a random distribution of the nuclear spins is assumed, the partial differential cross-section for a monoatomic sample can be split into a coherent and an incoherent term:

$$\left(\frac{d^2\sigma}{d\Omega dE_f}\right) = \left(\frac{d^2\sigma}{d\Omega dE_f}\right)_{coherent} + \left(\frac{d^2\sigma}{d\Omega dE_f}\right)_{incoherent}.$$

Coherent scattering is related to the correlated motion of the atoms in the sample, therefore it tells us about collective excitation modes such as magnons and phonons. Incoherent scattering, on the other hand, is related to the independent behavior of atoms in the sample. It provides information about local dynamics, such as diffusion of single atoms.

2.2 Nuclear Scattering

Compared to a typical neutron wavelength, nuclear forces are short ranged. Therefore one can look at nuclear neutron scattering as s-wave scattering from a pointlike scatterer. The interaction is then described by the Fermi pseudopotential

$$V(\mathbf{Q}) = \frac{2\pi\hbar^2}{m_n} b\delta(\mathbf{r} - \mathbf{R}),$$

where $\mathbf{r}$ is the position of the neutron, $\mathbf{R}$ the position of the nucleus and b is the scattering length. The magnitude of b describes the strength of the scattering, and its sign indicates whether the incident and outgoing waves are in or out of phase. The scattering length also depends on the composition of the nucleus and the relative orientation of the neutron spin to the spin of the nucleus. Therefore, scattering lengths are isotope specific. The average scattering length is $\overline{b} = \sum_i f_i b_i$ and its variance is $\overline{b^2} = \sum_i f_i b_i^2$, where f_i is the fraction of the isotope with the scattering length b_i in the target.

The partial differential cross sections for coherent and incoherent scattering for a mono-atomic sample are as follows:

$$\begin{aligned} \left(\frac{d^2\sigma}{d\Omega dE_f}\right)_{coherent} &= \frac{\sigma_{coh}}{4\pi}\frac{k_f}{k_i} S_{coh}, \\ \left(\frac{d^2\sigma}{d\Omega dE_f}\right)_{incoherent} &= \frac{\sigma_{inc}}{4\pi}\frac{k_f}{k_i} S_{inc}, \end{aligned}$$

where the cross sections are $\sigma_{coh} = 4\pi\overline{b}^2$ and $\sigma_{inc} = 4\pi(\overline{b^2} - \overline{b}^2)$ and the scattering functions are

$$\begin{aligned} S_{coh} &= \frac{1}{2\pi\hbar}\sum_{jj'}\int_{-\infty}^{\infty} dt\, e^{-i\omega t}\left\langle e^{i\mathbf{Q}\mathbf{r}_j(t)} e^{-i\mathbf{Q}\mathbf{r}_{j'}(0)}\right\rangle, \\ S_{inc} &= \frac{1}{2\pi\hbar}\sum_{j}\int_{-\infty}^{\infty} dt\, e^{-i\omega t}\left\langle e^{i\mathbf{Q}\mathbf{r}_j(t)} e^{-i\mathbf{Q}\mathbf{r}_{j}(0)}\right\rangle, \end{aligned}$$

where the brackets $\langle\rangle$ denote the thermal average. The elastic coherent scattering contains Bragg peaks if the arrangement of scattering centers in the sample is periodic and if the momentum transfer $\mathbf{Q}$ is equal to a reciprocal lattice vector $\mathbf{G} = \mathbf{Q} = \mathbf{k}_i$ - $\mathbf{k}_f$. For a monochromatic incoming beam this corresponds to Bragg's law:

$$n\lambda = 2dsin(\theta) = \frac{4\pi}{G} sin(\theta),$$

where d is the spacing between two adjacent lattice planes. Using Bragg's condition, the coherent elastic differential cross section is given by

$$\left(\frac{d\sigma}{d\Omega}\right)_{coherent}^{elastic} = N\frac{(2\pi)^3}{V}\sum_{\mathbf{G}}\delta\left(\mathbf{Q}-\mathbf{G}\right)\left|F_N(\mathbf{G})\right|^2$$

where V is the volume of the nuclear unit cell, $F_N(\mathbf{G}) = \sum_j \bar{b}_j e^{i\mathbf{Q}\mathbf{r}_j} e^{-W_j}$ is the static nuclear structure factor which contains information on the atomic positions within a unit cell and e^{-W_j} is the Debye-Waller factor. It is the mean square displacement of the j-th atom and describes the reduction of the scattering amplitude due to thermal vibrations of the atoms about their equilibrium position.

2.3 Magnetic Scattering

Neutrons have no charge, but they do have a magnetic dipole moment $\vec{\mu}_n = -\gamma\mu_n\vec{\sigma}$, where μ_n is the nuclear magneton, $\gamma = 1.913$ is the gyromagnetic ratio of the neutron, and $\vec{\sigma}$ the Pauli spin operator. Neutron beams can be polarized.

Through its magnetic moment a neutron can interact with the magnetic moment of the sample via dipole-dipole interaction. The magnetic interaction potential can be written as

$$V_m = -\boldsymbol{\mu}_n\mathbf{B},$$

where the magnetic field $\mathbf{B}$ has two contributions

$$\mathbf{B} = \mathbf{B}_S + \mathbf{B}_L,$$

where $\mathbf{B}_S$ and $\mathbf{B}_L$ are the respective contributions from the spin and angular momentum of the electron. For half filled electron shells or quenched angular momentum (which is, for example, the case for Cu^{2+} ions studied in this thesis) the spin angular momentum is the only contribution.

One can write the cross section as

$$\left(\frac{d^2\sigma}{d\Omega dE_f}\right)_{\lambda_i\sigma_i\to\lambda_f\sigma_f} = (\gamma r_0)^2\frac{k_f}{k_i}\left|\langle\sigma_f\lambda_f|\sigma\mathbf{M}_\perp|\sigma_i\lambda_i\rangle\right|^2\delta(E_{\lambda i}-E_{\lambda f}+\hbar\omega), \qquad (2.1)$$

where $r_0 = \frac{e^2}{m_e c^2}$ is the classical electron radius and

$$\mathbf{M}_\perp(\mathbf{Q}) = \hat{\mathbf{Q}}\times\left(\mathbf{M}(\mathbf{Q})\times\hat{\mathbf{Q}}\right)$$

is the component of the Fourier transformation of the sample magnetization perpendicular to the scattering vector $\mathbf{Q}$. This means that only the component perpendicular to $\mathbf{Q}$ contributes to the scattering amplitude.

The partial differential cross section is

$$\left(\frac{d^2\sigma}{d\Omega dE_f}\right) = \frac{k_f}{k_i}\left(\frac{\gamma r_0 g f(\mathbf{Q})}{2}\right)^2 e^{-2W(\mathbf{Q})} \sum_{\alpha,\beta}\left(\delta_{\alpha,\beta} - \hat{\mathbf{Q}}_\alpha \hat{\mathbf{Q}}_\beta\right) S^{\alpha\beta}(\mathbf{Q},\omega)$$

with the dynamic structure factor

$$S^{\alpha\beta}(\mathbf{Q},\omega) = \frac{1}{2\pi\hbar}\sum_{jj'} e^{i\mathbf{Q}(\mathbf{r}_j - \mathbf{r}_{j'})} \int_{-\infty}^{\infty} dt e^{-i\omega t}\left\langle S_j^\alpha(t)\, S_{j'}^\beta(0)\right\rangle,$$

where $\alpha, \beta = x, y, z$ are Cartesian coordinates. Since in this thesis no data from polarized neutron scattering are used, the indices α and β can be omitted. The dynamic structure factor is the Fourier transformation of the time-dependent spin-spin correlation function, and is measured by neutron scattering. g is the Lande factor and $f(\mathbf{Q})$ is the form factor, which is introduced in section 2.3.1.

As for nuclear scattering, a periodic arrangement of magnetic moments leads to Bragg scattering for elastic magnetic scattering. In this case magnetic Bragg peaks occur for $\mathbf{Q} = \mathbf{G}_m = \mathbf{G} \pm \mathbf{k}$, where $\mathbf{G}_m$ corresponds to the magnetic unit cell, and

$$\left(\frac{d\sigma}{d\Omega}\right)_{mag}^{el} = (\gamma r_o)^2 N \frac{(2\pi)^3}{V_m}\sum_{\mathbf{G}} \delta(\mathbf{Q} - \mathbf{G}_m)\left|\hat{\mathbf{Q}} \times (\mathbf{F}_M(\mathbf{Q}) \times \hat{\mathbf{Q}})\right|^2,$$

where $\mathbf{F}_M(\mathbf{Q}) = \sum_j \frac{g_j}{2} f_j(\mathbf{Q}) \langle \mathbf{S}_j \rangle e^{i\mathbf{Q}\mathbf{r}_j} e^{-2W_j(\mathbf{Q})}$ is the magnetic structure factor and $f(\mathbf{Q})$ the magnetic form factor.

2.3.1 Form factor

The form factor is determined by the distribution of magnetization in a single atom and can be written as

$$f(\mathbf{Q}) = \int d\mathbf{r} s_d(\mathbf{r}) e^{\mathbf{Q}\mathbf{r}},$$

where $s_d(\mathbf{r})$ is the normalized density of the unpaired electrons. The form factor can be analytically approximated by the spherical Bessel function within the dipole approximation (spherical symmetry). Parameters for an analytical approximation of the form factors were calculated by P. J. Brown [83].

Because magnetic neutron scattering occurs principally in the outer electron orbitals, the magnetic form factor falls off with increasing $\mathbf{Q}$, while nuclear scattering from the short-ranged nuclear potential is constant. The atomic form factor for X-rays falls off slower than the magnetic one for neutrons since the relevant interaction is a long-range electromagnetic one. Figure 2.2 shows the magnetic form factors for Cu^{2+} for neutron and X-ray scattering.

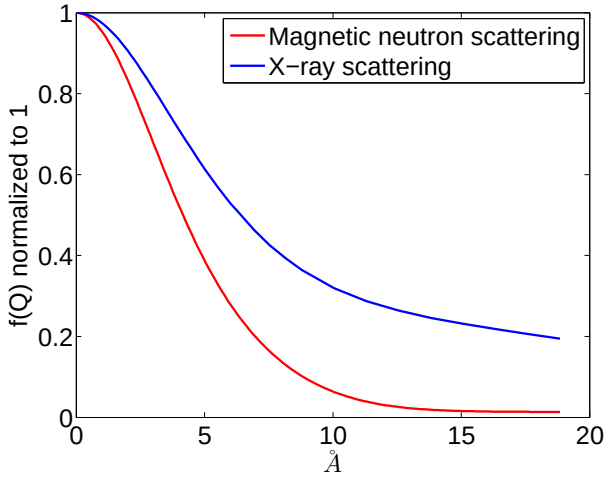

Figure 2.2: **Magnetic form factors** for Cu^{2+} for neutron and X-ray scattering [83].

2.3.2 Principle of detailed balance

During a scattering experiment, the energy loss or gain of a neutron can be measured. In thermal equilibrium, lower energy states in the sample are occupied with a higher probability than higher energy states, therefore it is more probable that the neutron will lose rather than gain energy in the scattering process. At very low temperatures one can neglect neutron energy gain, since higher energy levels (above ground state) are hardly populated.

The principle of detailed balance can be expressed in terms of the scattering function $S(\mathbf{Q},\omega)$ as:

$$S(-\mathbf{Q},-\omega) = e^{-\frac{\hbar\omega}{k_B T}} S(\mathbf{Q},\omega). \tag{2.2}$$

This principle is also valid for nuclear scattering. A short derivation of this equation is given in Squires [81].

2.3.3 Fluctuation-dissipation theorem

The fluctuation-dissipation theorem connects the dynamic structure factor, which is measured in neutron scattering experiments, with the imaginary part of the generalized magnetic susceptibility $\chi(\mathbf{Q},\omega)$ by

$$S(\mathbf{Q},\omega) = \left(1 - e^{-\frac{\hbar\omega}{k_B T}}\right)^{-1} \chi''(\mathbf{Q},\omega), \tag{2.3}$$

[84, 85].

2.3.4 Static structure factor

One can obtain the static structure factor $S(\mathbf{Q})$ and the static susceptibility $\chi'(\mathbf{Q})$ by an integral transformation of the dynamic structure factor

$$S(\mathbf{Q}) = \frac{1}{\pi}\int_0^\infty d\omega \left(1 + e^{-\frac{\hbar\omega}{k_B T}}\right) S(\mathbf{Q},\omega) \tag{2.4}$$

$$\chi'(\mathbf{Q}) = \frac{2}{\pi}\int_0^\infty d\omega \frac{1}{\omega}\left(1 - e^{-\frac{\hbar\omega}{k_B T}}\right) S(\mathbf{Q},\omega) \tag{2.5}$$

[86, 87].

2.4 Polarized neutron scattering

A useful property of neutron scattering is that we can determine both a neutron's momentum and spin state. Polarized neutron scattering allows one to distinguish between nuclear and magnetic scattering [88]. In an externally applied field the spin of a neutron can be either parallel (spin up) or anti-parallel (spin down) to the field, and the polarization can be expressed as

$$P = \frac{N_+ - N_-}{N_+ + N_-} = \frac{F-1}{F+1},$$

where N_+ neutrons have spin up and N_- have spin down. The flipping ratio $F = \frac{N_+}{N_-}$ can be measured experimentally.

Instead of only one cross-section (2.1) one measures now non-spin-flip and spin-flip cross sections. The structure factor would then be denoted by $S^{\alpha\beta}(\mathbf{Q},\omega)$, where the indices α, β denote the polarization of the spin of the incident and outgoing neutron with respect to a quantization axis. Non-spin-flip scattering is only sensitive to components of magnetization parallel to the neutron spin, while spin-flip scattering is only sensitive to components of magnetization perpendicular to the neutron spin. This means that if the polarization is parallel to the scattering vector $\mathbf{Q}$, the magnetization in the direction of the polarization will not be observed because the magnetic interaction vector will be zero, and all magnetic scattering will be spin flip [88–90].

2.5 Neutron scattering instruments

2.5.1 Triple-Axis Spectrometer

Several experiments for this thesis were performed on triple-axis spectrometers (TAS). Figure 2.3 shows a schematic outline of a triple-axis spectrometer. The

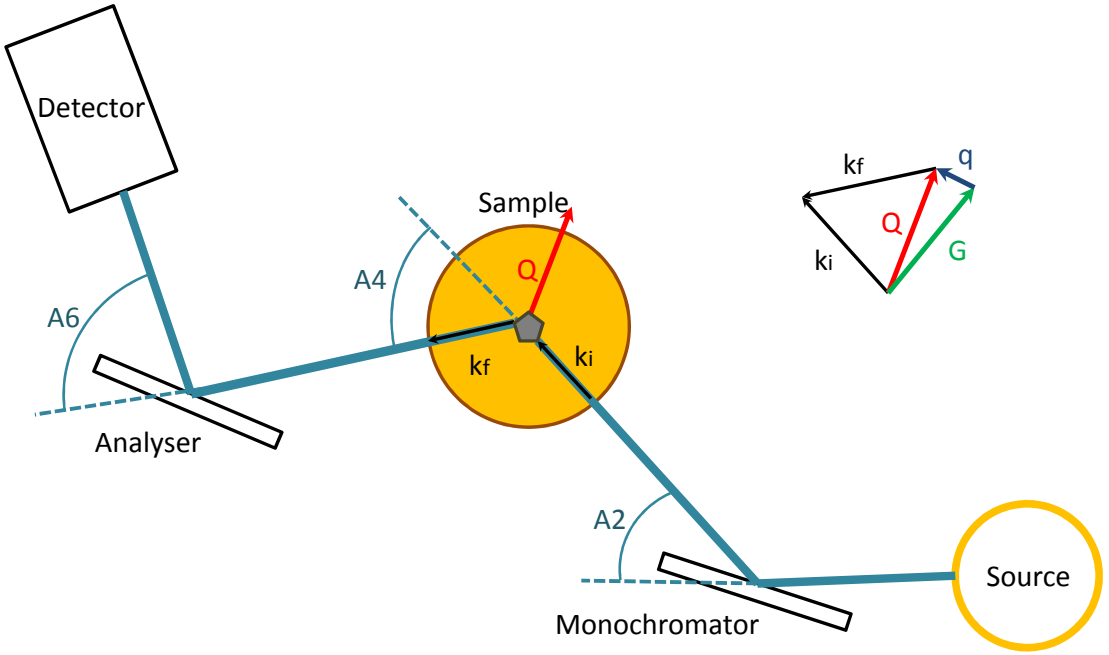

Figure 2.3: **Schematic outline of a triple-axis spectrometer.** The three axes the instrument can rotate about are at the positions of the monochromator, the sample and the analyser.

name of this instrument derives from the fact that it has three axes. The first axis is at the location of the monochromator which selects neutrons with a certain wave length. The neutrons are then scattered by the sample, which is at the location of the second axis, and a certain direction of the outgoing beam is chosen. The analyser, at the third axis, selects neutrons with a certain wavelength which are then counted in the detector.

Any scattering process has to satisfy energy and momentum conservation,

$$\mathbf{Q} = \mathbf{k}_i - \mathbf{k}_f = \mathbf{G} + \mathbf{q}, \tag{2.6}$$

$$\hbar\omega = \frac{\hbar^2}{2m_n}\left(k_i^2 - k_f^2\right), \tag{2.7}$$

where $\mathbf{G}$ is a reciprocal lattice vector of the sample and $\hbar\omega(\mathbf{q})$ the energy of an excitation of wave-vector $\mathbf{q}$.

Since in real experiments the beams are not perfectly monochromatic and collimated, one measures a volume of phase space around the selected values $\mathbf{Q}_0$ and

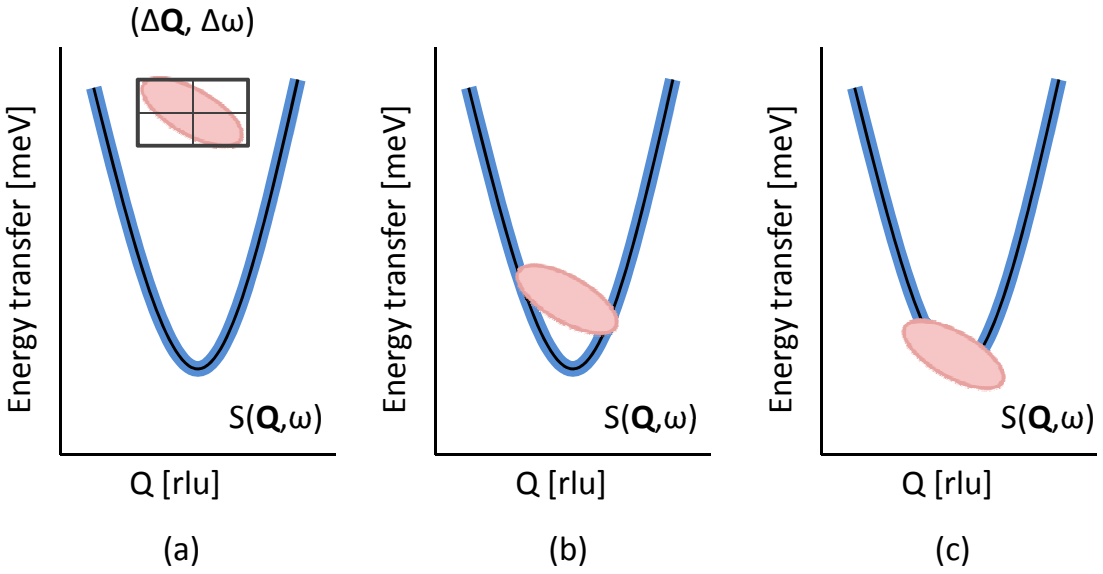

Figure 2.4: **Illustration of the convolution of the resolution ellipsoid and the scattering function.** In (a) a dispersion is shown. The blue shaded area illustrates the spectral width of the mode. The resolution ellipsoid is shown with no overlap between the dispersion and the ellipsoid. The resolution ellipsoid and dispersion have a partial overlap in (b) and a big overlap in (c) [23].

ω_0. The measured signal is then described by a convolution of the resolution function $R\left(\Delta\mathbf{Q} = \mathbf{Q} - \mathbf{Q}_0, \Delta\omega = \omega - \omega_0\right)$ and the scattering function $S\left(\mathbf{Q}, \omega\right)$ [85] as illustrated in Figure 2.4.

Both analytical methods and numerical calculations are used to compute the resolution function for a given instrumental configuration. [91–93]. The volume and form of the resolution ellipsoid can be calculated by two methods. The first method, called the Cooper-Nathans method, considers the geometry of the triple axis spectrometer but neglects spatial effects such as the size of the sample [94]. The second method by M. Popovici [95] considers such elements additionally to the considerations already made for the Cooper-Nathans method. In this thesis fits of resolution convoluted functions are used in chapter 4 and the resolution ellipsoid was calculated using the Popovici method.

The advantages of triple-axis spectrometers are that constant-$\mathbf{Q}$ or constant-E scans can be made and that polarization analysis can be used. The disadvantages are that both monochromator and analyzer can give rise to higher order effects. This can be minimized e.g. by using an appropriate filter or wisely choosing the incident and outgoing energy. A good overview over spurious peaks is given in chapter 6 of reference [85]. By restricting the measurements along certain directions it is possible that something important might be missed. Usually, before doing a triple-axis experiment, information about the sample is collected using different techniques [96].

Instruments used for this thesis are:

- The thermal triple-axis spectrometer IN22 at ILL
- The thermal triple-axis spectrometer EIGER at SINQ, PSI.

2.5.2 Time of Flight Spectrometer

Unlike triple-axis spectrometers, neutron time-of-flight spectrometers (ToF) exploit the particle property of the neutron. At pulsed sources the high peak flux and time structure are used optimally by the ToF technique. Choppers can be used to obtain a pulsed structure at steady state (reactor) sources. Before the beam is scattered by the sample, a wavelength is selected using a chopper (as for LET and IN5) or crystal monochromator. After interacting with the sample, the neutrons are detected by a large array of detectors placed equidistant from the sample. Some neutrons exchange kinetic energy with excitations in the sample and change their velocity. This reduces (for energy gain) or increases (for energy loss) the flight time of the neutron compared to elastic scattering. Energy and momentum transfer can then be written as

$$\begin{aligned} \hbar\omega(t) &= \frac{m_n}{2} L^2 \frac{t_f^2 - t_i^2}{t_i^2 t_f^2}, \\ Q &= \frac{m_n}{\hbar} L \sqrt{\frac{t_f^2 + t_i^2 - 2t_i t_f cos\,(2\theta)}{t_i^2 t_f^2}}, \end{aligned}$$

where L is the distance between the sample and the detector, t_i is the flight time for the distance L corresponding to an initial energy E_i, and t_f is the flight time of the scattered neutrons [97]. Time-of-flight spectrometers may be divided into two classes: Direct geometry spectrometers, in which the incident energy E_i is fixed, and indirect geometry spectrometers, where a fixed energy is selected after scattering with the sample.

Generally, ToF are better suited for measurements over a broad range in $(\mathbf{Q}, \omega)$ space, while triple-axis spectroscopy is advantageous for detailed investigations at well defined $(\mathbf{Q}, \omega)$ points. This distinction is becoming less valid with recent developments in ToF and TAS instrumentation. Multi-chopper spectrometers offer good control over the resolution by selecting the incident energy via the phase of the choppers, and control the resolution of the incident energy via the transmission width of the choppers [98].

For this thesis experiments were performed on the direct geometry time-of-flight spectrometers IN5 at ILL and LET at ISIS.

Chapter 3

Multispinons at finite temperatures in the spin-$\frac{1}{2}$ Heisenberg antiferromagnetic chain $CuSO_4*5D_2O$

Since 1931, when Hans Bethe presented the so called *Bethe ansatz* to calculate the eigenfunction of the one dimensional Heisenberg system [99], the interest in the Heisenberg model has not faded. The spin-$\frac{1}{2}$ Heisenberg model has been studied widely, both theoretically [71, 74, 76, 86, 100–106] and experimentally [14, 16–18, 107–109].

What makes the spin-$\frac{1}{2}$ Heisenberg antiferromagnetic chain interesting is its excitation spectrum. It consists of fractional excitations called *spinons* [4, 71]. The excitation spectrum has been calculated for temperature T = 0 and as a function of the temperature [76, 86, 103–106].

We used inelastic neutron scattering to study the evolution of the excitation spectrum as a function of the temperature. $CuSO_4*5D_2O$ is an excellent model material for the spin-$\frac{1}{2}$ Heisenberg antiferromagnetic chain. Because its main exchange is only 3 K [11, 72, 77], it is possible to study excitations up to ten times the exchange without needing to worry about thermal expansion effects.

3.1 Introduction

3.1.1 Theoretical background

In 1931 Bethe presented the *Bethe ansatz* to calculate the eigenfunction of the one dimensional Heisenberg system [99]. The excitation spectrum of the spin-$\frac{1}{2}$ Heisenberg antiferromagnet was first determined by des Cloizeaux and Pearson in 1962 [74]. In this section theoretical calculations for the excitation spectrum, which consists of quasi-particles called spinons, are presented.

Calculations for the excitations spectrum

For T = 0 Müller [103] calculated the dynamical structure factor for the one dimensional isotropic Heisenberg antiferromagnet as a function of momentum q and energy ω. q is given in units of 2π. The dynamical structure factor approximates the two-spinon continuum by introducing a cutoff at the upper two-spinon boundary

$$S(q,\omega) = \frac{A_M}{\sqrt{\omega^2 - \epsilon_l^2(q)}} \Theta\left(\omega - \epsilon_l(q)\right) \Theta\left(\epsilon(q)_u - \omega\right),$$

where A_M is a constant, Θ is the Heaviside step function and ϵ_l and ϵ_u are the lower and upper boundaries of the continuum and given by

$$\begin{aligned} \epsilon_l &= \frac{\pi}{2} \left| J \sin q \right|, \text{ and} \\ \epsilon_u &= \pi \left| J \sin \frac{q}{2} \right|. \end{aligned}$$

Schulz [104] used field theoretical techniques to calculate the structure factor at the antiferromagnetic zone center $q = 0.5$ for finite temperatures,

$$S(0.5,\omega) = \frac{e^{\hbar\omega/k_B T}}{e^{\hbar\omega/k_B T} - 1} \frac{A_{\text{Schulz}}}{T} \Im \left(\frac{\Gamma^2\left(\frac{1}{4} - i\frac{\omega}{4\pi T}\right)}{\Gamma^2\left(\frac{3}{4} - i\frac{\omega}{4\pi T}\right)} \right), \tag{3.1}$$

where A_{Schulz} is a constant.

In equation (3.1) the structure factor $S(q,\omega)\cdot T$ depends only on the dimensionless ratio ω/T.

Using conformal field theory, Starykh [105, 110, 111] adds logarithmic corrections due to umklapp scattering processes

$$\begin{aligned} S(0.5,\omega) = \frac{e^{\frac{\hbar\omega}{k_B T}}}{e^{\frac{\hbar\omega}{k_B T}} - 1} \frac{A_{\text{Starykh}}}{\pi T} 2^{2\Delta - 3/2} \sin(2\pi\Delta) \left(\ln \frac{T_0}{T}\right)^{1/2} \cdot \\ \Gamma^2(1-2\Delta)\, \Im \left(\frac{\Gamma^2\left(\Delta - i\frac{\omega}{4\pi T}\right)}{\Gamma^2\left(1 - \Delta - i\frac{\omega}{4\pi T}\right)} \right), \end{aligned} \tag{3.2}$$

where $\Delta = \frac{1}{4}\left(1 - \frac{1}{2\ln\frac{T_0}{T}}\right)$ is a temperature dependent scaling dimension and T_0 is the high-energy cutoff. A_{Starykh} is again a constant. Equations (3.1) and (3.2) are given for small temperatures. This usually means $T < J$.

Another scaling relation for finite temperatures is given by Barthel [112] and has the form

$$S(0.5,\omega) = \frac{e^{\frac{\hbar\omega}{k_B T}}}{e^{\frac{\hbar\omega}{k_B T}} - 1} \frac{a\widetilde{\omega}}{1 + b\widetilde{\omega}^3}, \tag{3.3}$$

where a and b are two parameters which are determined by data fitting and $\widetilde{\omega} = \frac{\omega}{T}$. Barthel [106] used a method called time-dependent density matrix renormalization group simulations (t-DMRG) to calculate the structure factor for one dimensional quantum systems. In this thesis we will not use results by Barthel other than equation (3.3).

Two- and four-spinon states

Calculations of the dynamic structure factor over the whole spectrum show that two-spinon states explain only 72.89 % of the total integrated intensity [113]. Caux and Hagemans calculated the exact structure factor for two- and four-spinon states. They have shown that four-spinon states carry the majority of the missing first momentum sum rule, namely 27(1) % [76].

Calculations of the excitation spectrum: Conformal field theory results by Werner and Klümper

Werner and Klümper [114] calculate the line shapes of dynamical correlation functions for a one-dimensional antiferromagnetic Heisenberg model. The correlation function for finite systems can be calculated by diagonalizing the spin Hamiltonian. The Bethe ansatz and conformal field theory are used.

The numerical results for finite systems were fitted with a theoretical prediction for the imaginary part of the susceptibility given by

$$\chi''(0.5,\omega) = \chi''_{CFT}(0.5,\omega)\frac{\left(\Lambda^2-\omega^2\right)^{\alpha}}{2\Lambda^{2\alpha}}\Theta(\Lambda-|\omega|), \tag{3.4}$$

where energies are given in units of the exchange J. The upper continuum edge Λ and the exponent α are given in in Table 3.1.

The susceptibility obtained from conformal field theory, χ_{CFT}, is given for T = 0 by

$$\chi''_{CFT}(q,\omega) \approx \begin{cases} 0 & \text{for } \omega < v|q-0.5|, \\ \left[\omega^2 - v^2(q-0.5)\right]^{x-1} & \text{otherwise,} \end{cases} \tag{3.5}$$

where v is the velocity of the low-lying spin excitations and given in units of J, and x is a scaling dimension. For small temperatures the susceptibility obtained from conformal field theory is given by

$$\chi''_{CFT}(q,\omega) = \Im\left(\sin(\pi x)v^{1-2x}\chi_0(\pi T)^{2x-2}F_x\left(\frac{\omega - v(q-0.5)}{2\pi T}\right)F_x\left(\frac{\omega + v(q-0.5)}{2\pi T}\right)\right) \tag{3.6}$$

with

$$F_x(k) = 2^{x-1}\Gamma(1-x)\frac{\Gamma\left(\frac{x}{2} - i\frac{k}{2}\right)}{\Gamma\left(1-\frac{x}{2} - i\frac{k}{2}\right)}.$$

The temperature T is given in units of J. The value of the scaling dimension x depends on the strength of the anisotropy and is given as $x = \frac{1}{2}$ for the isotropic Heisenberg chain at low temperatures. It increases to $x \sim 1$ around $T^* \approx 0.7\ J$ [114]. This temperature marks a crossover from a strongly-interacting low-temperature regime to a diffuse regime, which connects continuously to a high-temperature interacting fermion regime. The crossover at $T > T^*$ is introduced by Werner and Klümper [114] because the condition $T \ll \omega$ is then no longer fulfilled. χ_0 is a constant, and independent of T. It is weakly dependent on frustration.

For intermediate temperatures the upper limit of the continuum is approximately described by

$$\chi''(q,\omega) \approx L_-(\phi) - L_+(\phi) \tag{3.7}$$

with

$$L_\pm = \frac{K\cos(\phi) - (\Lambda \pm \omega)\,|\sin(\phi)|}{K^2 + (\Lambda \pm \omega)^2}.$$

The parameters α and Λ are the same as those introduced in equation 3.4. K is given in units of J and originally called Γ by Werner and Klümper [114] but renamed here to avoid confusion. The parameters for $q = 0.5$ are summarized in Table 3.1.

Temperature	K from [114]	ϕ from [114]	Λ from [114]	α from [114]	x from [114]
∞	0.375	-0.87	2.15	-	~ 1
$2\ J$	0.5^+	-0.825*	2.25^+	-	~ 1
J	0.941	-0.804	2.31	-	~ 1
$\frac{J}{2}$	-	-	3.3^+	1.6^+	0.5
$0.3\ J$	-	-	3.25^+	0.75^+	0.5
$0\ J$	-	-	3.25^+	0.5^+	0.4

Table 3.1: Parameters for equations (3.4) and (3.7) for $q = 0.5$ from [114]. * Interpolated. $^+$ From Figures in [114].

Calculations of the excitation spectrum: Quantum Monte Carlo and maximum entropy data by Rahnavard, Grossjohann and Brenig

Rahnavard, Grossjohann and Brenig [86, 115] used quantum Monte Carlo and maximum entropy methods to calculate the dynamic structure factor of the antiferromagnetic spin-$\frac{1}{2}$ Heisenberg chain at finite temperatures.

In order to assess the quality of their calculations, Grossjohann and Brenig [86] compared their QMC results with the scaling relations

$$S(0.5) = D_s \left(\ln \frac{T_s}{T} \right)^{\frac{3}{2}}, \tag{3.8}$$

$$\chi'(0.5) = \frac{D_\chi}{T} \left(\ln \frac{T_\chi}{T} \right)^{\frac{1}{2}}, \tag{3.9}$$

with $D_S = 0.094(1)$, $T_S = 18.3(5)$, $D_\chi = 0.32(1)$ and $T_\chi = 5.9(2)$ for $T = \frac{1}{4}$. These parameters were obtained by Starykh [105]. T, T_S and T_χ are given in units of J.

Spin diffusion

The question whether the long-wavelength dynamics in Heisenberg chains can be described by spin diffusion has long been discussed. Experimental studies of model materials for a spin-$\frac{1}{2}$ Heisenberg antiferromagnetic chain were performed using NMR [116], EPR [117], muon spin relaxation [118–120] and by measuring the thermal conductivity [121]. The results were the observations of spin transport as diffusive [117, 121], diffusive even at low temperatures [116, 118], or purely ballistic [119, 120]. Sirker et al. predict spin diffusion to be present in integrable 1-dimensional systems [122, 123]. Monte Carlo calculations of the dynamic structure factor by Grossjohann and Brenig [124] for $T \leq 0.25$ agree well with the predictions by Sirker [122].

According to Marshall and Lowde [125] the dynamic susceptibility arising from spin diffusion can be described by

$$\chi''(q,\omega) \approx A_{\mathrm{SD}} \frac{\chi'(q)}{g^2 \mu_B^2} \frac{G\omega}{\omega^2 + G^2}, \tag{3.10}$$

where $G = G(q)$. The static susceptibility $\chi'(q)$ is calculated using equation (2.5).

3.1.2 Heisenberg materials

Compounds with sufficiently weak interchain interaction can serve as spin chain model materials. The spin numbers and spin dimensionality, i.e. whether the system is Ising, XY or Heisenberg like, depends on the ion carrying the unpaired spin. In this section model materials with Heisenberg-like interactions are discussed.

Ions giving rise to Heisenberg-like interactions

In order to obtain Heisenberg-like interactions, the ions carrying the unpaired spins must have a very small single-ion anisotropy. In addition a cubic symmetry would be preferable, but crystal field splitting can change this symmetry. S-state ions as Mn^{2+}, Fe^{3+}, Gd^{3+} and Eu^{2+} are the most likely sources of Heisenberg compounds, since crystal field splitting is not important for these ions [11]. Examples are $SrMn_2V_2O_8$,

a Heisenberg antiferromagnetic chain with spin $\frac{5}{2}$ [126], or $RbMnF_3$ with $S = \frac{5}{2}$ [127, 128] and Vf_2 with $S = \frac{5}{2}$ [11, 129].

Another good example of an ion giving rise to Heisenberg interaction is Cu^{2+}. A free Cu^{2+} ion carries $L = 2$ and $S = \frac{1}{2}$, but the orbital momentum is quenched. Also the g-value anisotropy is usually small and there are no zero field splittings [130]. Model materials for spin-$\frac{1}{2}$ Heisenberg antiferromagnetic chains are e.g. KCuF3 [14, 15], $CuCl_2$*$2N(C_5D_5)$ [16, 17], $SrCuO_2$ [18, 19] and $CuSO_4$*$5D_2O$ which is studied in this thesis.

Also other ions like Ni^{2+} and Cr^{3+} can give rise to Heisenberg systems, e.g. $KNiF_3$ [131, 132] and $CsNiCl_3$ [133, 134] which have both $S = 1$.

Earlier experiments on Heisenberg chains

Already in the seventies a continuum-like spectrum with a linearly dispersing low-energy onset characteristic for spinon excitations was observed with inelastic neutron scattering in the spin-$\frac{1}{2}$ antiferromagnetic Heisenberg chain $CuCl_2$*$2N(C_5D_5)$ [16, 17].

One of the best studied model materials is $KCuF_3$. It shows good agreement with the Müller ansatz, [14, 15], and with the structure factors calculated by Schulz [58, 135], Caux [76] and Barthel [75, 106, 112].

Another model system for a spin-$\frac{1}{2}$ Heisenberg antiferromagnetic chain is $SrCuO_2$ which shows good agreement with the Müller ansatz [18, 19]. A study comparing experimental data from $SrCuO_2$ with the two- and four-spinon structure factor by Caux [76] accounts for only 80 % of the predicted intensity. The remaining discrepancy of 20 % was attributed to the Debye-Waller factor [136].

The two- and four-spinon continuum is observed not only in spin $\frac{1}{2}$-Heisenberg antiferromagnetic chains. Evidence for it was also found in the frustrated ferromagnetic spin-$\frac{1}{2}$ chain $LiCuVO_4$ by Enderle *et al.* [137].

3.1.3 $CuSO_4$*$5D_2O$

$CuSO_4$*$5D_2O$ crystallizes in the triclinic structure (space group $P\bar{1}$) shown in Figure 3.1.

The lattice parameters reported in the literature are a = 6.141 Å, b = 10.736 Å, c = 5.986 Å, $\alpha = 82.27°$, $\beta = 107.43°$ and $\gamma = 102.67°$ [140].

The copper ions carry spin-$\frac{1}{2}$ and occupy two inequivalent positions in the elementary cell at $\mathbf{r}_1 = [0,0,0]$ and $\mathbf{r}_2 = [\frac{1}{2},\frac{1}{2},0]$. They constitute two different magnetic subsystems Cu_1^{2+} and Cu_2^{2+} [141, 142]. The copper ions of one subsystem have a much stronger exchange than those of the other subsystem, and form nearly isolated chains with an exchange interaction of approximately 3 K as determined by neutron scattering [11, 72, 77]. The other subsystem remains paramagnetic down to at least 100 mK [77, 78]. Using a Bonner-Fisher relation [143] one can derive the intrachain exchange per chain from the maximum of the specific heat capacity [77, 144]. No

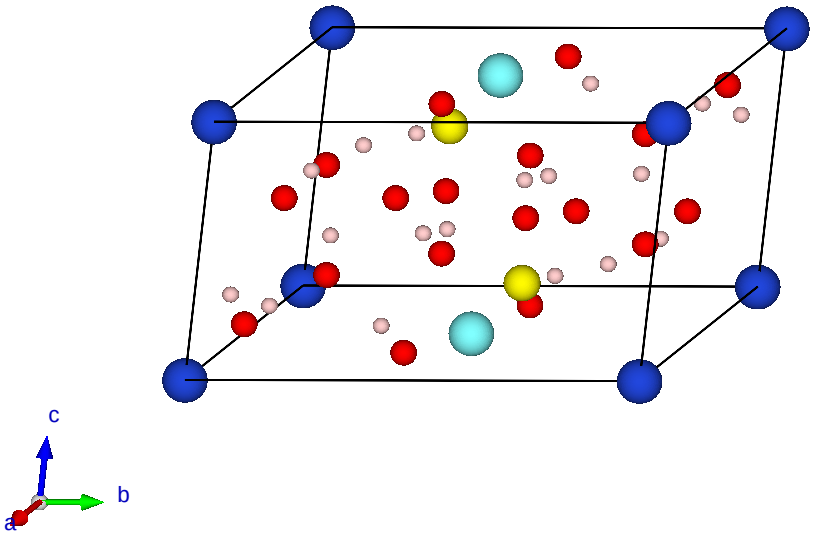

Figure 3.1: **Structure of $CuSO_4$*5D_2O [138].** The copper ions from the Cu_1^{2+} subsystem are shown dark blue, and those from the Cu_2^{2+} subsystem light blue. Sulphur is shown yellow, oxygen red and deuterium pink. The chains run along the crystallographic a-direction. This plot is made with VESTA [139].

phase transition occurs down to 100 mK. This provides an upper limit of 10^3 for the intrachain to interchain ratio [11].

$CuSO_4$*5D_2O is a good model material for the spin-$\frac{1}{2}$ Heisenberg antiferromagnetic chain [11], since it has low interchain exchange [72] and a vanishing anisotropy judging from NMR data [78]. A big advantage of $CuSO_4$*5D_2O over other model materials for the spin-$\frac{1}{2}$ Heisenberg antiferromagnetic chain is that, because of its low main exchange, it can be heated up to ten times its exchange without thermal expansion effects.

Large single crystals can be grown from solution, which is an advantage for neutron scattering. Because of the large incoherent cross section of hydrogen, $CuSO_4$*5D_2O is used instead of $CuSO_4$*5H_2O.

A previous inelastic neutron scattering study was performed by Mourigal [72]. Measurements on $CuSO_4$*5D_2O at 100 mK were compared to the Müller ansatz. The data are not well described by the Müller ansatz, the low energy part of the measured spectrum is underestimated by the Müller ansatz while the high energy part is overestimated. With accurate normalization of their data, and by comparing their data to the two- and four-spinon structure factor calculated by Caux [76], Mourigal *et al.* were able to show that two- and four-spinon states account for 99(8)% of the measured spectral weight [72].

3.2 Experiment

The experimental data analyzed in this section were obtained by M. Enderle and B. Fåk on the direct geometry Time-of-Flight (ToF) spectrometer IN5 at the Institut Laue-Langevin [145, 146]. The measurements cover the energy range between -1.3 meV and $+1.3$ meV and the temperature range between 50 mK and 32 K. In order to obtain temperatures in the mK range an orange cryostat with a dilution insert was used [147]. The sample, a $CuSO_4$*$5D_2O$ single crystal, was grown by A. Klöpperpieper at Universität des Saarlandes in Saarbrücken.

The crystal was aligned with the (100) and (011) reciprocal axes horizontal. In this orientation, the $\mathbf{q}_{1D} \approx$ (0.901, -0.345, -0.263) axis, which is parallel to the a-axis, is very close to the scattering plane. Its projection on the horizontal plane is (1, -0.302, -0.302) (given in reciprocal lattice units r.l.u.). The sample was aligned at a wavelength of $\lambda = 5$ Å with choppers at 12000 rpm. After some initial measurements, the bulk of the measurements were performed at $\lambda = 6$ Å with choppers at 16900 rpm, (ratio $\frac{4}{5}$) and $\mathbf{q}_{1D} \perp \mathbf{k}_i$ [145].

3.3 Data reduction

First the data were prepared for data analysis using Lamp [148, 149] and Horace [150]. After the data were loaded in Lamp the distance correction and normalization to monitor was done. Then the data were normalized to incoherent scattering before a flat background was subtracted. The background was determined at the lowest measured temperature, in this case 50 mK, far away from the magnetic signal. The data were then transformed from time-of-flight to energy. For this step the position of the elastic peak was fixed in time-of-flight. As a last step a mask, created from the incoherent scattering, was applied in order to cut out the direct beam and defective detector tubes. Calculations show that corrections due to the Debye-Waller factor are less than 2.5 % of the inelastic intensity. Therefore no corrections for the Debye-Waller factor were made.

Corrections for crystal tilt relative to the horizontal plane and for the form factor were performed in Horace. The projection axes were chosen to be $\mathbf{u}$ = (1, -0.302, -0.302), $\mathbf{v}$ = (0, 0, 1) and $\mathbf{w} = \mathbf{u}\times\mathbf{v}$. $\mathbf{u}$ and $\mathbf{v}$ may be perpendicular to each other, but it is not necessary. The data were then integrated perpendicular to the chain direction, along $\mathbf{v}$ and $\mathbf{w}$, and cuts were made. These cuts were then labeled with h. For example a cut labeled with h $\in$ [0.74, 0.76] is integrated between 0.74 and 0.76 in the first component h·$\mathbf{u}$. The cuts were afterwards loaded in Matlab. There, the temperatures measured close to the sample were checked using detailed balance, see section 3.3.1, and multiple and incoherent scattering were removed, see sections 3.3.2 and 3.3.3.

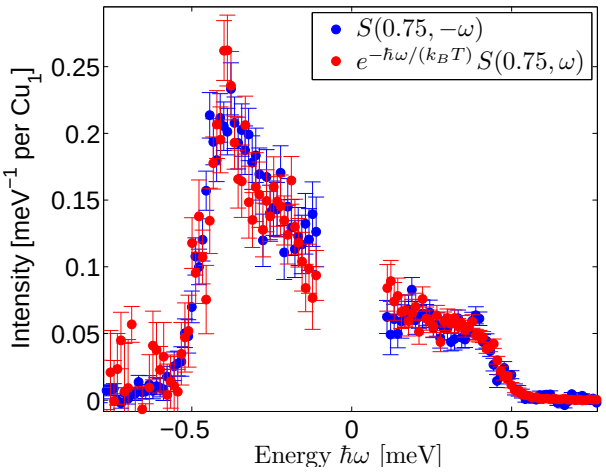

Figure 3.2: **Illustration of detailed balance.** Cut at h ∈ [0.745, 0.755] at T = 3.18(5) K. This means that the data are integrated over the interval 0.745 to 0.755 in the first component of h·**u**, and over the whole range in the second and third component which are parallel to **v** and **w**, see section 3.3. Once plotted as S(h,-ω) and once as $e^{-\hbar\omega/k_B T}$S(h,ω) with T = 3.18(5) K.

3.3.1 Detailed Balance

The actual sample temperature can be found using detailed balance by comparing the data for both sides of equation (2.2) in section 2.3.2. This was done by fitting the right hand side of equation (2.2) to the left hand side and varying the temperature T, an example for the comparison is shown in Figure 3.2. Since in the case studied here the reversal of **Q** (or h) has no effect, one can compare S(h,-ω) and $e^{-\hbar\omega/k_B T}$S(h,ω). The resulting actual sample temperatures are given in Table 3.2.

Measured T	T from detailed balance	Error Temp	T [$J \approx 3$ K [72]]
50 mK	150 mK	20 mK	$\sim 0.05\ J$
100 mK	150 mK	20 mK	$\sim 0.05\ J$
300 mK	297 mK	11 mK	$\sim J/10$
800 mK	793 mK	25 mK	$\sim J/4$
1.6 K	1.6 K	0.02 K	$\sim J/2$
3.2 K	3.18 K	0.05 K	$\sim J$
6.4 K	6.15 K	0.18 K	$\sim 2\ J$
12.8 K	12.4 K	0.47 K	$\sim 4\ J$
32 K	31.5 K	0.55 K	$\sim 10\ J$

Table 3.2: Sample temperatures measured during the experiment, and calculated using detailed balance.

3.3.2 Multiple Scattering

To remove multiple scattering, two cuts are needed. One cut with h ∈ [0, 1] (i.e. the data are integrated over the **u**-direction in addition to the **v**- and **w**-directions), called "*cut 1*", and a second cut with a small h-interval where one can clearly distinguish between multiple and magnetic scattering. In $CuSO_4$*$5D_2O$ multiple scattering is very pronounced close to 0.4 meV. A thin cut at h = 0 or 1 enables one to easily distinguish between multiple and magnetic scattering, since the magnetic signal approaches zero there. But neither data at h = 0 nor 1 are available, and the quality of the cuts decreases close to h = 0 or 1. A cut with h ∈ [0.11, 0.12], which from now on will be referred to as "*cut 2*", is close enough to h = 0 to clearly discern multiple scattering, and the data are of a sufficient quality.

Cut 1 was then scaled so that the peak close to 0.4 meV has the same height as the same peak in *cut 2*. The scaling is described by equation 3.11

$$y_{new} = S_{\mathrm{cut1}} \frac{I_{\mathrm{cut2}}}{I_{\mathrm{cut1}}}, \tag{3.11}$$

where S_{cut1} is $S(\omega)$ from *cut 1*, I_{cut1} is the height of the peak close to 0.4 meV from multiple scattering in *cut 1* and I_{cut2} is the height of the peak close to 0.4 meV from multiple scattering in *cut 2*. $\frac{I_{\mathrm{cut2}}}{I_{\mathrm{cut1}}}$ is a scaling factor which is determined only at T = 0.15(2) K. The errorbar was calculated using

$$e_{new} = \sqrt{\left(\left(\frac{S_{\mathrm{cut1}} \cdot dI_{\mathrm{cut1}}}{I_{\mathrm{cut1}}}\right)^2 + \left(\frac{dS_{\mathrm{cut1}}}{I_{\mathrm{cut1}}}\right)^2\right) \cdot I_{\mathrm{cut2}}^2 + (dI_{\mathrm{cut2}})^2 \cdot \left(\frac{S_{\mathrm{cut1}}}{I_{\mathrm{cut1}}}\right)^2}. \tag{3.12}$$

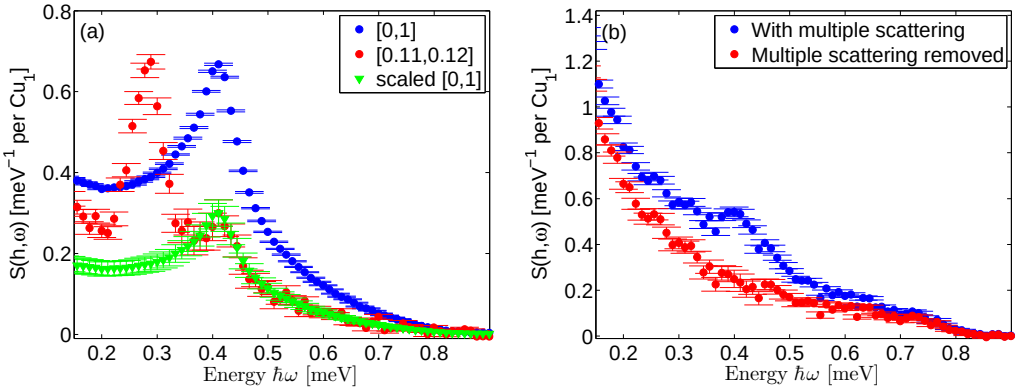

Figure 3.3: **Illustration of the process used to remove multiple scattering.** Panel (a) shows a cut from data at 0.15(2) K at h ∈ [0,1] (*cut 1*) and the same cut scaled to the height of the cut at h ∈ [0.11, 0.12] (*cut 2*). This scaled cut is then subtracted from the data with all other h-values to remove multiple scattering. (b) Cut from data at 0.15(2) K and h ∈ [0.495 0.505] before and after multiple scattering was removed.

Cut 1 and *2* and y_{new}, the scaled *cut 1* at T = 0.15(2) K, are shown in Figure 3.3 (a). y_{new} was then subtracted from all other cuts at T = 0.15(2) K in order to remove the multiple scattering. A cut before and after multiple scattering is removed is shown in Figure 3.3 (b). For higher temperatures *cut 1* was made for each temperature and then scaled with the scaling factor found at the lowest temperature, T = 0.15(2) K, to get y_{new} for each temperature. The y_{new} determined for each temperatures is then subtracted from the other cuts at higher temperatures.

3.3.3 Removing incoherent scattering

After multiple scattering, the incoherent scattering was removed as well. At the lowest temperature, in a cut where magnetic and incoherent scattering can be well separated, here h $\in$ [0.74,0.76], the incoherent scattering was fitted with an asymmetric Gaussian and an asymmetric Lorentzian. This fit is shown in Figure 3.4.

The resulting peak was then subtracted from the data at all temperatures and values of h. This method is not perfect, and some remnants of incoherent scattering often remain. For the sake of clarity these remnants are often cut out from plots.

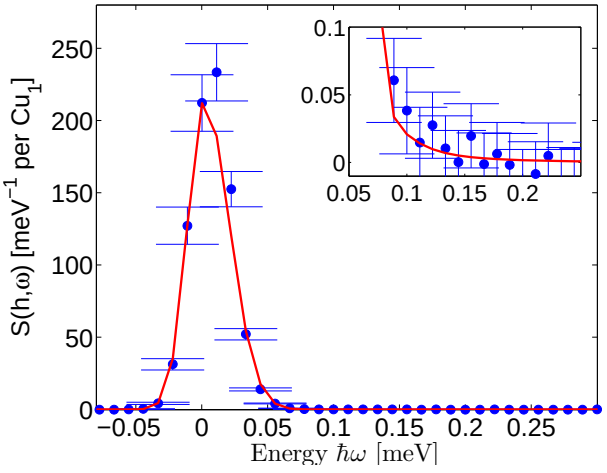

Figure 3.4: **Fit to the incoherent scattering**. Fit with an asymmetric Gaussian and Lorentzian to the incoherent peak at T = 0.15(2) K.

3.3.4 Calculating the dynamic susceptibility χ''

For further data analysis, the imaginary part of the dynamic susceptibility $\chi'' = \Im(\chi)$ is needed. It can be determined using the fluctuation-dissipation theorem introduced in section 2.3.3.

S(h,ω) and χ''(h,ω) calculated using equation 2.3 at 3.18(5) K are shown in Figure 3.5.

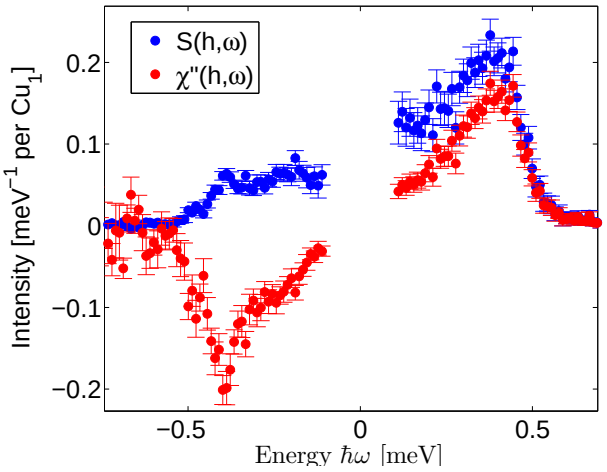

Figure 3.5: **Comparison of the dynamic susceptibility and structure factor** S(h,ω) and χ''(h,ω) at h $\in$ [0.745, 0.755] and 3.18(5) K (T $\approx$ J).

3.3.5 Increased intensity at h $\rightarrow$ 0 for increasing temperature

With increasing temperature the intensity at the antiferromagnetic zone center (h = 0.5) decreases while it increases at the antiferromagnetic zone boundaries close to h = 0 and h = 1. At 31.5(6) K the intensity close to h = 0 is strongly increased compared to h = 1, as can be seen in Figure 3.7 (b). The difference between the intensity at h = 0 and h = 1 is plotted in Figure 3.6 for three different temperatures. Since the difference in intensity at h = 0 and h = 1 does not depend on temperature, it is unlikely to originate from the sample and can be neglected for data analysis. Since the data are otherwise symmetric with respect to the antiferromagnetic zone center at h = 0.5, we evaluate the data with h $\geq$ 0.5.

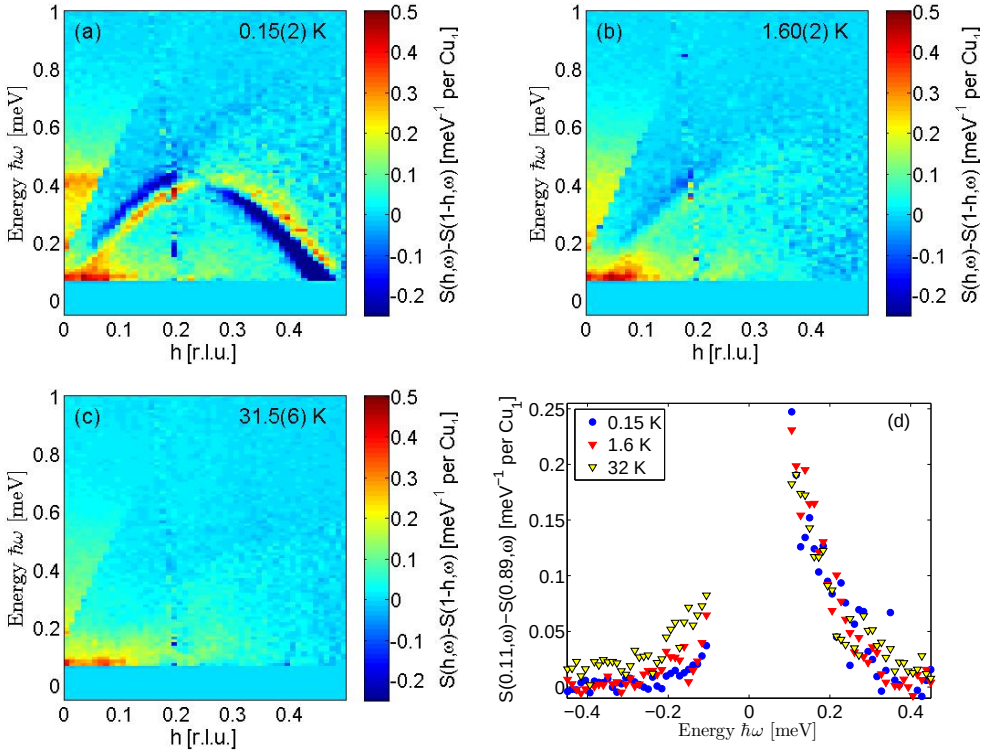

Figure 3.6: **Difference between the structure factor with h $>$ 0.5 and h $<$ 0.5** for different temperatures (a) 0.15(2) K (T $\approx$ 0.05 J), (b) 1.60(2) K (T $\approx$ $J/2$) and (c) 31.5(6) K (T $\approx$ 10 J) . (d) Cuts through this difference for the three temperatures. Errorbars were left out for better visibility.
The difference in intensity between h $\rightarrow$ 0 and h $\rightarrow$ 1 does not depend on temperature, so it is unlikely to originate in the sample. The higher intensity can be explained as a remnant of the direct beam, and can be ignored in the data analysis.

3.4 Results

Measurements were taken between T = 0.15(2) K (T ≈ 0.05 J) and T = 31.5(6) K, which is about 10 times the exchange interaction. Figures 3.7 (a) and (b) show the experimental data at the highest and lowest measured temperatures, normalized as will be described in section 3.4.1.

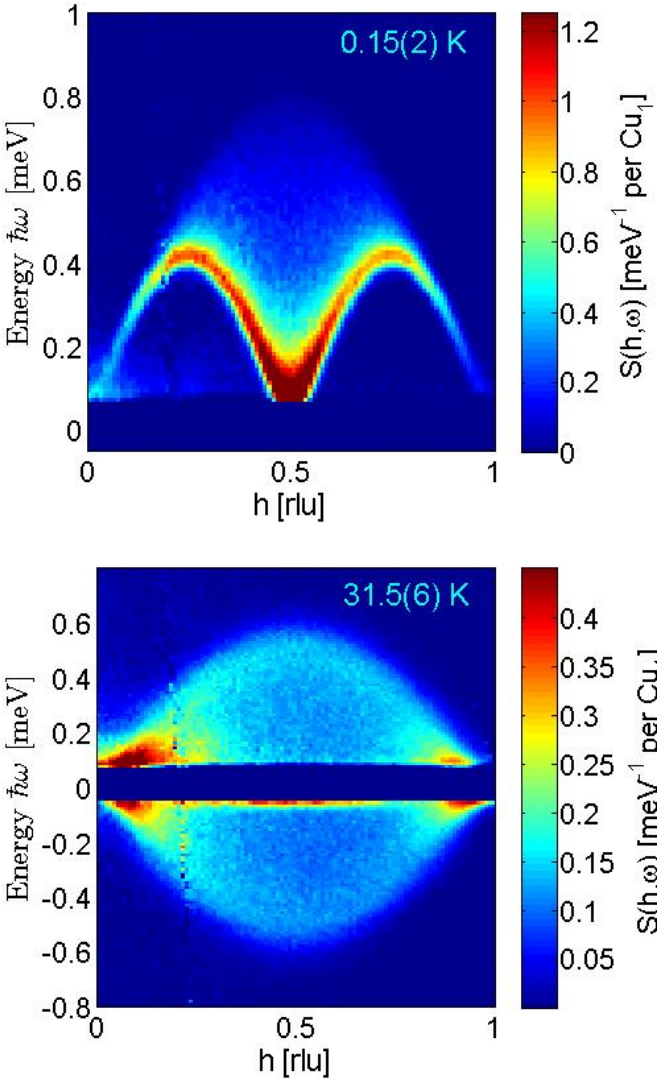

Figure 3.7: **Data at the lowest and highest measured temperatures.** Dynamic structure factor $S(h,\omega)$ $S(h,\omega)$ at T = 0.15(2) K (≈ 0.05 J) and $S(h,\omega)$ at T = 31.5(6) K (≈ 10 J).

At T = 0.15(2) K the signal is well defined, and most weight is observed around the antiferromagnetic zone center. The onset of the intensity, as well as the decrease of intensity at high energy transfers, depend on h. At 31.5(6) K, the intensity decreases at the antiferromagnetic zone center and increases below the lower boundary ϵ_l of the two-spinon continuum. The onset of intensity at high temperatures becomes

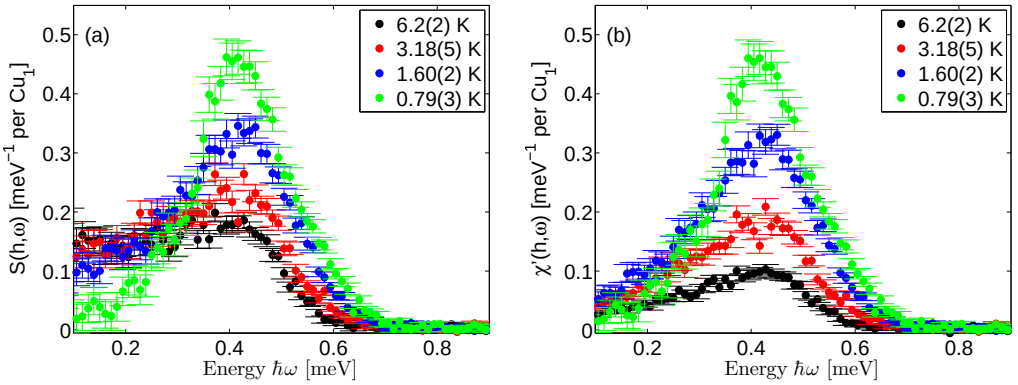

Figure 3.8: **Dynamic structure factor and susceptibility at different temperatures.** (a) $S(h,\omega)$ and (b) $\chi''(h,\omega)$ at h $\in [0.745, 0.755]$.

independent of h. The intensity increases close to to h $\rightarrow$ 1 and h $\rightarrow$ 0. The higher intensity at h $\rightarrow$ 0 can be explained as a remnant of the direct beam, see section 3.3.5.

Figure 3.8 shows the structure factor $S(h,\omega)$ and the dynamic susceptibility χ''(h,ω) for different temperatures. The changes in $S(h,\omega)$ and χ''(h,ω) from one temperature to another are smooth, especially for the dynamic susceptibility χ''(h,ω), and no sharp transition for T of the order of J is evident.

3.4.1 Low-temperature data analysis

We compared the data at T = 0.15 K ($\approx$ 0.05 J) with the exact two- plus four-spinon structure factor calculated by Caux [76], for which Mourigal has shown that it accounts for 99(8) % of the full spectral weight [72]. To do this, the method used by Mourigal to quantify the two- and four-spinon contributions in $CuSO_4$*5D_2O [72] was employed.

To compare theory and experiment, the theoretical two-and four-spinon structure factor $\widetilde{S}^{yy}_{2+4}(h,\omega)$ was convoluted with the resolution function described by a two-dimensional Gaussian, whose full widths at half maximum (FWHM) are the energy resolution σ_ω and momentum resolution σ_h. The integral of the resolution function over energy and momentum was normalized to one. The convoluted structure factor $S^{yy}_{2+4}(h,\omega)$ was normalized to $\frac{1}{3}$S(S+1). The convoluted and normalized calculated two- and four-spinon structure factor $S^{yy}_{2+4,\mathrm{norm}}(h,\omega)$ was then fitted to the data. In neutron scattering only the components of the magnetization perpendicular to the scattering vector are observable [81]. Therefore the structure factor observed in our experiments is $S(h,\omega) = S^{yy}(h,\omega) + S^{zz}(h,\omega)$.

From global and iterative fits we obtained $J = 0.2595 \pm 4.1{*}10^{-4}$ meV, the scaling factor $\mathrm{A}_{2+4} = 8.4869{*}10^{-5} \pm 6.5{*}10^{-7}$ with $2{*}\mathrm{A}_{2+4}\cdot S^{yy}_{2+4,\mathrm{norm}}(h,\omega) = S(h,\omega)_{\mathrm{Exp}}$ and $\sigma_h = 0.0773 \pm 0.0032$ (in r.l.u.). The energy resolution σ_ω(h) was determined with iterative fits, it is given in meV and depends on h. This h-dependence can be fitted

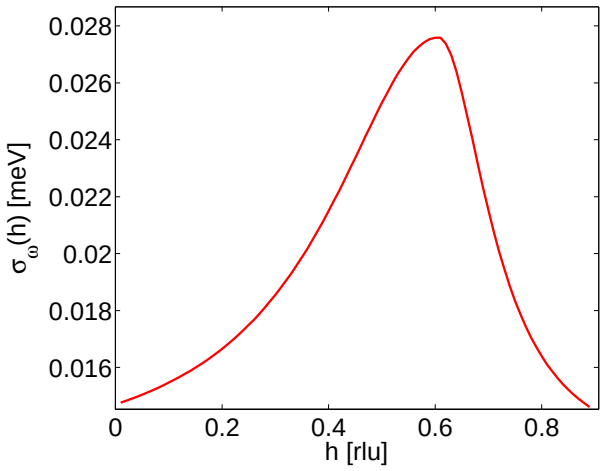

Figure 3.9: **Energy resolution as a function of h.** The energy resolution σ_ω(h) is a function of h which may be described by an asymmetric Lorentzian.

with an asymmetric Lorentzian and is shown in Figure 3.9. The values obtained from this Lorentzian are used for the convolution of the theoretical structure factor.

Figure 3.10 shows a color plot comparing the experimentally obtained $S(h,\omega) = S(h,\omega)_{\mathrm{Exp}}/A_{2+4} = S^{yy}(h,\omega) + S^{zz}(h,\omega)$ with the theoretical resolution-convoluted two- and four-spinon structure factor $2S^{yy}_{2+4,\mathrm{norm}}(h,\omega)$ by [76].

Figure 3.11 shows fits of the resolution-convoluted theoretical two- and four-spinon structure factor $2S^{yy}_{2+4}(h,\omega)$ to the measured structure factor $S(h,\omega) = S^{yy}(h,\omega) + S^{zz}(h,\omega)$. The parameters for the convolution are the ones found in this section.

The values obtained for J, A_{2+4}, σ_h and σ_ω(h) in this section are kept for comparison between theory and experiment at higher temperatures. Since the two- and four-spinon states account for 99(8) % of the spectral weight, we can normalize the experimental data at higher temperatures and obtain $S(h,\omega)_{Exp}/A_{2+4} = S(h,\omega)$. The value obtained for J (0.2595(4) meV) is between the one determined by Mourigal [72] using neutron scattering (0.252(17) meV) and the one found by Miedima [77] using specific heat measurements (0.276 meV).

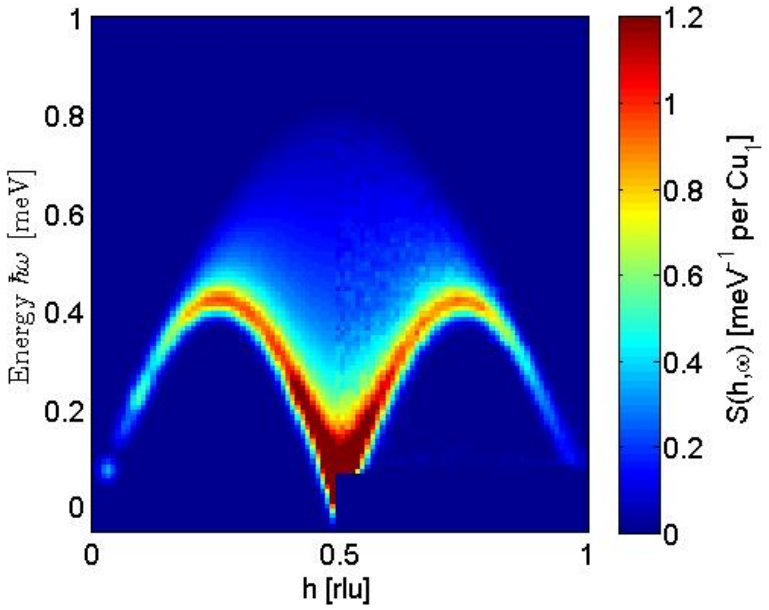

Figure 3.10: **Theoretical and experimental low temperature data.** Left side (h $<$ 0.5): Resolution-convoluted two- and four-spinon structure factor $2S^{yy}_{2+4,norm}(h,\omega)$, calculated by Caux [76] and right side (h $>$ 0.5): $S(h,\omega) = S(h,\omega)_{\mathrm{Exp}}/A_{2+4}$ measured on IN5 at 0.15(2) K = 0.05(1) J. Here J = 0.2595 $\pm$ 4.1*10^{-4} meV, σ_h = 0.0123(5), and σ_ω depends on h. The h-dependence of σ_ω(h) is shown in Figure 3.9.

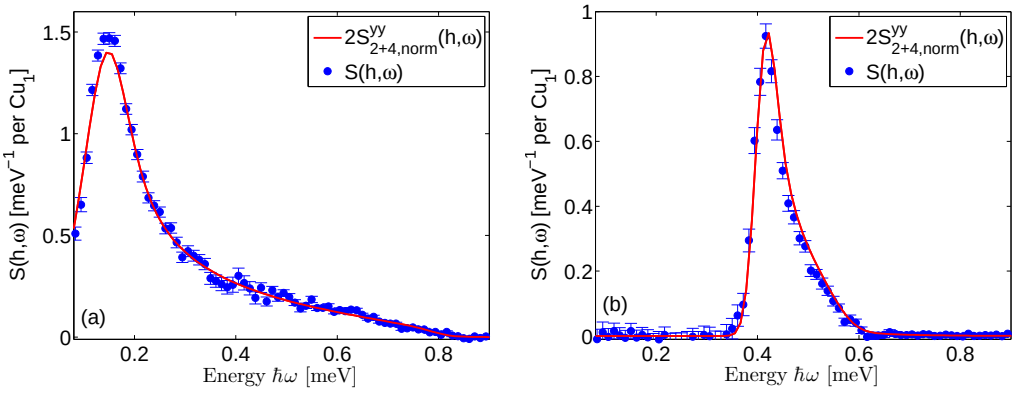

Figure 3.11: **Comparison of experimentally and theoretically obtained structure factors.** Comparison of the experimentally determined normalized $S(h,\omega) = S(h,\omega)_{\mathrm{Exp}}/A_{2+4}$ at 0.15(2) K = 0.05(1) J, blue points, to the convoluted and normalized two- plus four-spinon structure factor $2S^{yy}_{2+4,\mathrm{norm}}(h,\omega)$ from Caux [76] (red line). Here J = 0.2595(4) meV, σ_h = 0.0123(5), and σ_ω(h) depends on h, its h-dependence is shown in Figure 3.9. Cuts are at (a) h $\in$ [0.445, 0.455] with σ_ω(0.45)= 0.0234 meV and (b) h $\in$ [0.745, 0.755] with σ_ω(0.75) = 0.0183 meV.

3.4.2 Finite-temperature data analysis

Various theoretical calculations for the excitation spectrum of the spin-$\frac{1}{2}$ Heisenberg antiferromagnetic chain at finite temperatures are summarized in section 3.1.1. In this section, the experimental data are compared to theoretical calculations by Schulz [104], Starykh [105, 110, 111], Barthel [106, 112], Werner and Klümper [114] and Rahnavard and Brenig [115]. The data are also compared to a sum rule used by Starykh [105], and Grossjohann and Brenig [86], and the long-wavelength dynamics is studied.

The experimental data studied in this section are normalized by A_{2+4}, i.e. $S(h,\omega) = S(h,\omega)_{Exp}/A_{2+4}$ is used.

Scaling relations

The data are compared to the dynamic structure factors given by equation (3.1) by Schulz [104], equation (3.2) by Starykh [105, 110, 111] and equation (3.3) by Barthel [106, 112]. In order to do this, equations (3.1), (3.2) and (3.3) are convoluted with the instrument resolution and normalized as described in section 3.4.1.

Figures 3.12 and 3.13 compare the convoluted structure factor given by equation (3.1) to cuts at h $\in$ [0.495, 0.505]. The constant A_{Schulz}, which compares several prefactors into one, is determined by fits to be 0.65(2).

Equation (3.1) when multiplied by T is a scaling relation, since it then only depends on the dimensionless entity ω/T. The main Figure in 3.12 shows this scaling relation. The experimental data for temperatures between 0.15(2) K = 0.05(1) J and 6.2(2) K = 2.04(6) J and energies from 0.2 to 0.5 meV lie on a curve with the same proportionality constant A_{Schulz}. The dynamic structure factor calculated by Schulz [104] reproduces the shape of the continuum at 0.15(2) K = 0.05(1) J and also at higher temperatures correctly. The changes of the dynamic structure factor with increasing temperature are also described by this equation. But with increasing temperature the deviations between experiment and theory become bigger.

The inset of Figure 3.12 shows a cut at h $\in$ [0.495, 0.505] and 0.15(2) K = 0.05(1) J compared to equation (3.1).

The dynamic structure factor calculated by Starykh [105, 110, 111] and given by equation (3.2) is compared to experimental data in Figure 3.14. The high energy cutoff T_0 is set to πJ which is the upper spinon boundary for q = 0.5. Equation (3.2) is convoluted with the resolution function and normalized as described in section 3.4.1 and $A_{Starykh}$ is equal to one.

The theoretical structure factor calculated by Starykh [105, 110, 111] follows the shape of the continuum for temperatures up to 0.25 J, but agreement between equation (3.2) and experiment is not as good as for equation (3.1) given by Schulz. At T = 0.160(2) K = 0.532(7) J the change in curvature of the experimental structure factor is not described by the theoretical structure factor calculated by Starykh [105, 110, 111].

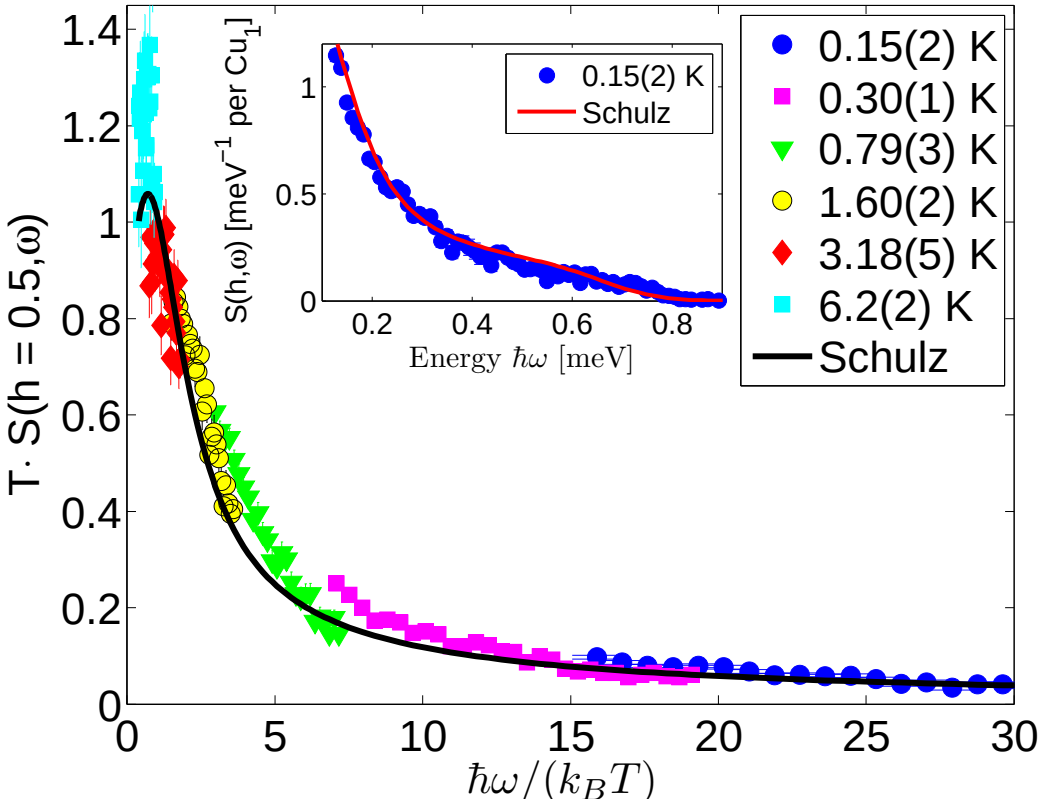

Figure 3.12: **Energy/temperature scaling for $CuSO_4$*5D_2O.**
Inset: Cut at 0.15(2) K = 0.05(1) J with h $\in$ [0.495, 0.505] compared to equation (3.1). This dynamic structure factor calculated by Schulz [104] agrees with the experimental dynamic structure factor. The best agreement is found between 0.2 and 0.5 meV.
Main Figure: Comparison of T·S(h, $\frac{\hbar\omega}{k_B \mathrm{T}}$) measured on IN5 with h $\in$ [0.495, 0.505] and energies between 0.2 and 0.5 meV to the scaling relation given by equation (3.1). The experimental data lie on a curve given by the scaling relation for temperatures between 0.15(2) K = 0.05(1) J and 6.2(2) K = 2.04(6) J with the same proportionality constant A_{Schulz}. The Gamma function used for this scaling is from reference [151]. For all other calculations the Gamma function from Mathematica has been used.

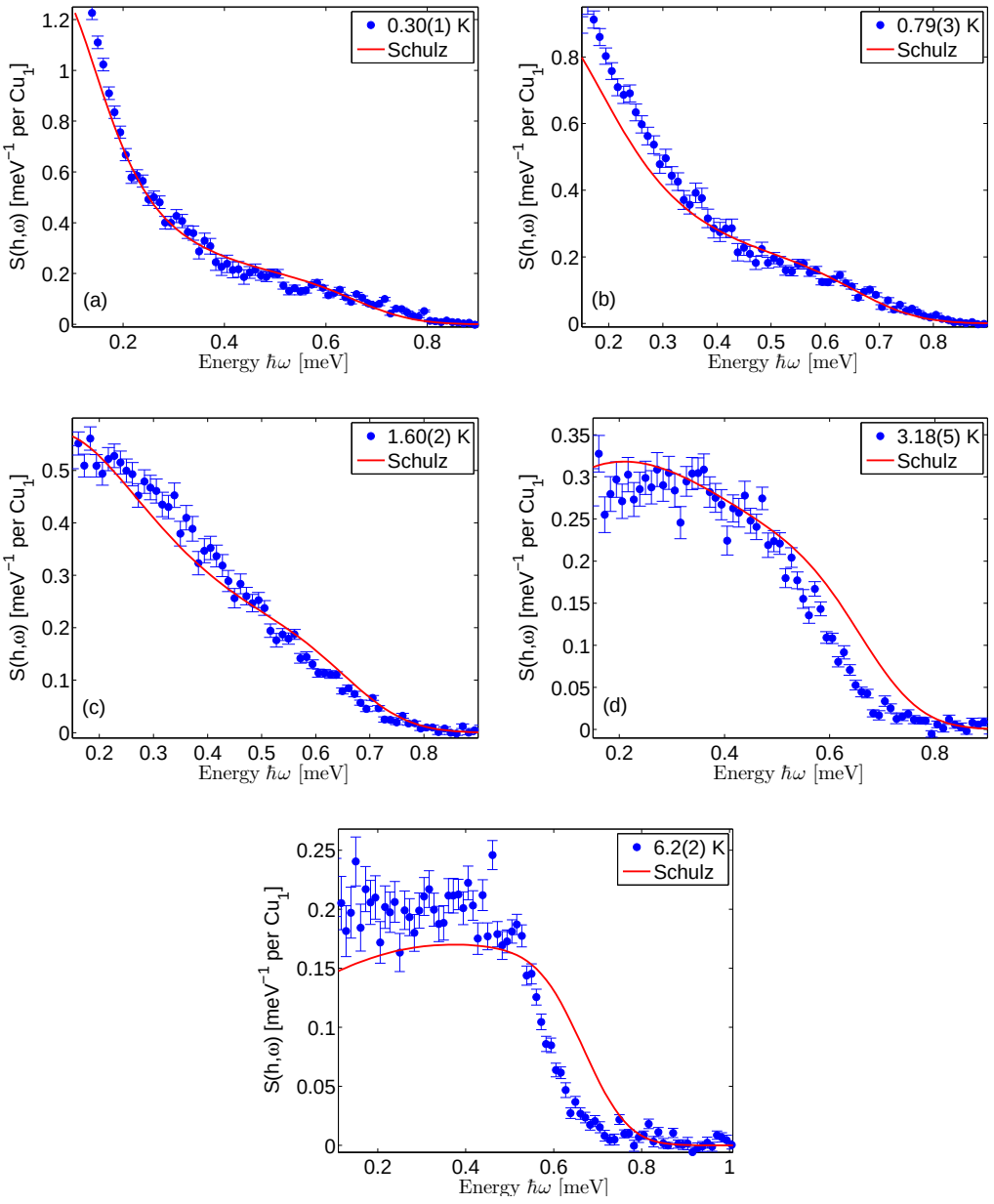

Figure 3.13: **The dynamic structure factor calculated by Schulz [104] compared to cuts** from data at h $\in$ [0.495, 0.505] at different temperatures. (a) 0.30(1) K = 0.099(4) J, (b) 0.79(3) K = 0.263(8) J, (c) 1.60(2) = 0.532(7) J, (d) 3.18(5) K = 1.06(2) J and (e) 6.2(2) K = 2.04(6) J. Deviations between the theoretical and experimental structure factor become bigger with increasing temperatures.

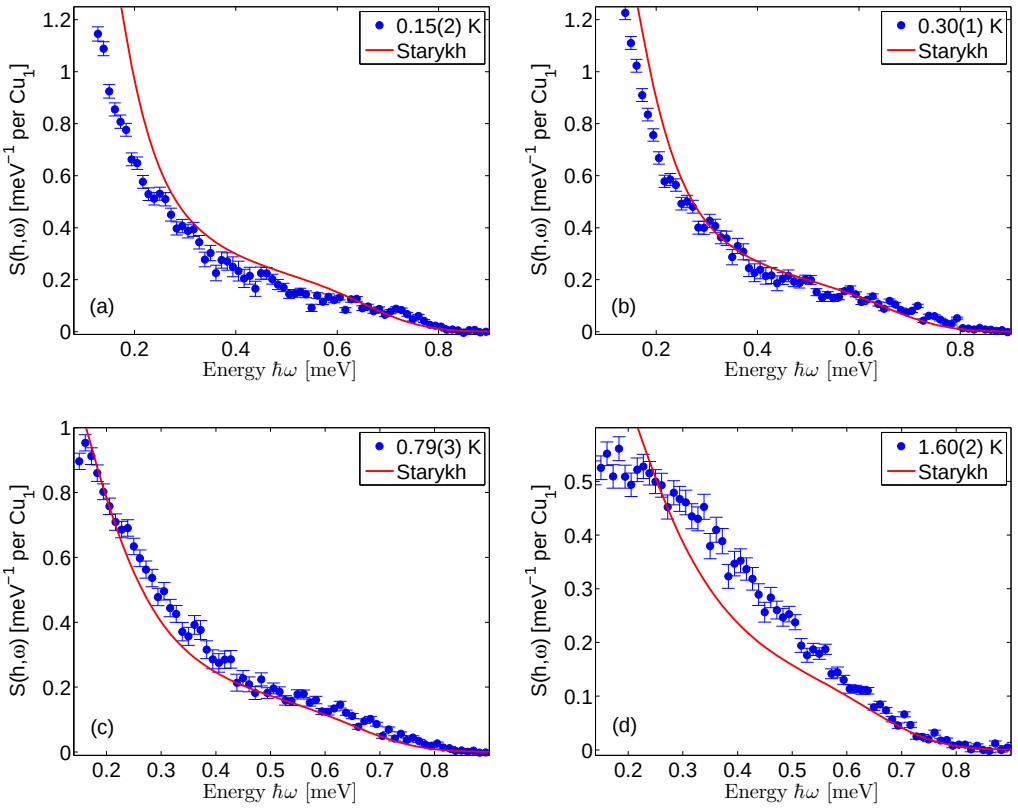

Figure 3.14: **Dynamic structure factor calculated by Starykh [105, 110, 111] compared to cuts** from data at h $\in$ [0.495, 0.505] for different temperatures: (a) 0.15(2) K = 0.05(1) J, (b) 0.30(1) K = 0.099(4) J, (c) 0.79(3) K = 0.263(8) J and (d) 0.160(2) K = 0.532(7) J.

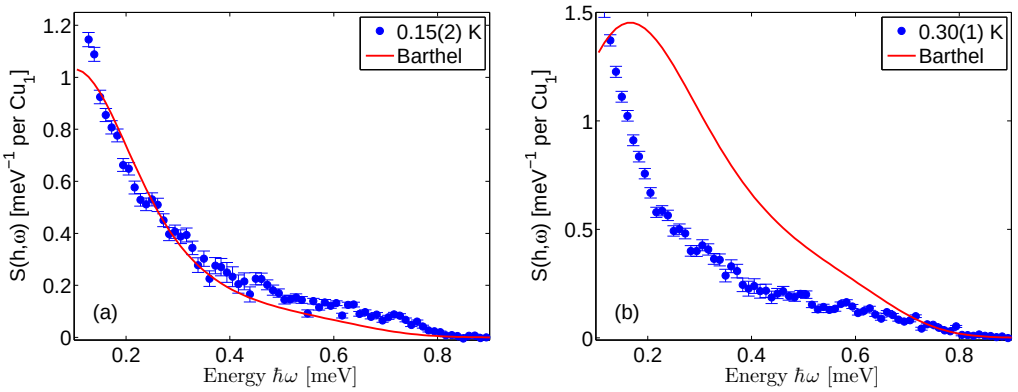

Figure 3.15: **Scaling relation calculated by Barthel [112] compared to cuts** from data at h ∈ [0.495, 0.505] for different temperatures: (a) 0.15(2) K = 0.05(1) J and (b) 0.30(1) K = 0.099(4) J.
The values obtained for the parameters at T = 0.15(2) K = 0.05(1) J are: a = -0.9(1) and b = 5(1)*10^{-4}.

Equation (3.3) given by Barthel [112] is also compared to the data. No temperature independent parameters a and b could be found by global fits at temperatures smaller than J. Therefore the parameters were fitted at the lowest measured temperature and the obtained values are a = -0.9(1) and b = 5(1)*10^{-4}. Equation (3.3) does not describe the data for temperatures above 0.15(2) K = 0.05(1) J, see Figure 3.15.

Conformal field theory results by Werner and Klümper

In this section we compare results by Werner and Klümper [114] with our data. Their numerical results from exact diagonalization of finite chains are compared with our experimental data in Figure 3.16. In order to compare numerical and experimental data, the numerically calculated data sets were convoluted with the resolution function and scaled with a scaling factor. This scaling factor was obtained by fitting the numerical data by Werner and Klümper [114] to the normalized experimental data. For the resolution convolution the parameters used were the ones obtained at low temperatures. Agreement is good for all three temperatures. Most noteworthy is the agreement between numerical data for T → ∞, and the experimental data for T = 31.5(6) K = 10.46(18) J. We expect therefore for $CuSO_4$*$5D_2O$ even for T ≫ 10 J good agreement with this numerical data.

Equations (3.4) and (3.7), which result from conformal-field theory, are also compared with cuts at h ∈ [0.495, 0.505] from our data. In order to do this, equations (3.4) and (3.7) are convoluted with the instrument resolution, as described in section 3.4.1. This leads to the resolution-convoluted theoretical dynamic susceptibility $\chi''_{WK}(h,\omega)$. Equations (3.4) and (3.5) are compared with data at T = 0.15(2) K in Figure 3.17 (a). At T = 0.79(3) K and 1.60(2) K the data are compared to equations (3.4) and (3.6). Data at T = 0.79(3) ≈ 0.25 J are compared to parameters for T =

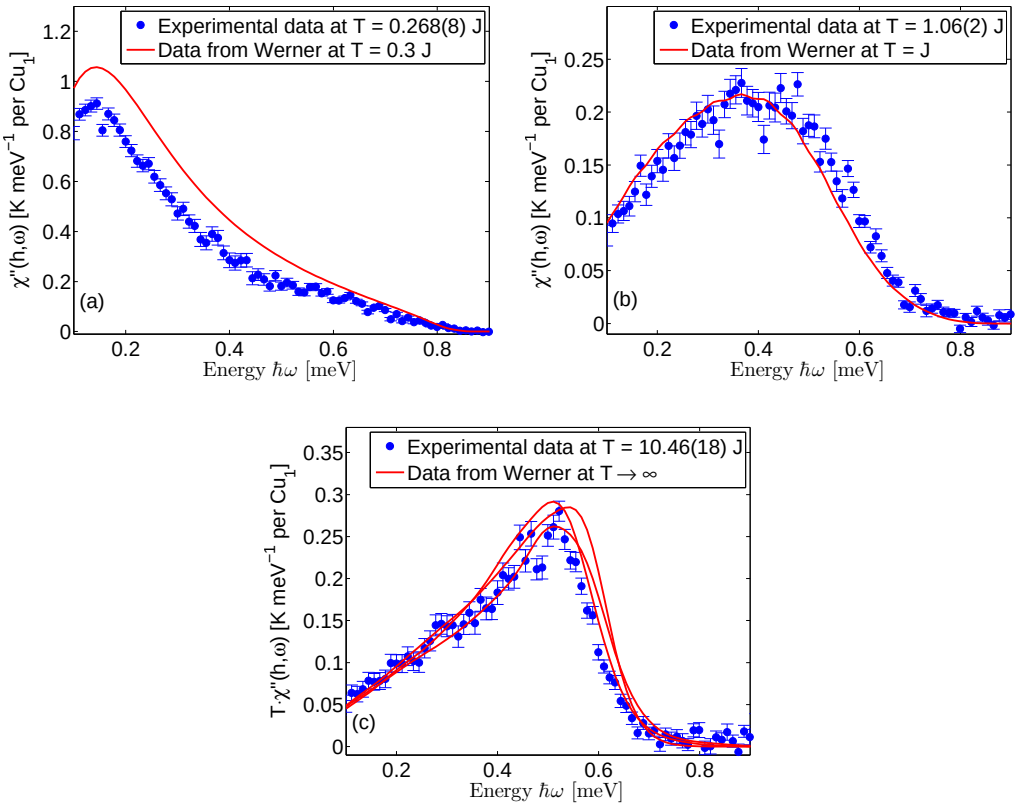

Figure 3.16: **Comparison between numerical and experimental data.** $\chi''(h,\omega)$ calculated numerically by Werner and Klümper [114] for finite chains, compared to cuts at h $\in [0.495, 0.505]$ from our data. In (a) the numerical data were calculated at T $= 0.3\ J$ while the experimental data were taken at T $= 0.79(3)$ K $= 0.263(8)\ J$. Experimental and theoretical data in (b) are at T $\approx 1\ J$ (T $= 3.18(5)$ K), and the theoretical data in (c) are calculated for T $\to \infty$ and compared with experimental data at the highest measured temperature T $= 31.5(6)$ K $= 10.46(18)\ J$.

0.3 J given in reference [114]. χ_0 is a constant and can be obtained by calculating the limit of equation (3.6) for temperatures approaching zero and then equating this result to equation (3.5). This was done with Mathematica and the resulting value is $\chi_0 = 0.16$. The comparison between data at T = 0.79(3) K and 1.60(2) K, and equations (3.4) and (3.6), are shown in Figures 3.17(b) and (c).

For temperatures above the crossover temperature T*, x is locked at 1 [114]. Substituting this into equation (3.6) leads to the sine term to be zero, but the limit for $x \to 1$ makes sense, therefore x = 0.999 is used. The data at temperatures higher than T* are then fitted using equations (3.4) and (3.6), Λ and α are allowed to vary freely. The constant χ_0 is kept fixed to 0.16.

Equations (3.4) and (3.5) show good agreement with the experimental data at T = 0.15(2) K. The dynamic susceptibility given by equations (3.4) and (3.6) reproduces the general shape of the experimental data for temperatures smaller or equal to J, but the intensity is underestimated by this calculation. T = 3.18(5) K is described correctly by equations (3.4) and (3.6) if Λ is allowed to vary freely. The experimental data at this temperature are described less good by equations (3.4) and (3.6) if Λ is fixed to the value given in Table 3.1. The resulting parameters are given in Table 3.3 and the fit is shown in Figure 3.17 (d). For $T \geq 6.2(2)$ K, using equations (3.4) and (3.6) no parameters were found which could describe our data.

Temperature [K]	Λ from fit	α from fit	x
3.18(5)	2.505(43)	0.17(4)	0.999

Table 3.3: Parameters for equations (3.4) and (3.6) from fits to the data at T = 3.18(5) K. x = 0.999 is used as an approximation for x = 1 found in reference [114].

No agreement was found between the experimental data and equation 3.7, neither with the parameters given by Werner and Klümper [114], which are summarized in Table 3.1, nor by fitting the parameters. We were unable to obtain fits for higher temperatures than $T \approx J$ using the equations from the paper by Werner and Klümper [114].

Temperature dependence and breakdown of conformal field theory

Even though the dynamic susceptibility calculated by Werner and Klümper [114] using conformal-field theory agrees with the experimental data for T = 0 and low temperatures, and their numerical results also agree with our experimental data, there are some discrepancies between their results and the experimental data.

One concerns the cut-off parameter Λ given in table 3.1. According to Werner and Klümper, this parameter varies with temperature. In Figure 3.18, the high energy behavior of the dynamic susceptibility $\chi''(h, \omega)$ is compared at different temperatures for h $\in$ [0.495, 0.505] and h $\in$ [0.745, 0.755]. Plotting the experimentally obtained $T \cdot \chi''(h, \omega)$ reveals that the intensity falls to zero at similar energies for all temperatures. Even though it seems in Figure 3.18 (a) and (c) as if the continuous

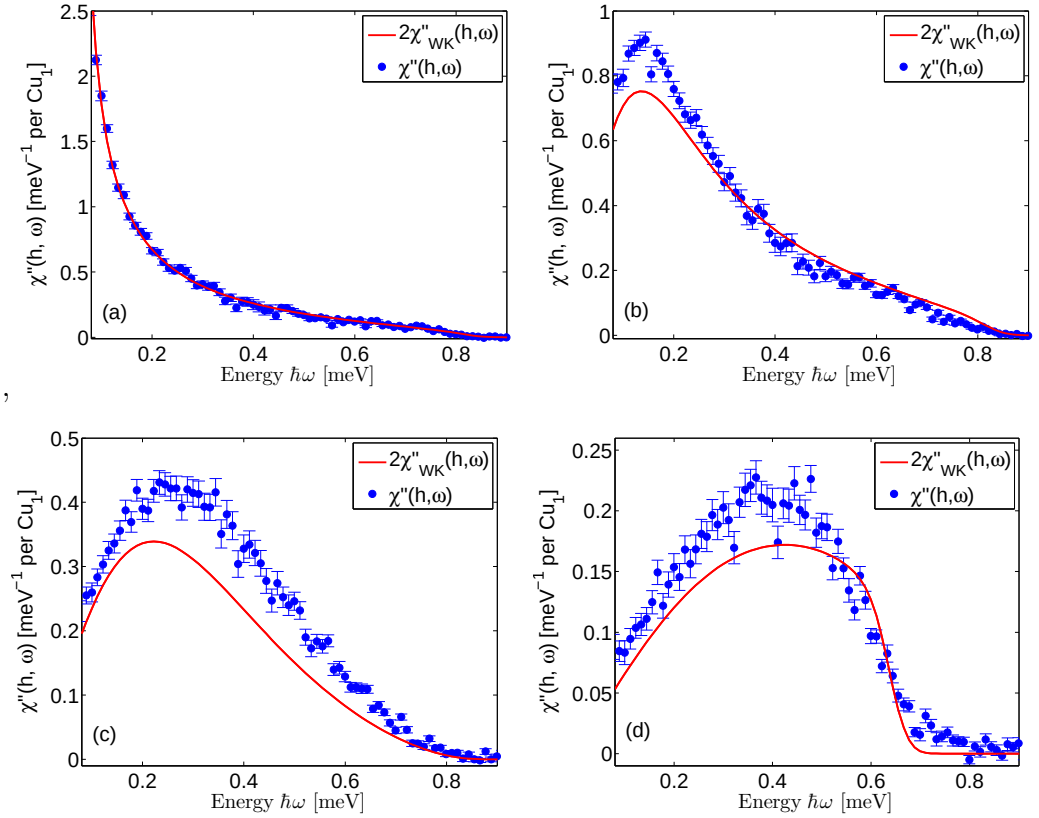

Figure 3.17: **Comparison between experimental and conformal field theory data.** The resolution-convoluted $\chi''_{WK}(\mathrm{h},\omega)$ calculated using equation (3.4) given by Werner and Klümper compared to scans at h $\in$ [0.495 0.505] with
(a) T = 0.15(2) = 0.050(7) J calculated using equations (3.4) and (3.5) and the parameters for T = 0, summarized in table 3.1.
(b) T = 0.79(3) = 0.263(8) J, and (c) T = 1.60(2) = 0.532(7) J, both calculated using equations (3.4) and (3.6). For these equations Werner and Klümper give parameters for T = 0.3 J and 0.5 J.
(d) A fit to the data at T = 3.18(5) = 1.06(2) J calculated using equations (3.4) and (3.6). The obtained parameters are given in table 3.3.
At higher temperatures, using equations (3.4) and (3.6), no parameters were found which could describe the data.

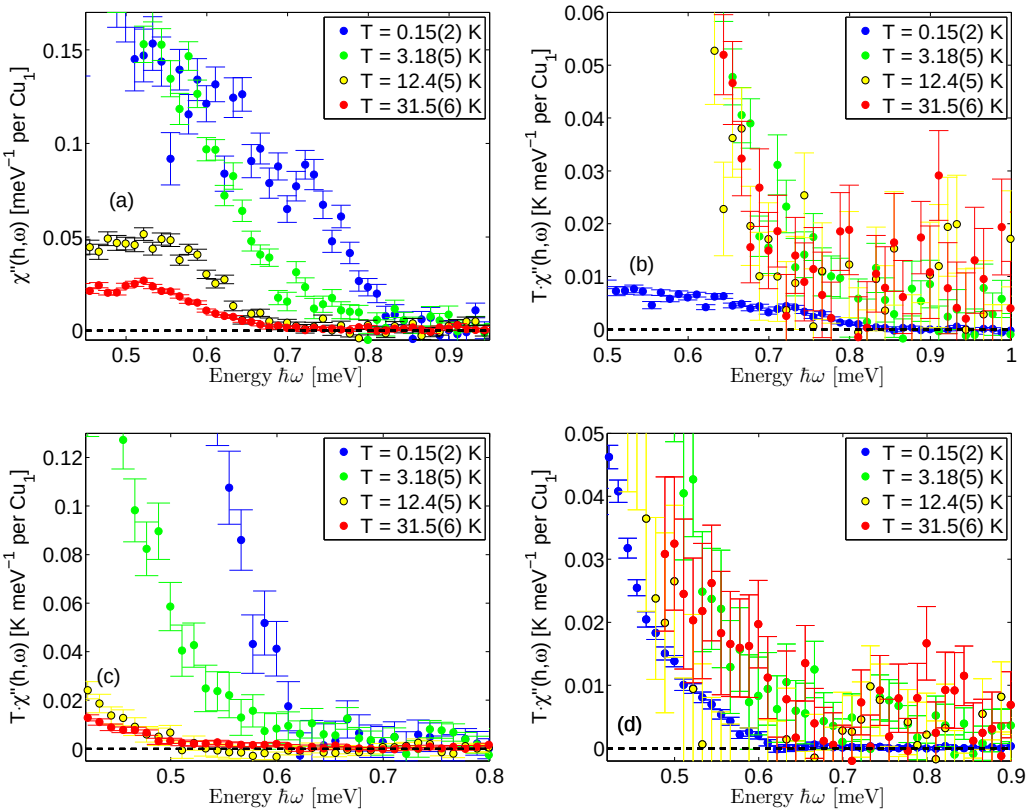

Figure 3.18: **Temperature dependence of the dynamic susceptibility.** (a) Dynamic susceptibility $\chi''(h,\omega)$ and (b) T·$\chi''(h,\omega)$ for different temperatures and h $\in$ [0.495, 0.505] and (c) $\chi''(h,\omega)$ and (d) T·$\chi''(h,\omega)$ for different temperatures and h $\in$ [0.745, 0.755].

scattering goes to zero at smaller energies for increasing temperatures, a closer look at (b) and (d) shows that this is not the case. This means that all the intensity is contained within the upper boundary of the two spinon continuum [72], and also suggests that the cutoff parameter Λ, as used by Werner and Klümper in equations (3.4) and (3.7) and summarized in table 3.1, does not change with temperature.

The peak positions for cuts of the dynamical susceptibility $\chi''(h,\omega)$ at different temperatures for h $\in$ [0.495, 0.505] and h $\in$ [0.745, 0.755] are compared in Figure 3.19. In Figure 3.19 (a) the peak positions move to higher energies for increasing temperatures. In Figure 3.19 (b) the position of the maximum moves to lower energies with increasing temperature. The peaks move to different values of energy transfer for different values of h with increasing temperatures, because with increasing temperature the intensity becomes more homogeneous within the upper boundary for the spinon continuum, and the intensity below the lower boundary of the spinon continuum increases, see Figure 3.7. Werner and Klümper [114] predict the shifting of the peak at h = 0.5 to higher energy transfer with increasing temperature, as is visible in the experimental data.

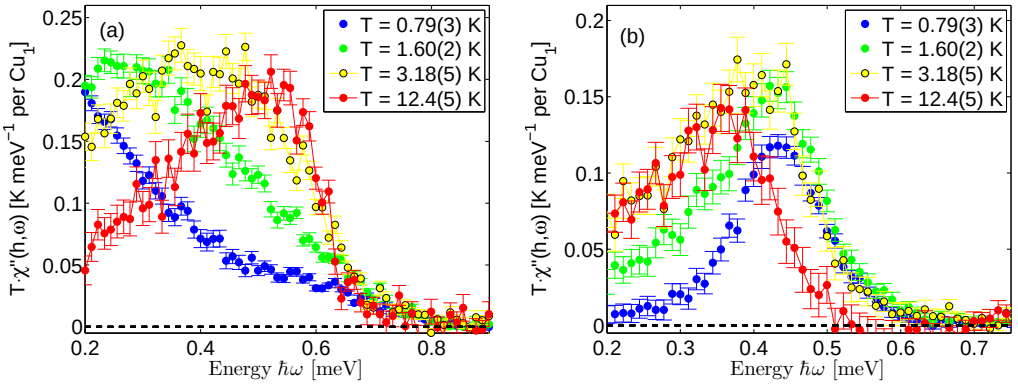

Figure 3.19: **Temperature dependence of the dynamic susceptibility**
(a) T·$\chi''(h,\omega)$ for different temperatures and h $\in$ [0.495, 0.505] and
(b) T·$\chi''(h,\omega)$ for different temperatures and h $\in$ [0.745, 0.755].

Quantum Monte Carlo (QMC) and maximum entropy data by Rahnavard and Brenig

The Quantum Monte Carlos and maximum entropy data from Rahnavard and Brenig [115] are resolution-convoluted as described for the data from Caux [76] in section 3.4.1. The experimental data are scaled with $\frac{1}{A_{2+4}}$ (see section 3.4.1), so that the experimentally obtained structure factor is $S(h,\omega) = S(h,\omega)_{\mathrm{Exp}}/A_{2+4}$. The resolution-convoluted structure factor calculated by Rahnavard and Brenig is called $S_{\mathrm{RB}}(h,\omega)$. Their results are compared to our normalized data in Figures 3.20 - 3.24.

Experimental data at T = 0.099(4) J are compared to QMC data at T = 0.1 J by Rahnavard and Brenig [115] in Figure 3.20. The shape of the structure factor is generally reproduced correctly by the Monte Carlo data. For most values of h, the calculated structure factor $2S_{\mathrm{RB}}(h,\omega)$ correctly describes the intensity, and the decrease in intensity with increasing energy. The wobbles in the Quantum Monte Carlo data arise from the uncertainty when $S_{\mathrm{RB}}(h,\tau)$ (calculated with quantum Monte Carlo) is transformed into $S_{\mathrm{RB}}(h,\omega)$ because of the analytical continuation of imaginary time data.

In Figure 3.21 experimental data at T = 0.263(8) J are compared to QMC data at T = 0.25 J. The intensity and its decrease with increasing energy transfer, as well as the general shape of the structure factor, are well reproduced by $2S_{\mathrm{RB}}(h,\omega)$. Already the peaks in the cuts appear broader, which can be explained by the intensity below ϵ_l increasing, this is well described by $2S_{\mathrm{RB}}(h,\omega)$.

Figure 3.22 shows a comparison between experimental data at T = 0.532(7) J and QMC data at T = 0.5 J. At this temperature the intensity below the lower boundary of the two-spinon continuum ϵ_l increases further. The Monte Carlo data agree with the experimental data, but the width of $2S_{\mathrm{RB}}(h,\omega)$ at T = 0.5 J is bigger than the width of the experimental structure factor. The intensity at negative energy transfer increases as well. This means that at this temperature the neutrons not only transfer

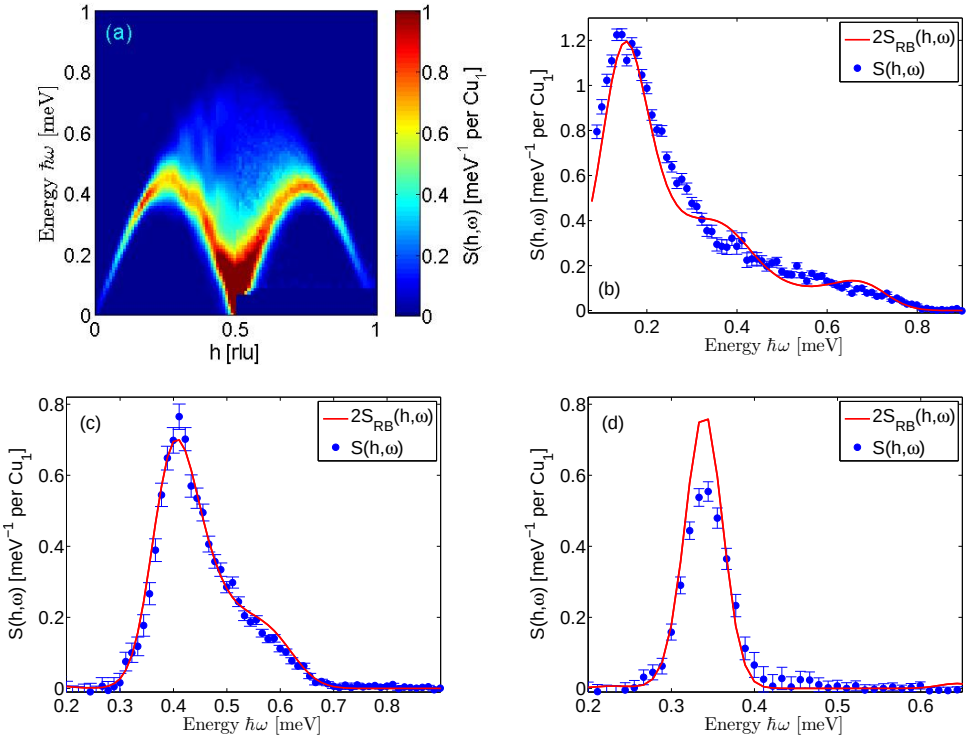

Figure 3.20: **Comparison between experimental and QMC data for T = 0.099(4) J.** (a) Left side (h <0.5): $2S_{\mathrm{RB}}(h,\omega)$ calculated by Rahnavard and Brenig [115] for T = 0.1 J and right side (h >0.5): $S(h,\omega)$ measured on IN5 at 0.30(1) K = 0.099(4) J. (b) Cut at h $\in$ [0.545 0.555], (c) cut at h $\in$ [0.695, 0.705] and (d) cut at h $\in$ [0.845, 0.855] for the same temperature.
The blue points are the experimentally determined $S(h,\omega) = S^{yy}(h,\omega) + S^{zz}(h,\omega)$, which are compared to the results from Rahnavard and Brenig (red line).

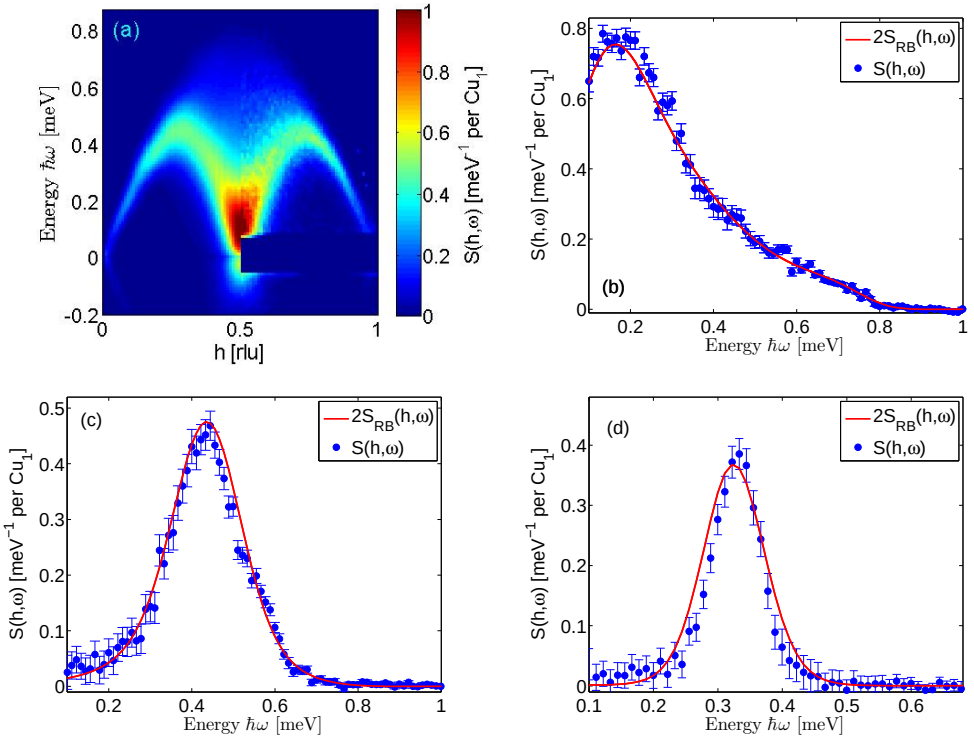

Figure 3.21: **Comparison between experimental and QMC data for T = 0.263(8) J.** (a) Left side (h <0.5): $2S_{\mathrm{RB}}(h,\omega)$ calculated by Rahnavard and Brenig [115] for T = 0.25 J and right side (h >0.5): $S(h,\omega)$ measured on IN5 at 0.79(3) K = 0.263(8) J. (b) Cut at h $\in$ [0.545 0.555], (c) cut at h $\in$ [0.695, 0.705] and (d) cut at h $\in$ [0.845, 0.855] at the same temperature.
The blue points are the experimentally determined $\mathrm{S}(h,\omega) = S^{yy}(h,\omega) + S^{zz}(h,\omega)$, which are compared to the results from Rahnavard and Brenig (red line).

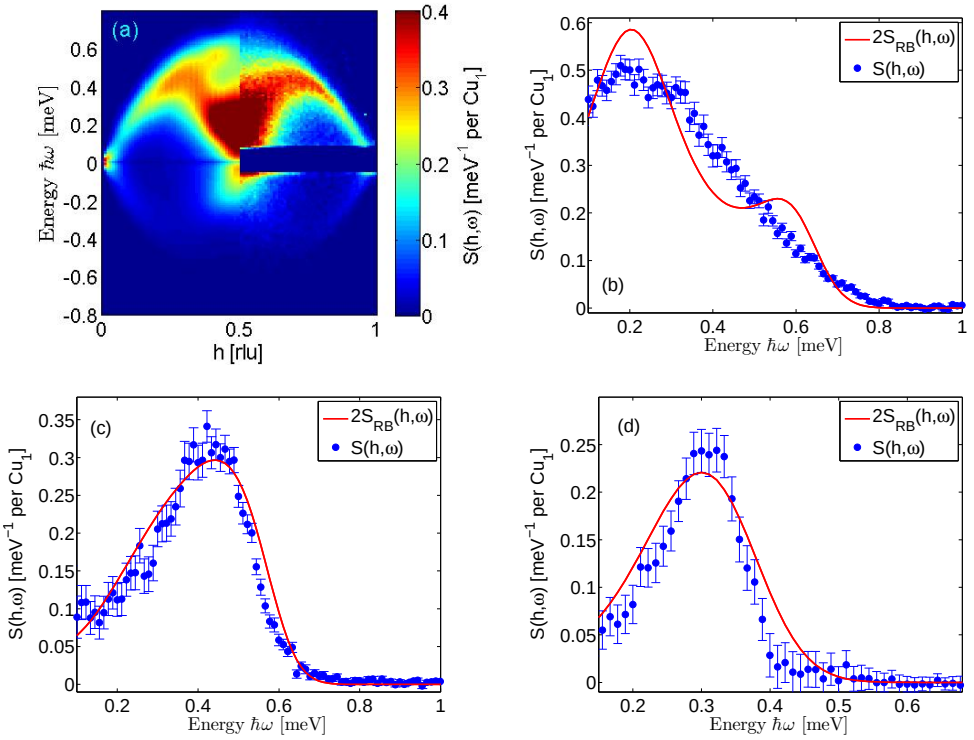

Figure 3.22: **Comparison between experimental and QMC data for T = 0.532(7) J.** (a) Left side (h <0.5): $2S_{\mathrm{RB}}(h,\omega)$ calculated by Rahnavard and Brenig [115] for T = $J/2$ and right side (h >0.5): $S(h,\omega)$ measured on IN5 at 1.60(2) K = 0.532(7) J. (b) Cut at h $\in$ [0.545 0.555], (c) cut at h $\in$ [0.695, 0.705] and (d) cut at h $\in$ [0.845, 0.855] at the same temperature.
The blue points are the experimentally determined $S(h,\omega) = S^{yy}(h,\omega) + S^{zz}(h,\omega)$, which are compared to the results from Rahnavard and Brenig (red line).

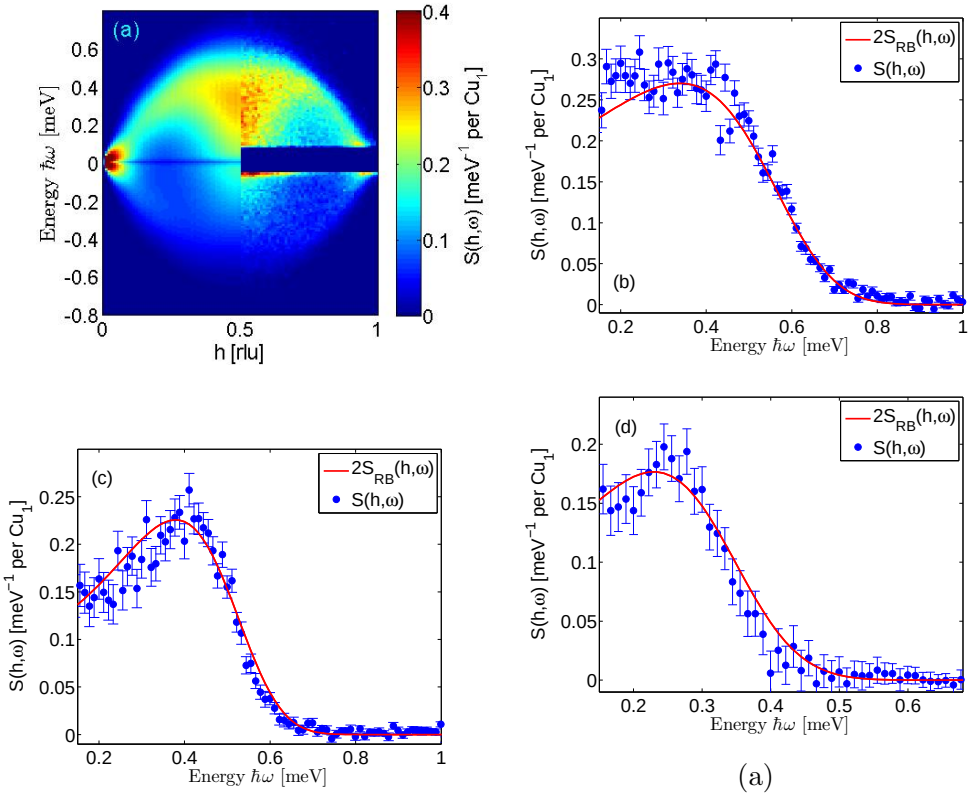

(a)

Figure 3.23: **Comparison between experimental and QMC data for T = 1.06(2) J.** (a) Left side (h <0.5): $2S_{\mathrm{RB}}(h,\omega)$ calculated by Rahnavard and Brenig [115] for T = J and right side (h >0.5): $S(h,\omega)$ measured on IN5 at 3.18(5) K = 1.06(2)J . (b) Cut at h ∈ [0.545 0.555], (c) cut at h ∈ [0.695, 0.705] and (d) cut at h ∈ [0.845, 0.855] at the same temperature. The blue points are the experimentally determined $S(h,\omega) = S^{yy}(h,\omega) + S^{zz}(h,\omega)$, which are compared to the results from Rahnavard and Brenig (red line).

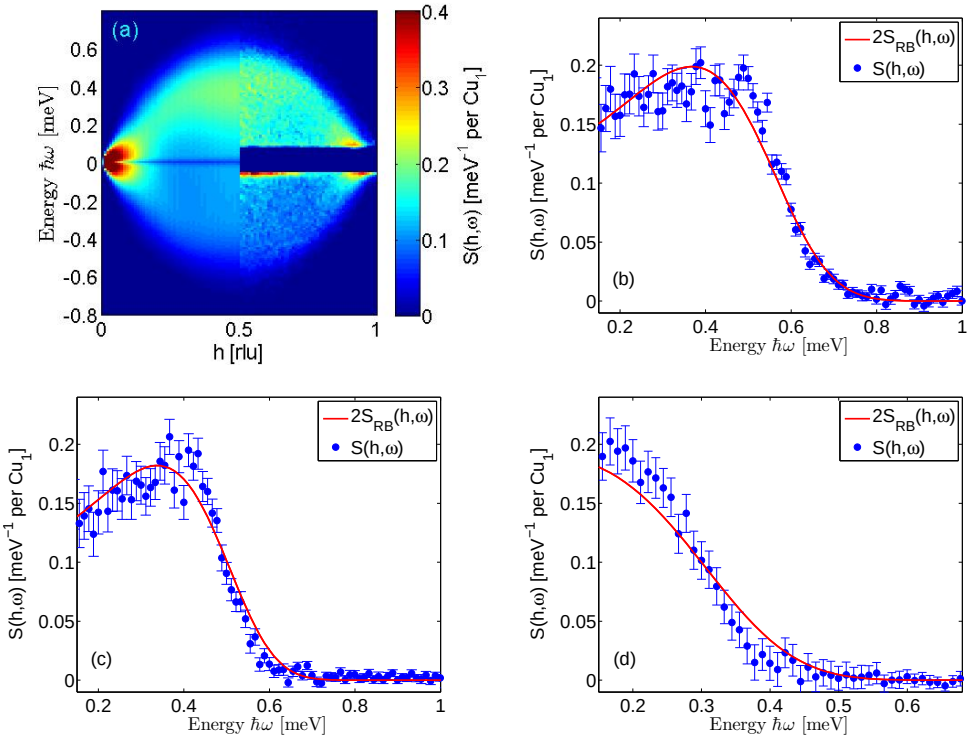

Figure 3.24: **Comparison between experimental and QMC data for T = 2.04(6) J.** (a) Left side (h <0.5): $2S_{\mathrm{RB}}(h,\omega)$ calculated by Rahnavard and Brenig [115] for T = 2 J and right side (h >0.5): $S(h,\omega)$ measured on IN5 at 6.2(2) K = 2.04(6) J. (b) Cut at h $\in$ [0.545 0.555], (c) cut at h $\in$ [0.695, 0.705] and (d) cut at h $\in$ [0.845, 0.855] at the same temperature. The blue points are the experimentally determined $S(h,\omega) = S^{yy}(h,\omega) + S^{zz}(h,\omega)$, which are compared to the results from Rahnavard and Brenig (red line).

energy to the sample, but can also gain energy from it. The wiggles in the Monte Carlo data arise from the uncertainty when $S_{\mathrm{RB}}(h,\omega)$ (calculated with quantum Monte Carlo) is transformed into $S_{\mathrm{RB}}(h,\omega)$ because of the analytical continuation of the imaginary time data.

A comparison between experimental data at T = 1.06(2) J and QMC data at T = J is shown in Figure 3.23. $S_{\mathrm{RB}}(h,\omega)$ shows good agreement with the experimental data. At this temperature the intensity below the lower boundary of the two-spinon continuum ϵ_l increases further. Spectral weight shifts from the antiferromagnetic zone center towards h $\rightarrow$ 0 and 1 where increased intensity can be observed.

Experimental data at T = 2.04(6) J are compared to QMC data at T = $2J$ in Figure 3.24. Even at T = 2 J the experimental structure factor is described correctly by the theoretical structure factor $S_{\mathrm{rB}}(h,\omega)$. The intensity is still limited by the upper boundary ϵ_u of the two-spinon continuum. Within this boundary the intensity is almost independent of h, with the exception of the higher spectral weight at low energies and h $\rightarrow$ 0 and 1.

The resolution-convoluted structure factor $S_{\mathrm{RB}}(h,\omega)$ by Rahnavard and Brenig [115] describes the intensity and its decrease with increasing energies for all temperatures compared in this chapter. The increase in intensity below the lower boundary for the two-spinon continuum ϵ_l with increasing temperature, and the boundaries of the scattering, are reproduced correctly by the theoretical results. For all measured temperatures a continuum is observed. The increased intensity close to h $\rightarrow$ 0, 1 is studied closer in the section about long-wavelength dynamics.

Static structure factor $S(h)$ and susceptibility $\chi'(h)$

Grossjohann and Brenig [86] use sum rules to assess the quality of the analytic continuation in their calculations. Here we compare our data and the structure factor calculated by Rahnavard and Brenig [115] to their scaling relations (3.8) and (3.9).

The parameters D_S and D_χ are given for the unconvoluted QMC data from Grossjohann and Brenig [86]. Therefore D_S and D_χ need to be adapted for comparison with the experimentally obtained data. Due to normalization considerations and the fact that, in practice, one measures $S(h,\omega) = S^{yy}(h,\omega)+S^{zz}(h,\omega)$, both the structure factor and the susceptibility have to be corrected by a factor $\pi/2$. Instead of multiplying the static structure factor and susceptibility by $\pi/2$, D_S and D_χ can be divided by $\pi/2$. This allows for easy comparison with the scaling relations (3.8) and (3.9).

These scaling relations use the static structure factor $S(h)$ and the static susceptibility χ'(h), which one can obtain by an integral transformation of the dynamic structure factor given by equations (2.4) and (2.5) in section 2.3.4. In order to compare our data with the scaling relations, cuts at h $\in$ [0.495, 0.505] are made and the data between -0.1 meV and 0.1 meV, where the incoherent scattering was subtracted improperly, are replaced by a linear interpolation. The interpolation is done for the dynamic susceptibility, since it is easier to interpolate χ''(h,ω), see Figure 3.25. The result is then transformed to the dynamic structure factor using the fluctuation-dissipation theorem described in sections 2.3.3 and 3.3.4. Interpolation is not possible in $\chi''(h,\omega)$ at the two lowest temperatures, T = 0.15(2) and T = 0.30(1) K. For T = 0.15(2) K, $S(h,\omega)$ is interpolated between -0.1 and 0.1 meV using the resolution-convoluted two- plus four-spinon structure factor calculated by Caux [76]. The data for T = 0.30(1) K were omitted from the comparison with these scaling relations.

The static structure factor and susceptibility were calculated using equations (2.4) and (2.5). Comparisons of the static structure factor and susceptibility with the scaling relations (3.8) and (3.9) are shown in Figure 3.26.

The experimentally determined static susceptibility χ'(h) agrees less well with the scaling relation (3.8) than the resolution convoluted QMC data by Rahnavard and Brenig [115]. The experimentally determined static structure factor S(h) agrees with the scaling relation (3.8) for temperatures up to 4 J, but deviates strongly from equation (3.8) for 10 J.

A possible explanation for this could be that small interpolation errors are blown up when χ''(h,ω) is transformed into S(h,ω). To test if interpolation errors explain this discrepancy, the static structure factor S(h) and susceptibility χ'(h) are calculated for the experimental data, and the QMC data from Rahnavard and Brenig, with an integration range starting at 0.1 meV. The interpolated data are below this energy, so using this method they are not taken into account. Then the scal-

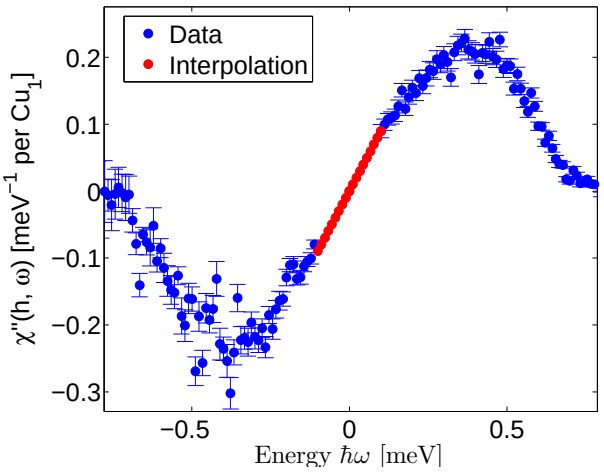

Figure 3.25: **Linear interpolation of the dynamic susceptibility** χ''(h,ω), h $\in$ [0.495, 0.505], at T = 3.18(5) K.

ing relations (3.8) and (3.9) are fitted to $S(h)_{RB}$, and $\chi'(h)_{RB}$ obtained with the method mentioned above for the resolution-convoluted QMC data from Rahnavard and Brenig [115] for energies bigger than 0.1 meV. This leads to the new values D_S = 0.072(2) and D_χ = 0.1175(7). The experimentally determined static structure factor $S(h)$ and susceptibility $\chi'(h)$, with the integration range $>$ 0.1 meV, are compared to the scaling relations with these new parameters in Figure 3.27.

The experimental static structure factor and susceptibility do not agree better with the reparametrized scaling relation (Figure 3.27) than with the original one (Figure 3.26). Therefore, possible interpolation errors do not explain all discrepancies between QMC and experimental data.

Another possible explanation is that with increasing temperature, less spectral weight shifts from the antiferromagnetic zone center at h = 0.5 than predicted by Rahnavard and Brenig [115]. But in the region with increased intensity, close to h $\rightarrow$ 0,1 at 6.2(2) K, no noticeable difference between theory and experiment was observed, see e.g. Figure 3.24.

The deviation in χ'(h) is less pronounced because of the division by ω in equation (2.5).

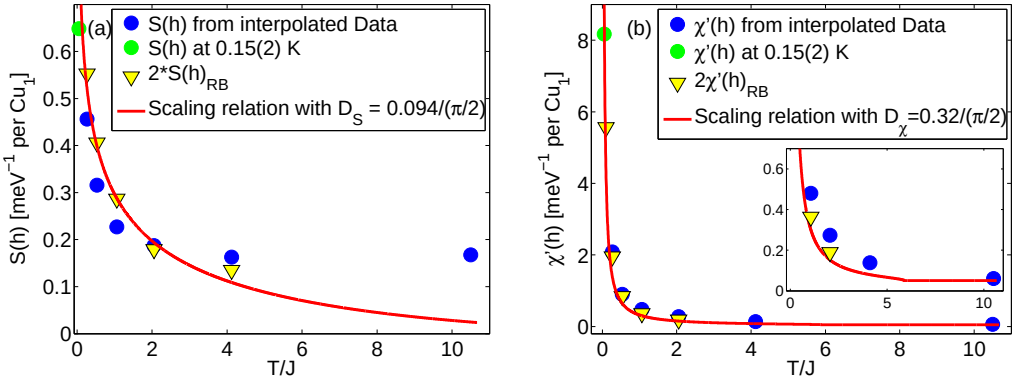

Figure 3.26: **Comparison between experimental data and scaling relations.** (a) Comparison of the measured static structure factor (blue points) to the scaling relation (3.8) with $D_S/(\pi/2)$. (b) Comparison of the experimentally determined static susceptibility, calculated using equation (2.5), with the scaling relation (3.9) and $D_\chi/(\pi/2)$. The data are interpolated in $\chi''(h,\omega)$ between -0.1 meV and 0.1 meV where the incoherent scattering is not properly subtracted from the data. The error bars are smaller than the symbols.
The green points are the static structure factor, respectively susceptibility at 0.15(2) K, interpolated using the exact two- plus four-spinon structure factor calculated by Caux [76]. The triangular symbols are twice the static structure factor $S(h)_{RB}$, respectively susceptibility $\chi'(h)_{RB}$ calculated from the resolution-convoluted QMC data from Rahnavard and Brenig [115].

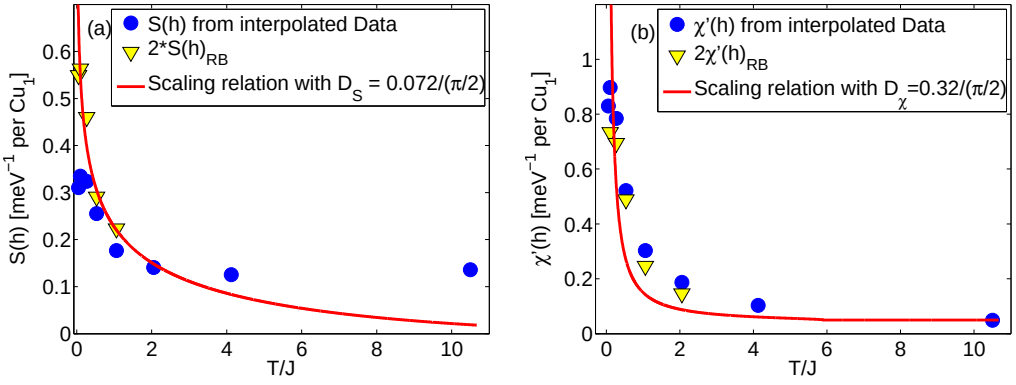

Figure 3.27: **Comparison between experimental data and scaling relations.** (a) Comparison of the measured static structure factor (blue points) to the scaling relation (3.8) with $D_S = 0.064(2)/(\pi/2)$. The integration in (2.4) started at 0.1 meV in order to rule out possible errors from interpolation. (b) Comparison of the experimentally determined static susceptibility (blue points) with the scaling relation (3.9) and $D_\chi = 0.137(7)/(\pi/2)$. Integration in (2.5) started at 0.1 meV in order to rule out possible errors from interpolation.
S(h) and χ'(h) at the two lowest temperatures, 0.15(2) and 0.30(1) K, are lower than for higher temperatures, because at low temperatures a bigger ratio of spectral weight is cut out. The triangular symbols are twice the static structure factor $S(h)_{RB}$, respectively susceptibility $\chi'(h)_{RB}$ calculated from the resolution-convoluted QMC data from Rahnavard and Brenig [115]. Again, integration in (2.4) and (2.5) started at 0.1 meV.

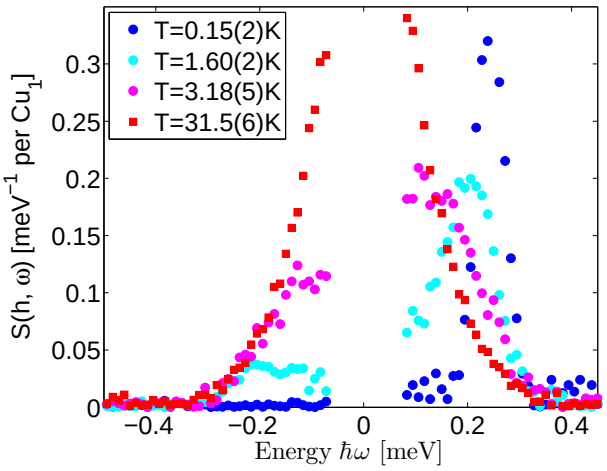

Figure 3.28: **Temperature dependence of the long-wavelength dynamics.** $S(h, \omega)$ from cuts at h $\in$ [0.895 0.905] and different temperatures. The intensity at h $\rightarrow$ 1 is temperature dependent.

Long-wavelength dynamics

With increasing temperatures spectral weight shifts from the antiferromagnetic zone center to $\hbar\omega \rightarrow 0$ and h $\rightarrow$ 0,1, as can be seen in Figure 3.7. The question whether the long-wavelength dynamics in Heisenberg chains can be described by spin diffusion has long been discussed.

Because of the temperature independent intensity at h close to zero, discussed in section 3.3.5, only data with h $\rightarrow$ 1 were studied. The temperature dependence of the increased intensity for h $\rightarrow$ 1 is easily visible in Figure 3.28.

The increased intensity close to h $\rightarrow$ 1 could be caused by the copper subsystem which forms the magnetic chains, by phonons, or it could be an additional Bragg peak. The positions of Bragg peaks were calculated, and do not agree with the observed signal. In order to determine whether this contribution to the signal comes from the copper subsystem, which forms the magnetic chains, or from phonons, the total spectral weight for each temperature is calculated by integrating over the whole h- and ω-range. To do this, cuts from S(h, ω) with width 0.01 between h = 0.5 and 0.95 are taken and summed up over h. Because the step width in h is constant, one can use

$$S(\omega) = \sum_{h=0.5}^{0.95} S(h, \omega)\Delta h.$$

Where the incoherent scattering could not be completely removed, in the energy range between -0.1 to 0.1 meV, it was cut out in S(ω) and replaced by a linear interpolation in $\chi''(\omega)$, before the data were transformed into S(ω) again using equation (2.3), see section 2.3.3. The data were interpolated in χ'', because it is easier and

more reliable due to the linear energy dependence of χ'' close to $\hbar\omega = 0$. At the three lowest temperatures, 0.15(2) K, 0.30(1) K and 0.79(3) K, linear interpolation in $\chi''(\omega)$ was not possible, therefore the data were interpolated in S(ω) for these temperatures. The resulting $S(\omega)$ was summed over the energy range from -1.3 meV to 1.3 meV using the equation

$$S_{\mathrm{Sum}} = \sum_{\hbar\omega=-1.3\mathrm{meV}}^{1.3\mathrm{meV}} S(\omega)\Delta\omega$$

and compared with the spectral weight calculated using the convoluted and normalized two- and four-spinon continuum by Caux [76]. The data were normalized with the scaling factor A_{2+4} determined in section 3.4.1. Due to the integration range h $\in$ [0.5, 0.95] and the normalization, the total expected spectral weight is $\frac{1}{2}\frac{2}{3}$S(S+1) = 0.25 since S = 1/2 for $CuSO_4$*5D_2O. The integration range was chosen to finish at h = 0.95 because for higher h the energy cutoff is too low be able to safely distinguish between magnetic and incoherent scattering. The results are shown in Table 3.4.

Temperature [K]	S_{Sum}
31.5(6)	0.224(10)
12.4(5)	0.228(6)
6.2(2)	0.23(1)
3.18(5)	0.24(3)
1.60(2)	0.25(3)
0.79(3)	0.25(2)
0.30(1)	0.25(2)
0.15(2)	0.25(2)
Caux *	0.251(8)

Table 3.4: Results of summing the data over the whole h- and ω-range. * The two- and four-spinon structure factor calculated by Caux is convoluted with the resolution function and normalized as described in section 3.4.1.

The difference between the highest and lowest calculated spectral weight is less than 15%. The lower spectral weight observed at higher temperatures is due to the fact that only data up to h = 0.95 were taken into account, and that more spectral weight can be seen at h $\rightarrow$ 1 at high temperatures. For phonons, the spectral weight would increase with increasing temperature. This small variation in the measured spectral weight hints that the increased intensity close to h $\rightarrow$ 0,1 does indeed originate from the copper subsystem which forms the magnetic chains. Cuts at different wave vectors show that this increased intensity changes its form with changing wave vector h, see Figure 3.29.

In order to determine if the increased intensity arises from spin diffusion, it was fitted using equation (3.10) by Marshall and Lowde [125]. Before equation (3.10) was fitted to the data, it was convoluted with the resolution function as described

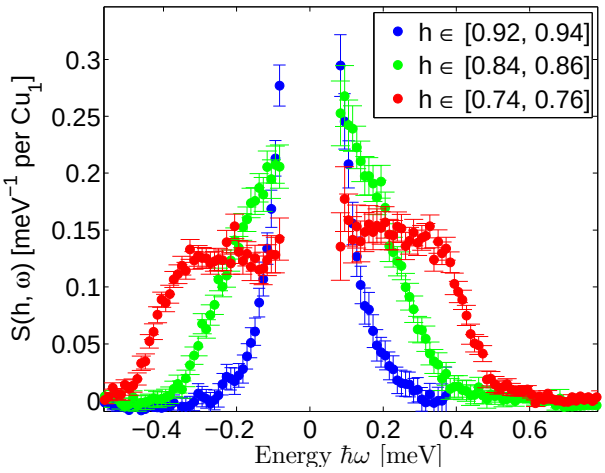

Figure 3.29: **Long-wavelength dynamics for different wave vectors.** Cuts at T = 31.5(6) K through the region with increased intensity close to h → 1 with different wave vectors. The width and shape change with varying wave vector.

in section 3.4.1. Fits are done at T = 31.5(6) K and for h close to 1. Two fits are shown in Figure 3.30.

Fits using equation (3.10) do not fit well to the measured data, even though the shape of the experimental data is similar to the fit. Hence, we cannot conclude that the increased intensity close to h = 1 comes from spin diffusion. To clarify this question, further investigation of this phenomenon is necessary.

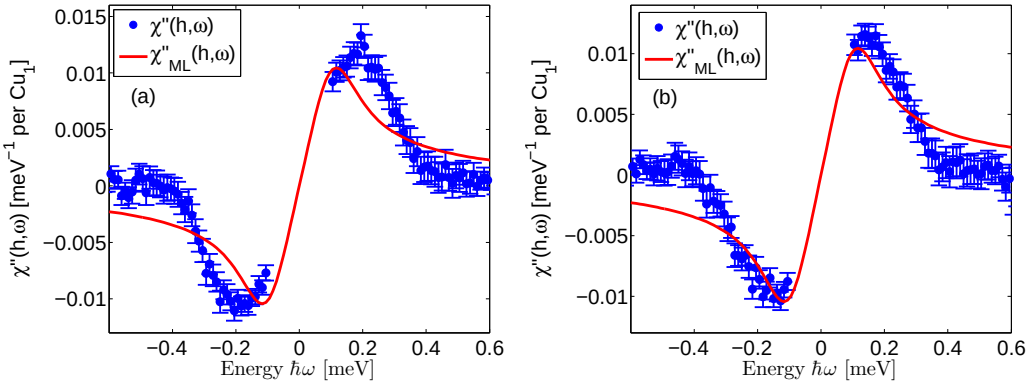

Figure 3.30: **Fits for the long-wavelength dynamics.** Fits using equation (3.10) to cuts at T = 31.5(6) K with (a) h ∈ [0.845 0.855] and (b) h ∈ [0.865 0.875].

3.5 Discussion

Fitting the resolution convoluted two- and four-spinon dynamical structure factor calculated by Caux to the data at 150 mK permits to find the scaling factor A_{2+4} for an absolute normalization of the data onto the Cu_1^{2+} spin. The parameters for the resolution function and the exchange J are determined as well by these fits. Using this scaling factor, resolution function and J, the data at finite temperatures can be compared absolutely to theoretical predictions.

The two- and four-spinon dynamical structure factor calculated by Caux [76] describes the low temperature behavior of $CuSO_4$*$5D_2O$ correctly, as already shown by [72]. Werner and Klümper [114] found a simpler expression for the structure factor at T = 0 given in equations (3.4) and (3.5). This theoretical structure factor fits similarly well to the cut at h ∈ [0.495, 0.505] at T = 0.15(2) K as the two- and four-spinon dynamical structure factor calculated by Caux. For high energies, the results by Caux, and by Werner and Klümper, are nearly identical and only deviate noticeably below 0.3 meV. At even lower energies, $\hbar\omega < 0.1$ meV, the structure factor calculated by Werner and Klümper starts to deviate further than the error bars. This shows that the two- plus four-spinon continuum at low temperatures can be described by a quite simple expression, given by equations (3.4) and (3.5), for a relatively big energy range when the cut-off is chosen appropriately. Equations (3.4) and (3.6) by Werner and Klümper show agreement with cuts from the experimental data at h ∈ [0.495, 0.505] also for finite temperatures up to T = 3.18(5) K, which corresponds to T ∼ J. This is already above the crossover temperature, which is given as $T^* = 0.7\ J$. The fits however break down for T > J. Equation (3.7) did not fit the data, but comparing numerical results from Werner and Klümper to our experimental data shows that experimental data at 31.5(6) K, which corresponds to T ∼ 10 J, show good agreement with their numerical data for T ∼ ∞. We expect therefore for $CuSO_4$*$5D_2O$ good agreement with these numerical results even for T ≫ 10 J and that even at these temperatures spin correlations are important.

The scaling relation by Schulz [104] given in equation (3.1) shows good agreement with the data up to temperatures of the order of J, i.e. intermediate temperatures. This is higher than the range given by Schulz, who states that (3.1) is valid for low temperatures, which usually means T < J. The temperature energy scaling for $CuSO_4$*$5D_2O$ collapses to a single curve given by equation (3.1) for energies between 0.2 and 0.5 meV and temperatures up to $2J$. This shows that the excitation spectrum of $CuSO_4$*$5D_2O$ is similar to the excitation continuum of the 1D LL.

Introducing logarithmic corrections for umklapp scattering, as done by Starykh, does not improve agreement between experimental data and the theoretically calculated structure factor. Equation (3.2) by Starykh [105, 110, 111] reproduces the shape of the continuum at h ∈ [0.495, 0.505] for temperatures smaller or equal to ≈ 0.25 J, but overestimates the intensity, especially at low temperatures and low energies.

Equation (3.3) given by Barthel [112] was originally proposed for the Bose-Hubbard model, and only follows the experimental data at the lowest measured temperature, 0.15(2) K, which is the temperature where the parameters are fitted.

The scaling relations for the static structure factor and the static susceptibility with the parameters given by Starykh [105] agree with quantum Monte Carlo data by Rahnavard and Brenig [115]. Good agreement for all temperatures is found between the static susceptibility and the scaling relation. The static structure factor S(h) also agrees with the sum rule, except at the highest measured temperature . A possible explanation is that, in reality, less spectral weight shifts from the antiferromagnetic zone center than predicted by Rahnavard and Brenig [115]. But in the region with increased intensity up to temperatures of 6.2(2) K, close to h $\rightarrow$ 0,1, no noticeable difference between the quantum Monte Carlo data by Rahnavard and Brenig and experimental data was found. Accounting for possible errors introduced by interpolation does not improve agreement between the scaling relation and dynamic susceptibility.

The dynamic structure factor of the antiferromagnetic spin-$\frac{1}{2}$ Heisenberg antiferromagnetic chain calculated by Rahnavard and Brenig [115] describes the behavior of $CuSO_4$*$5D_2O$ correctly. At low temperatures (T = 0.30(1) K and T = 1.60(2) K) the results from Grossjohann and Brenig show wiggles, which we do not observe. These wiggles arise from the uncertainty when $S_{RB}(h, \tau)$ (calculated with quantum Monte Carlo) is transformed into $S_{RB}(h, \omega)$, because of the analytic continuation of imaginary time data. At all temperatures for which quantum Monte Carlo results by Rahnavard and Brenig are available, $S_{RB}(h, \omega)$) is a qualitatively and quantitatively good description of the experimental data. The intensities, as well as the changing shape of the continuum, are reproduced correctly. The shifting of spectral weight below the lower boundary of the two-spinon continuum and away from the antiferromagnetic zone center to h $\rightarrow$ 0,1 with increasing temperature are also described. This shifting of spectral weight away from the antiferromagnetic zone center was predicted by Starykh [105] and Grossjohann and Brenig [86]. We could not determine definitely whether this increased intensity near h $\rightarrow$ 0, 1 at low energies is diffuse. The excitation spectrum of $CuSO_4$*5D2O shows excellent agreement with the excitation spectrum of a spin-$\frac{1}{2}$ Heisenberg antiferromagnetic chain, even at finite temperatures.

For all observed temperatures continuous scattering drops to zero at the same energy. So even at the highest measured temperature, the signal is well contained within the upper boundary of the two-spinon continuum [72]. This means that a spinon continuum is observed at all measured temperatures, and $CuSO_4$*$5D_2O$ behaves, even at 31.5(6) K, like a quantum magnet and not like a classical system at infinite temperatures, for which one would expect single spin flips.

- $CuSO_4$*$5D_2O$ is an excellent model material for the spin-$\frac{1}{2}$ Heisenberg antiferromagnetic chain.
- A spinon continuum is observed at all measured temperatures and therefore one can conclude that $CuSO_4$*$5D_2O$ behaves like a quantum magnet even at T $\sim 10J$, and not like a classical magnet at infinite temperatures, for which one would expect single spin flips.
- Quantitative and qualitative comparisons between experimental data and theoretical calculations across a range of temperatures were done.
- The dynamic structure factor for the excitation spectrum of the spin-$\frac{1}{2}$ Heisenberg antiferromagnetic chain calculated by QMC is a quantitatively good description of the experimental data.
- The increasing intensity at h $\rightarrow$ 0,1 and $\hbar\omega \rightarrow 0$ with increasing temperature, which is also predicted theoretically, arises from the same copper subsystem that forms the magnetic chains.
- Good agreement between the excitation spectrum of $CuSO_4$*$5D_2O$ and ω/T-scaling is observed up to T $\sim 2J$.
- Both static structure factor and static susceptiblity show good agreement with scaling relations for most temperatures.
- Numerical data for T $\rightarrow \infty$ and experimental data for T $\sim 10J$ show good agreement, and indicate that even for T $\gg J$ good agreement may be expected and that spin correlations are important at these temperatures.

Chapter 4

The quasi-1 dimensional Ising antiferromagnet $RbCoCl_3$

The Ising chain is probably one of the most studied models in magnetism. The simplest excitation in an Ising chain is flipping a spin. This gives rise to two domain walls which are a soliton-pair state. The Ising chain in a transverse magnetic field is probably the simplest realization of a quantum phase transition. Near its quantum critical point the ferromagnetic Ising chain $CoNb_2O_6$ shows a spectrum of bound states [13]. This motivates the investigation of similar physics in other model systems.

Candidates are from the family $ACoX_3$, with A = {Rb, Cs, Tl} and X = {Br, Cl} to which $RbCoCl_3$ belongs. Optical spectroscopy measurements indicate a lower energy for $RbCoCl_3$ than for other members of this family [3]. In order to experimentally access the quantum critical point, which is in this case the critical magnetic field, a low enough energy scale is needed.

In this chapter the magnetic structure of $RbCoCl_3$ is discussed and neutron scattering studies of the excitation spectrum of $RbCoCl_3$, which gives rise to bound states at low temperatures, and its temperature dependence are presented.

4.1 Introduction

4.1.1 Ising materials

One of the most studied models in magnetism is the Ising model. It is named after Ernst Ising, who studied a linear model of spins which can point only along one axis [152]. Ising found that the one dimensional case has no phase transition. Peierls predicted later that ferromagnetic order sets in at sufficiently low temperatures for the two dimensional Ising model [153]. This case was solved exactly by Lars Onsager [154].

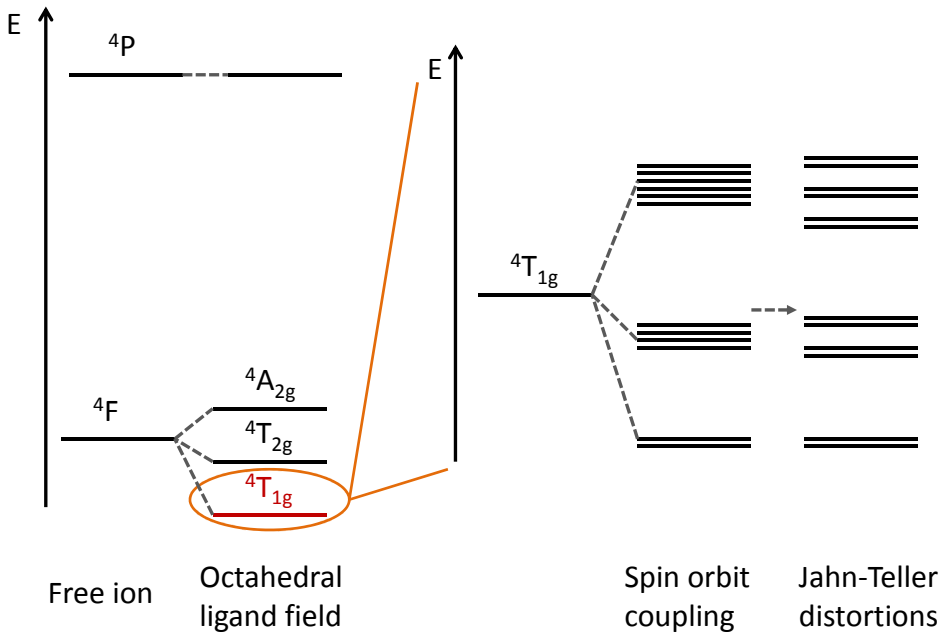

Figure 4.1: **Splitting of the energy levels of a free Co^{2+} ion**. The energy levels of a free Co^{2+} ion split under the influence of the ligand field, spin-orbit coupling and Jahn-Teller distortions. The resulting ground state has effective spin-$\frac{1}{2}$ [162].

Ions giving rise to Ising-like interactions

Because the spins in Ising materials can only point along one axis, ions giving rise to Ising-like interactions require large anisotropy. Since the magnetic moment varies with the g-value, the g-value anisotropy can be used to find Ising ions [130]. One ion which leads to Ising like interactions is Dy^{3+} [11] e.g. in the antiferromagnets DyAlGa [155] and $DyPO_4$ [156, 157]. Other model materials with Ising like interaction can be found, for example, in the lithium rare earth (R) tetrafluorides $LiRF_4$ for certain rare earths. $LiTbF_4$ and $LiHoF_4$ are Ising-like ferromagnets [158, 159]. The Co^{2+} ion is also a good resource for anisotropic model materials, and results in Ising- or sometimes XY-interactions [130, 160, 161].

The Co^{2+} ion

The ground state of the free Co^{2+} ion is the ^4F state with a spin of $\frac{3}{2}$, and the first excited state is the ^4P state. Under an octahedral ligand field, the free ion terms ^4F and ^4P split into a ground state $^4T_{1g}$ and excited states. A sketch of this splitting is shown in Figure 4.1.

Because the angular orbital momentum of Co^{2+} is not quenched, spin-orbit coupling must be taken into account. This leads to an additional splitting of the states obtained by ligand field splitting. The ground state $^4T_{1g}$ term is split into a ground

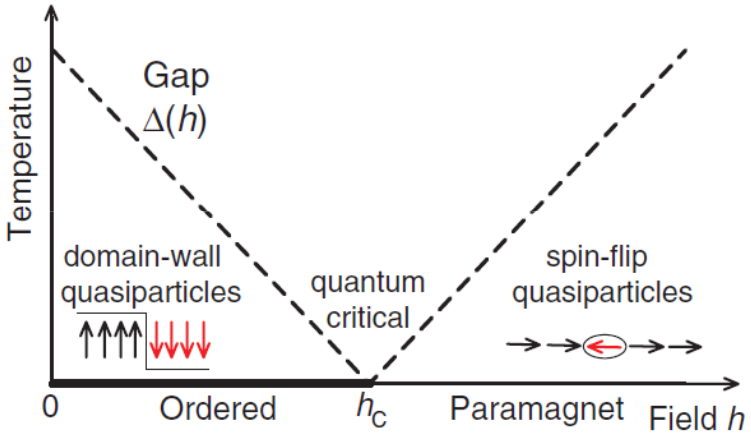

Figure 4.2: **Phase diagram of the Ising chain in a magnetic field**. At low transverse field the elementary excitations are pairs of domain walls. Above the critical field, in the paramagnetic phase, excitations are flipped spins. This Figure is taken from reference [13].

state Kramers doublet, a quartet and a sextet. The Jahn-Teller distortion of the octahedral ligand field leads to further splitting into six Kramers doublets. Since at low temperature only the lowest Kramers doublet is thermally populated, one can assume that octahedrally coordinated Co^{2+} ions have an effective spin of $\frac{1}{2}$ [130, 160–162]. Depending on the kind of distortion (stretching or compression) this spin can be of Ising- or XY-type. The anisotropy of the spin will depend on the relative magnitudes of the spin-orbit coupling and the crystal field [130, 163].

The Ising chain in a transverse magnetic field

Perhaps the simplest realization of a quantum phase transition is the Ising chain in a transverse magnetic field. At low transverse fields the elementary excitations are domain walls, and above the critical magnetic field the elementary excitations are flipped spins, as shown in Figure 4.2. Around the quantum critical point unconventional entangled scaling and critical scaling can occur [1]. The one-dimensional Ising model in a transverse field was studied theoretically by Pfeuty [164] and Sachdev [1], amongst others.

In order to study this quantum phase transition experimentally a good model material for an Ising chain is needed. Since the critical magnetic field depends on the energy scale (10 T $\approx$ 1 meV), the energy scale should be low enough so that the magnetic field strengths are still experimentally accessible. Coldea *et al.* studied a ferromagnetic Ising chain, $CoNb_2O_6$, near its quantum critical point where it displays a spectrum of eight particles, long predicted to appear near the critical point of an Ising chain [165]. In $CoNb_2O_6$ these effects are realized by the interchain coupling acting as a perturbation to the dominant Ising state [13, 166]. In contrast, in the three dimensional Ising magnet $LiHoF_4$ sharp spin-flip quasiparticles were observed

both above and below the critical field [159, 167]. The study of $CoNb_2O_6$ by Coldea *et al.* motivates the investigation of other Ising-like magnetic chains.

Another Ising chain which has been studied experimentally is $CsCoCl_3$ [59, 60]. For this compound, Shiba predicted the Néel phase to change into a spin-liquid like state with no long range order [168]. This has not been confirmed in $CsCoCl_3$ due to its rather high critical field, but is suspected to be responsible for an order to disorder transition in $BaCo_2V_2O_8$ [169]. Another Ising chain studied is $SrCo_2V_2O_8$ which shows two phase transitions with an applied magnetic field increasing in strength [12, 126].

The family $ACoX_3$

The family $ACoX_3$, with A = {Rb, Cs, Tl} and X = {Br, Cl}, is a class of potential Ising materials [11]. $CsCoBr_3$ [59, 62–64], $CsCoCl_3$ [59, 60, 170] and $TlCoCl_3$ [65–67] have been studied using neutron scattering. Those materials all have an in-chain interaction around $2J$ = 12.8 - 14.7 meV, an XY-component ϵ = 0.14 - 0.15, and order around 30 K. $RbCoCl_3$, which is studied in this chapter, has been studied less than these compounds. Magnetic susceptibility measurements indicated the energy scale $2J$ to be lower. A low enough energy scale is needed to experimentally access the critical magnetic field [3].

The excitation spectrum of $CsCoCl_3$ and $CsCoBr_3$ has been studied using neutron scattering [60, 62] and Raman spectroscopy [161, 171]. The weak interchain interaction present in these compounds leads to a set of discrete peaks being observed. Due to the lower energy scale of $RbCoCl_3$, and the better resolution of high resolution neutron spectroscopy, studying the excitations in $RbCoCl_3$ is expected to lead to a better understanding of the excitation spectrum of the Ising-like antiferromagnetic chain.

4.2 Excitations in Ising-like antiferromagnetic chains

The simplest excitation in a spin chain consists of flipping a spin, see section 1.2. The excitation spectrum of the spin-$\frac{1}{2}$ anisotropic Heisenberg antiferromagnet

$$\begin{aligned} H &= 2J \sum_j \left[S_j^z S_{j+1}^z + \epsilon \left(S_j^x S_{j+1}^x + S_j^y S_{j+1}^y \right) \right] \\ &= H_{ZZ} + H_{XY}, \end{aligned}$$

where ϵ is a measure for the anisotropy, was first determined for $\epsilon = 1$ by des Cloizeaux and Pearson [74] and is discussed for the spin-$\frac{1}{2}$ Heisenberg antiferromagnetic chain in section 1.2 and chapter 3. Here the excitation spectrum for the

Ising-like antiferromagnetic chain is introduced.

Villain [172] studied the spin dynamics of an Ising-like antiferromagnetic chain at low temperatures, and showed that it can be governed by the propagation of boundaries between antiferromagnetic one-dimensional domains (single-domain-wall description). At elevated temperatures, the motion of thermally activated domain walls should manifest itself as a central peak of the longitudinal response $S^{zz}(\mathbf{Q}, \omega)$ [172]. This peak has been observed by, amongst others, Hirakawa and Yoshizawa in $CsCoCl_3$ [173, 174] and Nagler in $CsCoBr_3$ [62]. If these excitations, consisting of domain walls, satisfy certain conditions they are called solitons. *"Essentially, solitons are quantized excitations of a classical, continuous system which are not scattered by solitons or other quasi-particles: they can be retarded or accelerated during the collision, but the velocity (and shape) at the end of the collision is the same as before"* [61].

Mikeska [175] suggested that solitons can be observed by inelastic neutron scattering. A first experiment on the ferromagnetic chain $CsNiF_3$ was carried out by Kjems and Steiner [176] in 1978, but the result is controversial. Regnault, Boucher *et al.* could prove the existence of solitons, showing that the domain walls in the antiferromagnetic chain $(CD_3)_4NMnCl_3$ propagate freely, by studying the lifetime of antiferromagnetic excitations [177, 178]. Figure 4.3 shows a sketch of a magnon decaying into two solitons and the resulting dispersion.

Ishimura and Shiba [179] studied the spin dynamics of one dimensional Ising-like antiferromagnets, using perturbation theory up to first order in ϵ and exact calculations for finite chains (domain-wall-pair description). Shiba expanded the model to take interchain interactions into account. These models are explained in more detail in section 4.2.1. Other models were established to describe experimental results. Johnstone *et al.* [171] studied the Ising-like antiferromagnetic chain $CsCoBr_3$ using Raman spectroscopy. They postulated that the interchain interaction modifies the Co^{2+} levels, and implemented this by changing the nearest neighbor interchain interaction J_{IC} for every peak. Lehmann *et al.* [161] studied $CsCoCl_3$ and $CsCoBr_3$ using Raman spectroscopy, and implemented the modification of Co^{2+} levels by changing ϵJ for every peak. Jörke and Dürr [180] compared FIR spectroscopy results for $RbCoCl_3$ with the theories by Johnstone and Lehmann and found reasonably good agreement. Nagler [62] extended the perturbation theory by Ishimura and Shiba to finite temperatures, and the results compare reasonably well to inelastic neutron scattering data for the one-dimensional Ising-like antiferromagnet $CsCoBr_3$. They also found experimental evidence for ideal soliton gas behavior near the antiferromagnetic zone center, suggested by Maki [181].

Matsubara [182] studied the quasi one-dimensional antiferromagnets $CsCoCl_3$, $CsCoBr_3$ and $RbCoCl_3$ using Raman scattering. He introduced an extension to Shibas model, which removes the discrepancies observed between experimental and theoretical results in earlier theories. This theory is presented in more detail in section 4.2.1. Goff [60] introduced a term arising from exchange mixing to explain

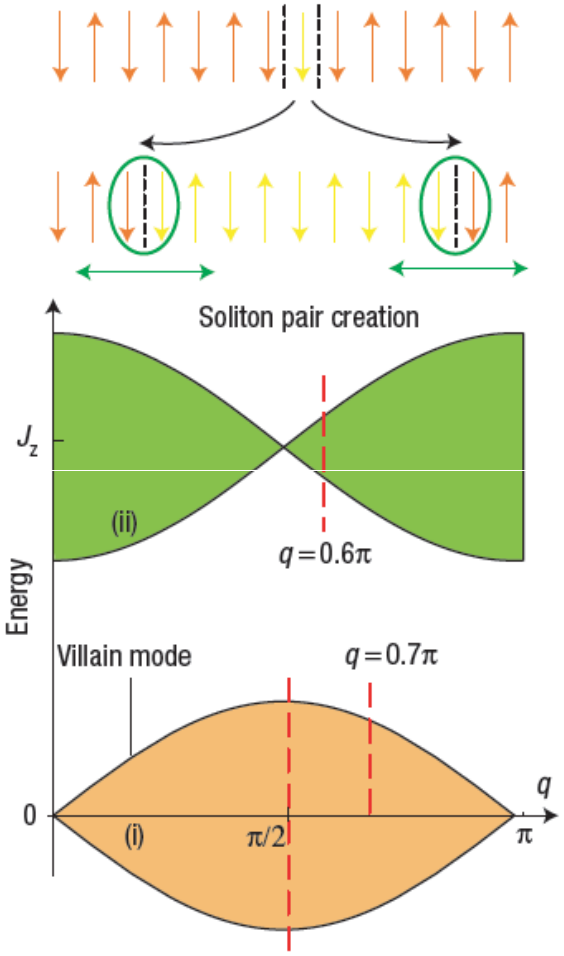

Figure 4.3: **Sketch of solitons and the resulting dispersion.**
Top: A magnon decaying into two solitons (domain walls).
Bottom: With neutron scattering one can observe two continua arising from soliton pairs. The low lying continuum is called a "*Villain mode*", it is due to neutrons scattering on thermally excited solitons. The continuum at higher energies arises due to the creation of a pair of solitons which leads to a gapped dispersion. This Figure is from reference [64]. J_z corresponds to J, and the red lines indicate scans in reference [64].

neutron scattering results in $CsCoCl_3$. This theory is also presented in more detail in section 4.2.1.

4.2.1 Theoretical models

The isolated chain model

For the Ising-like antiferromagnet, ϵ is much smaller than 1 and can be treated as a perturbation. Ishimura and Shiba [179] studied the dynamics of the one dimensional Ising like antiferromagnet using perturbation theory up to first order in ϵ. This model only treats isolated chains. For a chain of N ions Ishimura and Shiba find the matrix elements

$$\langle \nu, \mathrm{Q} \left| H \right| \nu', \mathrm{Q} \rangle = \begin{cases} 2J & \text{for } \nu' = \nu, \\ \mathrm{V} & \text{for } \nu' = \nu + 1, \\ \mathrm{V}^* & \text{for } \nu' = \nu - 1, \\ 0 & \text{otherwise,} \end{cases} \tag{4.1}$$

where $\mathrm{V} = \epsilon J \left(1 + e^{-2\pi i \mathrm{Q}}\right)$ and ν is the number of reversed spins. The dynamic spin correlation function $\mathrm{S}^{\alpha\alpha}(\mathrm{Q}, \omega)$, α= x or z, can be written as

$$\mathrm{S}^{\alpha\alpha}(\mathrm{Q}, \omega) = \sum_f \left| \left\langle f \left| S^\alpha_{\mathrm{Q}} \right| g \right\rangle \right|^2 \delta \left(\omega - E_\mathrm{f} + E_\mathrm{g} \right),$$

where E_g and E_f are the energies of the ground state and the excited state, $|g\rangle$ is the ground state, and $|f\rangle$ is an excited state connected by the spin fluctuation operator $\mathrm{S}^\alpha_\mathrm{Q} = N^{-1/2} \sum_j e^{i \mathrm{Q}_j} S^\alpha_j$. The ground state is given by perturbation theory as

$$|g\rangle \approx \Psi_{\mathrm{Neel1}} + \frac{1}{E_0 - H_{ZZ}} H_{XY} \Psi_{\mathrm{Neel1}},$$

and

$$\mathrm{S}^+_\mathrm{Q} |g\rangle \approx \frac{1}{\sqrt{2}} \left(1 - \epsilon \cos\left(2\pi \mathrm{Q}\right)\right) \Psi_1(\mathrm{Q}) + \frac{1}{\sqrt{2}} \frac{\mathrm{V}^*}{2J} \Psi_3(\mathrm{Q}),$$

where Ψ_{Neel1} is a Néel state and Ψ_1 and Ψ_3 are excited states. E_0 is the energy of the Néel state. These states are illustrated in Figure 4.4.

The spin correlation function can be written as

$$\begin{aligned} \mathrm{S}^{xx}(\mathrm{Q}, \omega) \approx \left(-\frac{1}{4\pi}\right) \mathrm{Im}[& \left(1 - \epsilon \cos(2\pi \mathrm{Q})\right)^2 G(1,1) \\ - \left(1 - \epsilon \cos(2\pi \mathrm{Q})\right) & \left(\frac{\mathrm{V}*}{2J} G(1,2) + \frac{\mathrm{V}}{2J} G(2,1) + o\left(\epsilon^2\right) \right)], \end{aligned} \tag{4.2}$$

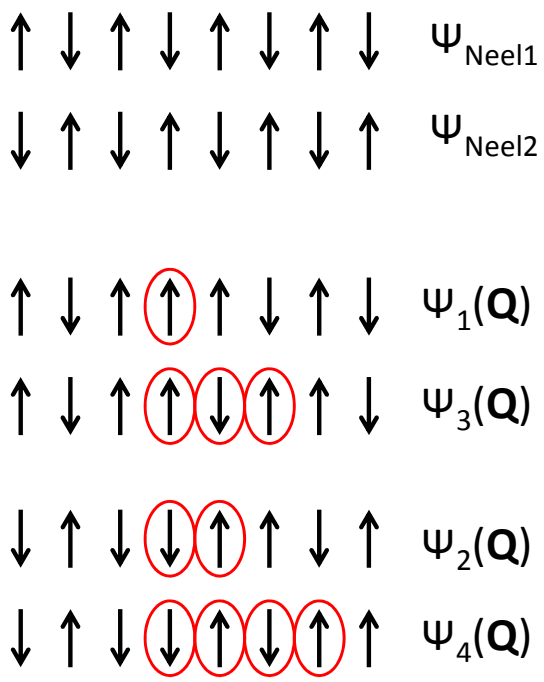

Figure 4.4: **Basis states for the perturbation theory from the pure Ising limit** used by Ishimura and Shiba. The states with flipped spins are excited states of the Néel state. This Figure is inspired by Figure 1 in reference [179].

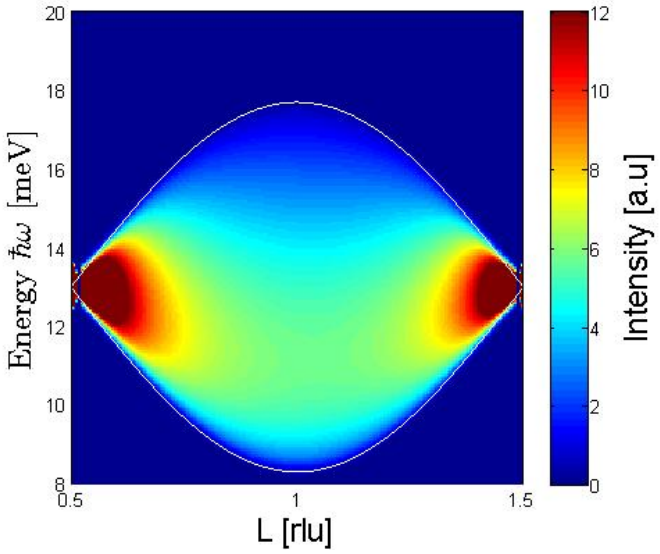

Figure 4.5: **Excitation continuum for the isolated chain model.** The white lines are the upper and lower boundaries of the continuum resulting from solitons in isolated chains. The parameters are estimated for compounds of the $ACoX_3$ family. For the isolated chain model, the parameters are J = 6.5 meV and $\epsilon = 0.18$.

where $G(i,j) = \left\langle i \left| \frac{1}{\omega - H + i\mu} \right| j \right\rangle$, $(\mu \to +0)$, is the Green's function defined using (4.1). The resulting excitation spectrum is shown in Figure 4.5

The interchain coupling model

Shiba [183] extended the isolated chain model by Ishimura and Shiba by taking interchain coupling into account through the staggered field $h_{IC} = nJ_{IC}$, where J_{IC} is the exchange between nearest neighboring chains and n is a multiplicity arising from the magnetic structure. Under the influence of interchain coupling discrete peaks arise. The boundaries of the continuum shift slightly, and the discrete peaks due to interchain interaction have spectral weight also outside of the continuum boundaries. Figure 4.6 shows the excitation spectrum when interchain coupling is taken into account. In Figure 4.7 the excitations for isolated chains and for coupled chains are compared. Under the influence of interchain coupling the continuum splits into discrete peaks, which appear on top of the continuum arising from isolated chains (two staggered fields arise due to the assumed magnetic structure, here h_{IC} = 0 and 6*0.05 meV. The staggered field $h_{IC} = 0$ meV leads to a continuum, while h_{IC} = 6*0.05 meV leads to discrete peaks on top of the continuum).

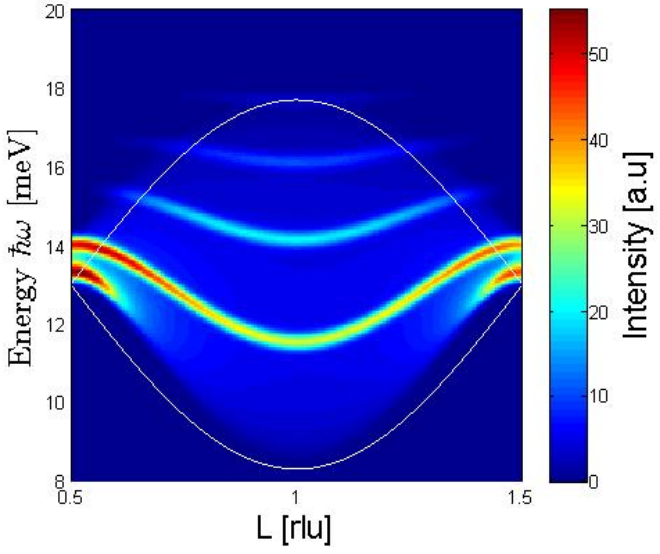

Figure 4.6: **Excitation spectrum of the interchain coupling model.** The white lines are the boundaries for the continuum arising from isolated chains. The parameters are estimated for compounds of the $ACoX_3$ family. For the interchain coupling model the parameters are $J = 6.5$ meV and $\epsilon = 0.18$ with an added interchain interaction $h_{IC} = 0$ and 6*0.05 meV.

Equation (4.1) then takes the form

$$\langle \nu, \mathrm{Q} \left| H \right| \nu, \mathrm{Q} \rangle = \begin{cases} 2J\left(1+\epsilon^2\right) + 2(2\nu - 1)h_{\mathrm{IC}} & \text{for } \nu = 1, \\ 2J\left(1+\frac{3}{2}\epsilon^2\right) + 2(2\nu - 1)h_{\mathrm{IC}} & \text{otherwise,} \end{cases} \tag{4.3}$$

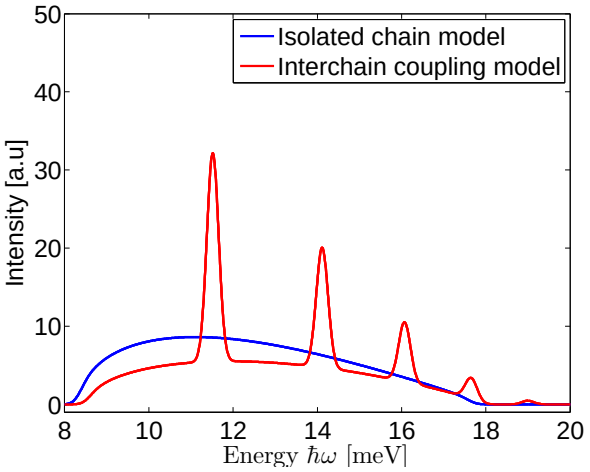

Figure 4.7: **Comparison between the isolated chain model and the interchain coupling model.** The parameters are estimated for compounds of the $ACoX_3$ family and are taken as $J = 6.5$ meV, $\epsilon = 0.18$. Q is 1.0 [r.l.u.]. The staggered fields are $h_{IC} = 0$ and 6*0.05 meV.

and

$$\langle \nu, \mathrm{Q} \,|H|\, \nu', \mathrm{Q} \rangle = \begin{cases} \mathrm{V} & \text{for } \nu' = \nu + 1, \\ \mathrm{V}^* & \text{for } \nu' = \nu - 1, \\ \mathrm{V}_2 & \text{for } \nu' = \nu + 2, \\ \mathrm{V}_2^* & \text{for } \nu' = \nu - 2, \\ 0 & \text{otherwise,} \end{cases} \tag{4.4}$$

where $\mathrm{V}_2 = -J\frac{1}{2}\epsilon^2 \left[1 + e^{-4\pi i \mathrm{Q}}\right]$. The dynamic spin correlation function $\mathrm{S}^{xx}(\mathrm{Q}, \omega)$ is calculated in a similar manner to the isolated chain model, using the matrix elements of equation (4.4) instead of (4.1).

The in-chain next nearest neighbor (nnn) model

Matsubara extended the interchain coupling model by taking a next nearest neighbor in-chain interaction into account [182, 184]. He studied the quasi one-dimensional antiferromagnets $CsCoCl_3$, $CsCoBr_3$ and $RbCoCl_3$ using magnetic Raman scattering [182]. He explained the results by extending the interchain coupling model by Shiba. In addition to the interchain exchange h_{IC} and the antiferromagnetic in-chain nearest neighbor (nn) exchange J, he also takes the ferromagnetic in-chain next nearest neighbor (nnn) exchange J' into account. The effect of J' is shown in Figures 4.8. In this model the intensity of the continuum decreases while the discrete peaks win in intensity. Also the low energy limit of the excitation spectrum is at higher energies than the lower boundary given by the isolated chain model. The boundaries of the continuum for isolated chains are not valid anymore in this model. Figure 4.9 compares the in-chain nnn model with the interchain coupling model. The position of the discrete peaks shifts, and the spectral weight of the continuum arising

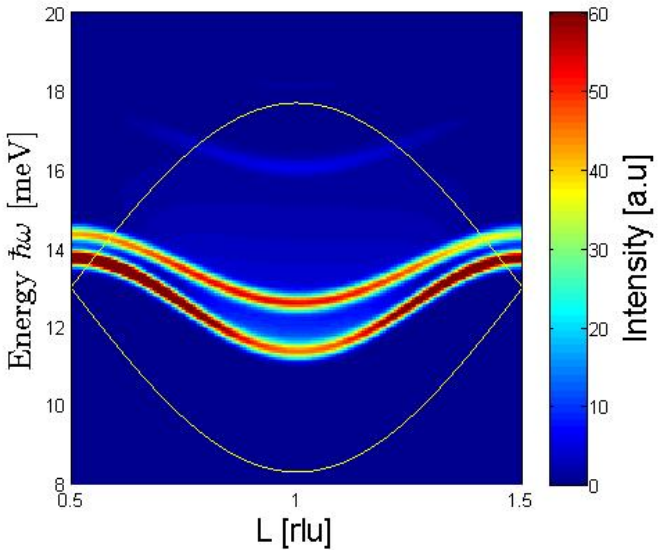

Figure 4.8: **Excitation spectrum of the in-chain next nearest neighbor (nnn) model.** The weight lines are the boundaries of the continuum for isolated chains. The parameters are estimated for compounds of the $ACoX_3$ family. The parameters are J = 5.43 meV, J' = -1.07 meV, ϵ = 0.18 and the staggered fields are h_{IC} = 0 and 6*0.05 meV.

from isolated chains decreases. The part of spectral weight accounted for by the discrete peaks compared to the spectral weight of the continuum is bigger when J' is taken into account. Also the onset of the intensity is now at higher energy, and no continuum is visible at energies lower than the position of the first peak.

The matrix elements of the Hamiltonian are given by

$$\langle \nu, \mathrm{Q} \,|H|\, \nu, \mathrm{Q} \rangle = \begin{cases} 2J\left(1+\epsilon^2\right) + 2J'\left[1-\epsilon\cos(2\pi \mathrm{Q})\right] + 2(2\nu-1)h_{\mathrm{IC}} & \text{for } \nu = 1, N-1, \\ 2J\left(1+\frac{3}{2}\epsilon^2\right) + 4J' + 2(2\nu-1)h_{\mathrm{IC}} & \text{otherwise,} \end{cases} \tag{4.5}$$

for diagonal terms, and for off-diagonal terms by

$$\langle \nu, \mathrm{Q} \,|H|\, \nu', \mathrm{Q} \rangle = \begin{cases} \mathrm{V}_2 * & \text{for } \nu' = \nu - 4, \\ \mathrm{V} * & \text{for } \nu' = \nu - 2, \\ \mathrm{V} & \text{for } \nu' = \nu + 2, \\ \mathrm{V}_2 & \text{for } \nu' = \nu + 4, \\ 0 & \text{otherwise.} \end{cases} \tag{4.6}$$

The dynamic spin correlation function $\mathrm{S}^{xx}(\mathbf{Q}, \omega)$ is calculated using equations (4.2), (4.5) and (4.6). For $RbCoCl_3$ Matsubara found the parameters ϵ = 0.15, J = 71.8 K $\approx$ 6.19 meV, J'/J = 0.135 and J_{IC}/J = 0.02. Fits by Matsubara to the Raman scattering results for $RbCoCl_3$ work well for low frequencies, but additional peaks which were not observed by Matsubara are predicted by this model [182].

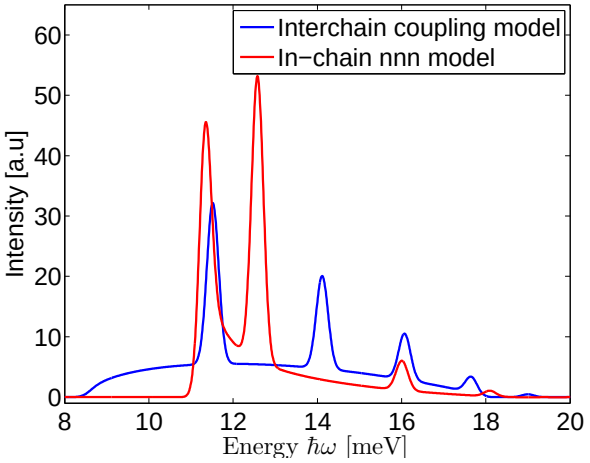

Figure 4.9: **Comparison between the interchain coupling model and the in-chain next nearest neighbor (nnn) model.** The parameters are estimated for compounds of the $ACoX_3$ family and are taken as $J = 6.5$ meV for the interchain coupling model, and $J = 5.43$ meV and $J' =$ -1.07 meV for the in-chain nnn model, and $\epsilon = 0.18$ and $h_{IC} = 0$ and 6*0.05 for both models. Q = 1.0 [r.l.u.].

The exchange mixing model model

Goff *et al.* [60] describe the magnetic excitations observed by neutron scattering in the Ising antiferromagnetic chain $CsCoCl_3$ using the spin Hamiltonian with diagonal terms

$$\langle \nu, \mathrm{Q} \,|H|\, \nu, \mathrm{Q} \rangle = \begin{cases} 2J + \nu h_{\mathrm{IC}} & \text{for } \nu = 1, N-1, \\ 2J + \nu h_{\mathrm{IC}} + 2\Delta & \text{otherwise,} \end{cases} \tag{4.7}$$

and off-diagonal terms

$$\langle \nu, \mathrm{Q} \,|H|\, \nu', \mathrm{Q} \rangle = \begin{cases} \mathrm{V}^* & \text{for } \nu' = \nu - 2, \\ \mathrm{V} & \text{for } \nu' = \nu + 2, \\ 0 & \text{otherwise,} \end{cases} \tag{4.8}$$

where ν runs over the values 1,3,5,...,N-1.

Δ is the exchange mixing, and calculated to be $\Delta = 0.09$J. The exchange mixing arises from a mixing with higher levels having the same spin number. This depresses the split levels of the lowest Kramers doublet by the same amount Δ. The exchange mixing term helps to distinguish energetically between a two-soliton and a spin-wave state. This function can also be fulfilled by the in-chain next nearest neighbor interaction J' introduced in Matsubara's in-chain nnn model. The difference is that J' leads to an additional Q-dependence of the matrix elements of the Hamiltonian, while Δ is a local splitting. The dynamic spin correlation function $\mathrm{S}^{xx}(\mathrm{Q}, \omega)$ is calculated using equations (4.2), (4.7) and (4.8).

Goff found "*quantitative agreement*"between his model and neutron scattering

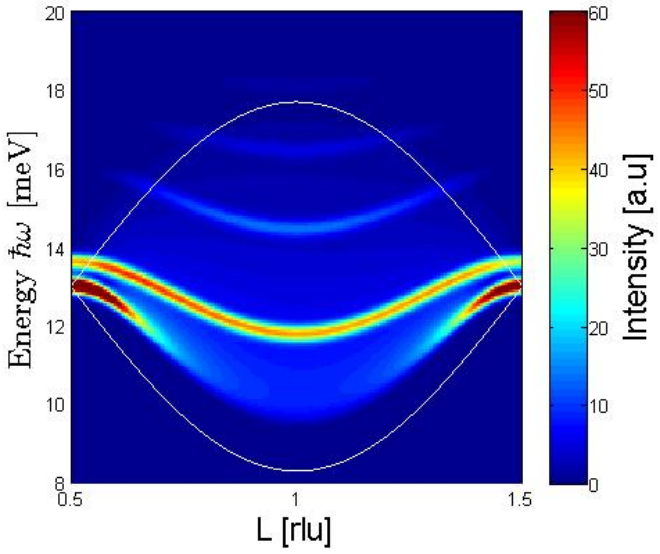

Figure 4.10: **Excitation spectrum for the exchange mixing model.** The white curves are the lower and upper boundaries of the continuum arising from isolated chains. The parameters are estimated for compounds of the $ACoX_3$ family and are $J = 6.5$ meV, $\epsilon = 0.18$ with an interchain interaction $h_{IC} = 0$ and 6*0.1 meV and exchange mixing $\Delta = 0.09{*}J = 0.59$ meV.

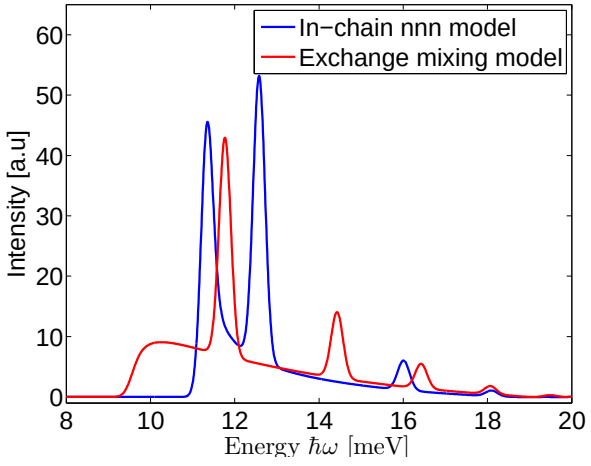

Figure 4.11: **Comparison between the in-chain nnn model and the exchange mixing model.** The parameters are estimated for compounds of the $ACoX_3$ family and are taken as $J = 5.43$ meV, $J' =$ -1.07 meV, $\epsilon = 0.18$ and $h_{IC} = 0$ and 6*0.05 for the in-chain nnn model, and $J = 6.5$ meV, $\epsilon = 0.18$, $h_{IC} = 0$ and 6*0.1 meV and $\Delta = 0.59$ meV for the exchange mixing model.

data for $CsCoCl_3$, and his model works better in this case than Matsubara's in-chain nnn model [60].

Figure 4.10 shows the excitation spectrum for the exchange mixing model. The lower boundary for isolated chains is too low compared to this model, and the upper boundary does not fit also. Again the discrete peaks have spectral weight outside of the continuum. Figure 4.11 shows the difference between Matsubara's in-chain nnn model and Goff's exchange mixing model. The differences are remarkable. The peak positions change, and the continuum from isolated chains is smaller in the in-chain nnn model than in the exchange mixing model. The first peak in the exchange mixing model is a broad onset of the continuum.

4.3 Magnetic and crystallographic structure of $RbCoCl_3$

In order to understand the magnetic excitations in $RbCoCl_3$ a good understanding of the crystallographic and magnetic structure is essential. To obtain this, neutron scattering experiments were performed in cooperation with Nora Hänni from the University of Bern. The results presented in this section are also published in reference [185].

4.3.1 Experiments

Experiments were performed on powder and on single crystal samples. The samples used for this work were grown by Nora Hänni at the University of Bern under the supervision of Karl Krämer [185], three single crystals are shown in Figure 4.12. Neutron diffraction data on powder samples were obtained by Nora Hänni and Karl Krämer at the HRPT [186, 187] and DMC [187] powder diffractometers at the Swiss spallation neutron source (SINQ) at the Paul Scherrer Institut (PSI) in Villigen, Switzerland. The data were collected between 1.5 K and 300 K.

Data from elastic neutron scattering were obtained on the triple-axis spectrometers IN22 at ILL and EIGER at PSI at temperatures between 1.5 K and 80 K. An elastic neutron scattering experiment on EIGER with vertical magnetic fields between 0 T and 13 T was also performed. The samples were aligned for the experiments with scattering plane (0 0 1) and (1 1 0) for the experiment on IN22 and (0 0 2) and (2 2 0) for the experiments on EIGER.

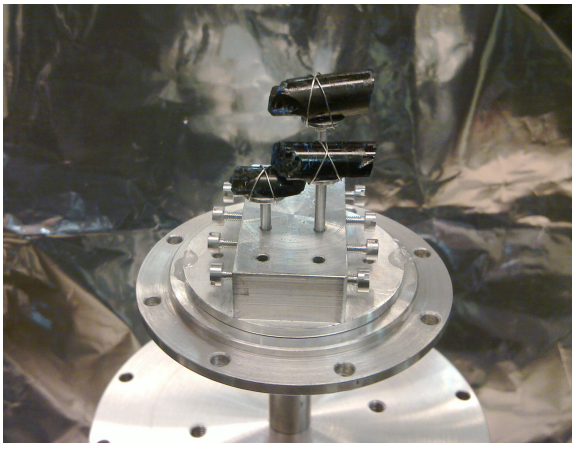

Figure 4.12: **Three $RbCoCl_3$ single crystals** grown by Nora Hänni [185]. The depicted crystals were used for inelastic neutron scattering measurements at the time-of-flight spectrometer LET of the ISIS Facility at the Rutherford Appleton Laboratory in Didcot, UK, see section 4.4.1, and are already mounted onto the sample holder. The samples were handled in a glove box filled with helium and put in an aluminum sample can.

4.3.2 Crystal Structure

$RbCoCl_3$ is a hexagonal perovskite of the family $ACoX_3$ with A = Rb, Cs, Tl and X = Br, Cl. The Rb^+ and Cl^- ions form layers of $RbCl_3$ along the c-axis, and smaller Co^{2+} ions occupy octahedral voids between the layers. The Co^{2+} ions carry an effective spin-$\frac{1}{2}$, see section 4.1.1, and form chains along the c-axis. On cooling down to 1.5 K no indications for a structural phase transition were observed [185]. Table 4.1 gives the lattice parameters for different temperatures. The crystal structure obtained is shown in Figure 4.13.

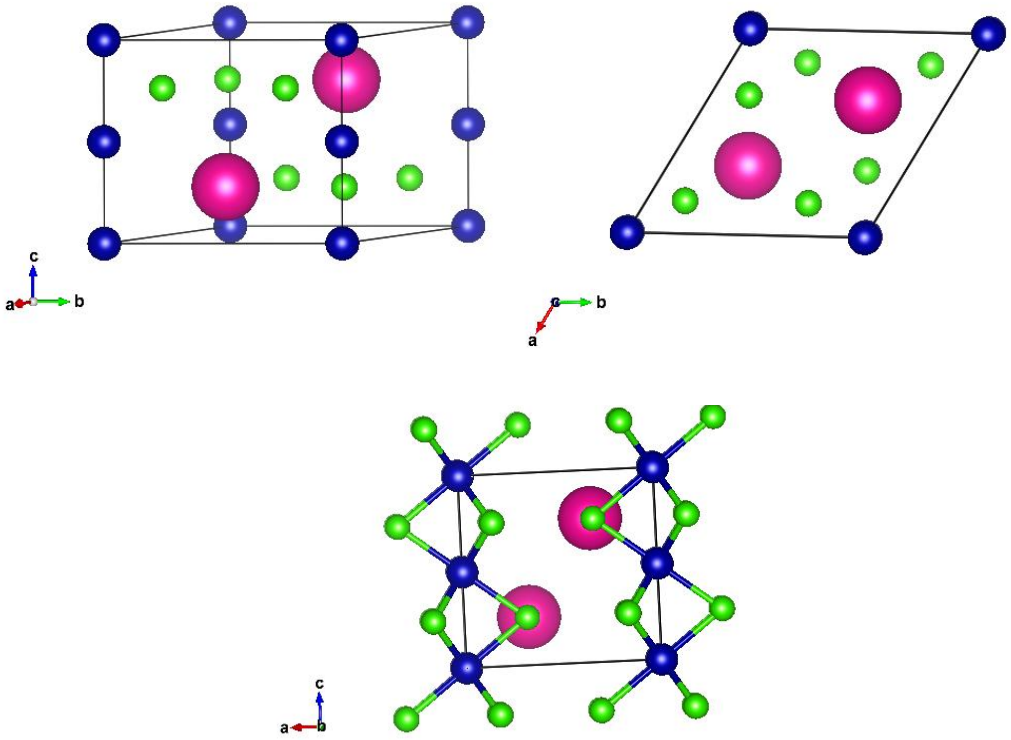

Figure 4.13: **Crystal structure of $RbCoCl_3$.** Rb is purple, Co blue and Cl green. The Co^{2+} ions carry spin-$\frac{1}{2}$ and form chains along the crystallographic c-axis [185, 188]. These plots were made with VESTA [139].

T [K]	a [Å]	c [Å]
297	7.0003(3)	5.9989(2)
80	6.9416(2)	5.9606(2)
1.5	6.9299(1)	5.9510(1)

Table 4.1: Lattice parameters for $RbCoCl_3$ at different temperatures [185].

4.3.3 Magnetic structure

In diffraction experiments with powder and single crystal samples two magnetic phase transitions were observed at $T_{N_1} \approx 28$ K and $T_{N_2} \approx 14$ K [185] (for comparison: the transition temperatures for $CsCoCl_3$ are $T_{N_1} \approx 21$ K and $T_{N_2} \approx$ 10-14 K [60, 189]). Diffraction scans obtained on EIGER are shown in Figure 4.14 and the integrated intensity of these peaks is shown in Figure 4.15. In order to obtain the integrated intensities, the Bragg contributions observed in the diffraction experiments were fitted using a Gaussian, while the diffuse contributions were fitted using a Lorentzian. At the transition temperatures one can observe an increase in the Bragg contribution (related to magnetic long range order) and a simultaneous decrease of diffuse scattering (indicating short range order).

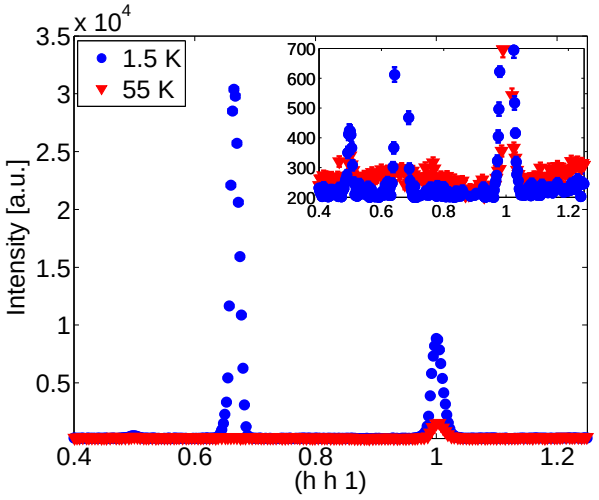

Figure 4.14: **Diffraction pattern of a $RbCoCl_3$ single crystal** at 1.5 K and 55 K. A structural peak at h = 1 is prohibited by the space group of $RbCoCl_3$, but the peak at h = 1 at 55 K is not of magnetic origin [185].

Figure 4.16 shows a temperature diagram for $RbCoCl_3$ indicating the transition temperatures, and the temperatures where the magnetic structure was determined.

The magnetic moments point along the crystallographic c-direction, which is also the chain direction. The magnetic exchange interactions along the chains are antiferromagnetic and rather strong because of superexchange via the Co-Cl-Co bonds. The shortest interaction path between the chains is via Co-Cl-Cl-Co. This includes a Cl-Cl van der Waals contact, and therefore the magnetic interchain interaction is much weaker than the interaction within a chain [185, 190].

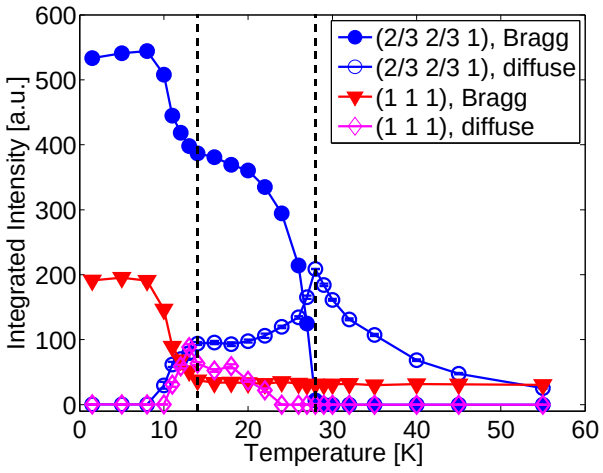

Figure 4.15: **Integrated intensity of diffraction scans on $RbCoCl_3$** made on the thermal neutron triple-axis spectrometer EIGER at PSI. The transition temperatures are indicated by the dotted lines. At the transition temperature the Bragg scattering increases while the diffuse scattering increases at $T_{N_{1,2}}$, but decreases with further decreasing temperatures.

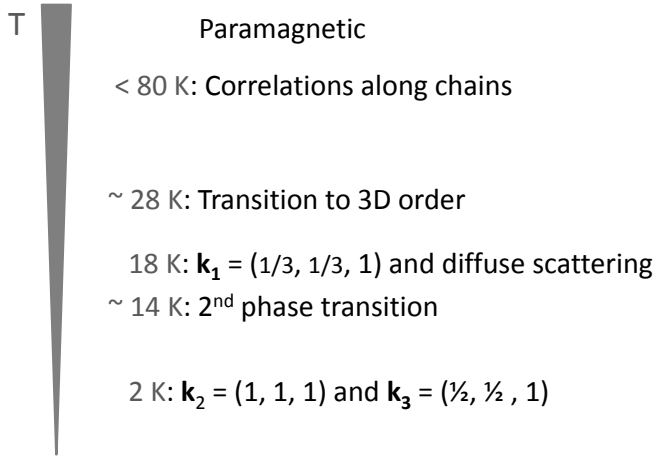

Figure 4.16: **Temperature dependence of the magnetic correlations in $RbCoCl_3$.** This Figure sketches how the magnetic structure of $RbCoCl_3$ changes with temperature, and where the magnetic structure was determined for each phase.

Structure for $T > T_{N_1}$

The magnetic moments order antiferromagnetically in the chains below 70 - 80 K where the magnetic susceptiblity shows a maximum [185]. Above T_{N_1} the interchain interaction plays no role in the correlation between spins. The magnetic moments are parallel to the crystallographic c-axis, but are unordered in the ab-plane.

Structure for $T_{N_1} > T > T_{N_2}$ (intermediate temperatures)

At $T_{N_1} > T > T_{N_2}$ one propagation vector, $\mathbf{k}_1 = \left(\frac{1}{3}, \frac{1}{3}, 1\right)$, was observed. The magnetic structure determined by N. Hänni [185] at T = 18 K, which is between T_{N_2} and T_{N_1}, is shown in Figure 4.17 (a). In neutron scattering experiments phases are undetermined, and solutions which differ only in a phase shift have to be considered equivalent. Therefore, the magnetic structures of $RbCoCl_3$ and $CsCoCl_3$, shown in Figure 4.17, are considered equivalent at intermediate temperatures [185, 189].

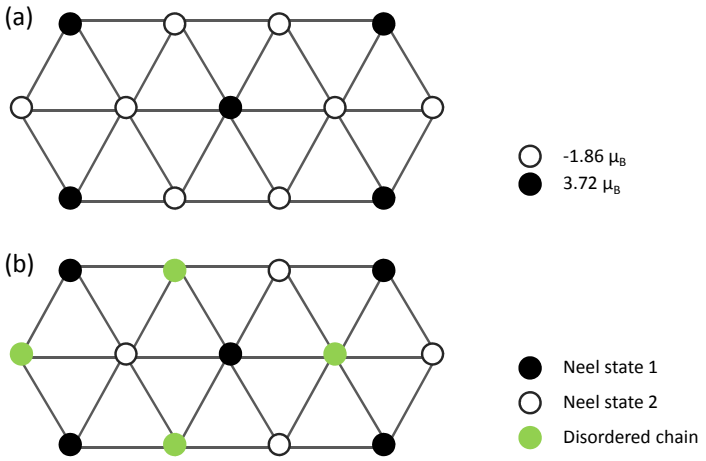

Figure 4.17: **Magnetic structure in the intermediate temperature phase.** (a) Magnetic structure of $RbCoCl_3$ at 18 K determined by Nora Hänni [185]. (b) Magnetic structure found for the intermediate temperature phase in $CsCoCl_3$ by Mekata [189]. This structure is equivalent to the structure shown in (a) because in neutron scattering phases are undetermined.

Monte Carlo Simulation of the magnetic structure

In order to understand the magnetic structures better, Monte Carlo simulations were done in cooperation with Mattia Mena from University College London [191]. Ab-initio calculations were performed where the energy of a system of random spins with magnetic moment $\pm\mu_B$ aligned along the crystallographic c-axis, which are subject to an antiferromagnetic nearest neighbor and ferromagnetic next nearest neighbor interaction, was minimized. The diffraction pattern for the resulting structures was calculated and compared with the experimentally obtained diffraction pattern.

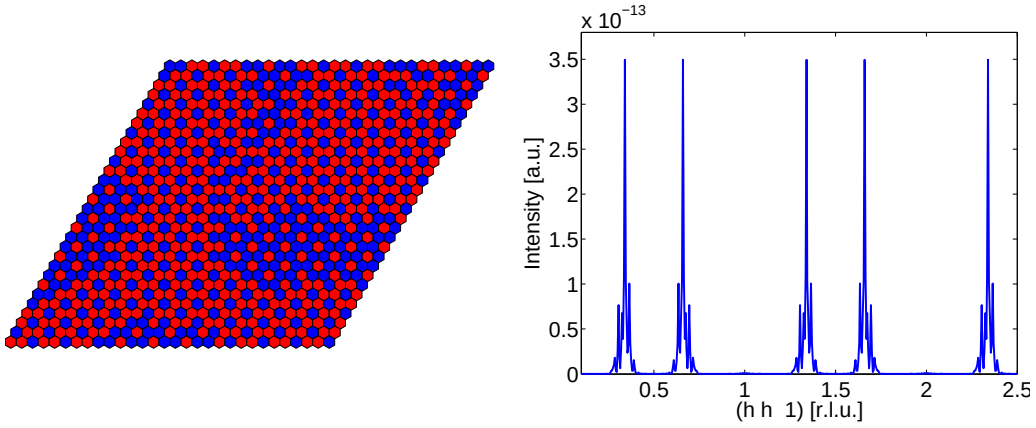

Figure 4.18: **Monte Carlo simulation of the magnetic structure and Bragg diffraction pattern at intermediate temperatures** done in cooperation with Mattia Mena from University College London [191]. The partially ordered magnetic structure in the ab-plane which leads to the Bragg diffraction pattern which agrees with the experimentally observed Bragg pattern at 18 K. Therefore the structure at 18 K is thought to be similar to the one shown here.

The Monte Carlo simulation reproduces the positions of the Bragg peaks which give the propagation vector. The magnetic moment is connected to the intensity of the Bragg peaks. For intermediate temperatures, the Monte Carlo simulation is able to reproduce the position of the sharp Bragg peaks at h = 1/3 arising from the propagation vector $\mathbf{k}_1 = \left(\frac{1}{3}, \frac{1}{3}, 1\right)$ and the diffuse scattering observed at 18 K. These features can be obtained from a partially disordered magnetic structure, as shown in Figure 4.18. The order within the domains leads to the sharp Bragg peaks at h = 1/3 while the disorder at the boundaries of the domains leads to diffuse scattering. Better simulations may be obtained using the *cluster heat bath method* [192, 193] used by Koseki and Matsubara to simulate the magnetic phase transitions in $CsCoCl_3$ and $CsCoBr_3$ [194].

Structure for $T_{N_2} > T$ (low temperatures)

Below T_{N_2} two additional propagation vectors, $\mathbf{k}_2 = (1, 1, 1)$ and $\mathbf{k}_3 = \left(\frac{1}{2}, \frac{1}{2}, 1\right)$, have been found. The peak arising from $\mathbf{k}_3$ is small. Elastic neutron scattering scans with and without an applied magnetic field and X-ray diffraction confirm that the $\mathbf{k}_3$ propagation vector is of magnetic origin. The magnetic structure at 2 K is of a ferrimagnetic kind and is sketched in Figure 4.19.

Monte Carlo Simulation of the magnetic structure

Minimizing the energy on a random grid as done for intermediate temperatures leads to a perfect honeycomb lattice, the structure in the top diagram in Figure 4.19 where $\mathbf{k}_3$ is not taken into account. This ideal honeycomb ground state at 2 K, and the corresponding magnetic Bragg pattern, are shown in Figure 4.20. In addition to a nearest neighbor antiferromagnetic inter-chain exchange, a ferromagnetic next-nearest neighbor interaction is also needed to stabilize the perfect honeycomb structure [161, 183].

At low temperatures the Monte Carlo simulation should reproduce two effects: The propagation vectors $\mathbf{k}_2 = (1, 1, 1)$ and $\mathbf{k}_3 = \left(\frac{1}{2}, \frac{1}{2}, 1\right)$. While the peak arising at h = 1 could be reproduced , the peak arising at h = 1/2, which was observed experimentally, could not be reproduced using Monte Carlo simulations. Additional simulations which take not only single planes, but the three dimensional nature of the problem into account were also done. Defects in the planes and along the chains were introduced in the simulations, but have, so far, not reproduced the peak at h = 1/2. A possible explanation could be that the implementation of the temperature is not yet satisfying. Only the position of the Bragg peaks, which give the propagation vectors, could be reproduced, but not the correct intensities. The relative intensities are connected to the relative magnetic moments.

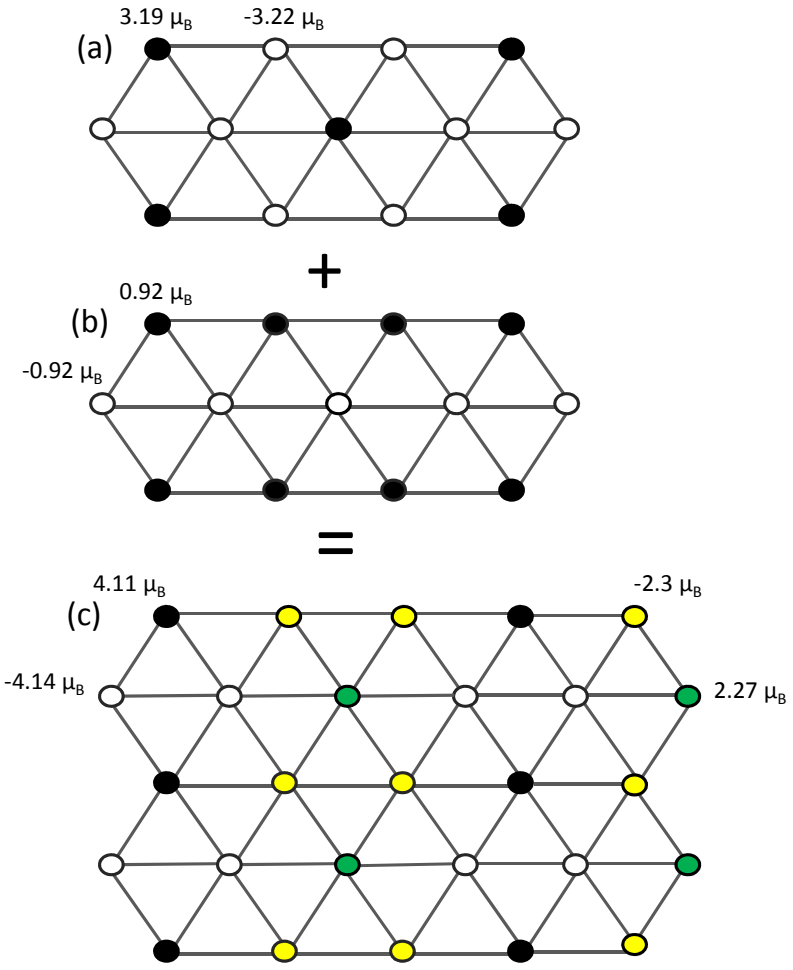

Figure 4.19: **Magnetic structure in the low temperature phase.** Magnetic structure of $RbCoCl_3$ at 2 K considering the propagation vectors $\mathbf{k}_1$, $\mathbf{k}_2$ and $\mathbf{k}_3$. (a) The top structure arises when only $\mathbf{k}_1$ and $\mathbf{k}_2$ are taken into account, the middle structure (b) is the structure arising from $\mathbf{k}_3$, and the lower structure (c) is the sum of top and middle structure, arising from all three propagation vectors. The top structure is the same as found for $RbCoCl_3$ by Lockwood [190] and for $CsCoCl_3$ by Mekata [189].

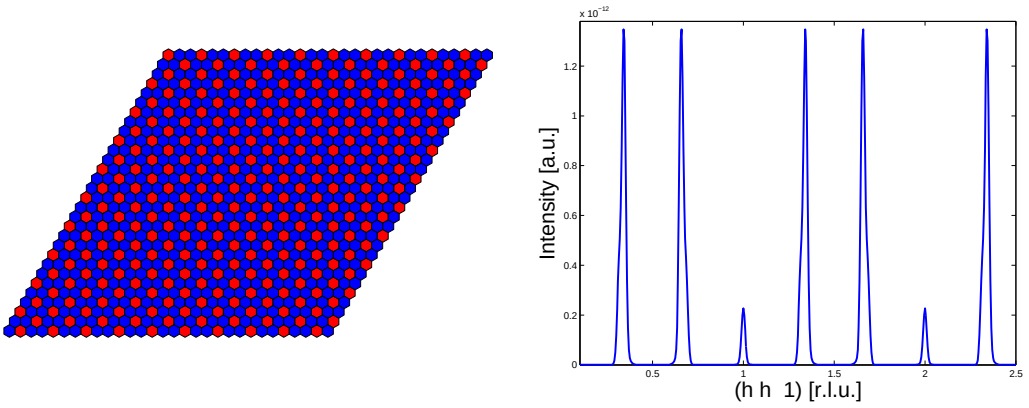

Figure 4.20: **Monte Carlo simulation of the magnetic structure and Bragg pattern at low temperatures** done in cooperation with Mattia Mena from University College London [191]. The magnetic structure in the ab-plane found with Monte Carlo simulations minimizing the energy at 2 K corresponds to the structure in the top diagram in Figure 4.19. This structure leads to the magnetic Bragg diffraction pattern shown here.

4.3.4 Discussion

Neutron diffraction on powder samples and elastic neutron scattering on single crystals confirm the crystallographic structure from Engberg and Soling [188]. No structural phase transitions were observed. Two magnetic order transitions were observed and the transition temperatures agree with those found using Raman scattering by Lockwood [190] and using FIR spectroscopy by Jörke [180].

The magnetic structure for $T_{N_1} \geq T \geq T_{N_2}$ is the same as found for $CsCoCl_3$ except for a phase shift. Lockwood found the magnetic structure at temperatures lower than T_{N2} to be the same as for $CsCoCl_3$ [190], while we observed an additional propagation vector $\mathbf{k}_3 = \left(\frac{1}{2}, \frac{1}{2}, 1\right)$. Jörke and Dürr [180] observed a "*not pure F-phase*" (the phase for $T < T_{N_2}$). They attributed this to impurities in the crystal and domain wall pinning. Monte Carlo simulations using spins with a fixed magnetic moment pointing along a given axis, done in cooperation with Mattia Mena from University College London [191], have been able to reproduce the position of the Bragg peaks at 18 K, but at low temperatures only the perfect honeycomb structure, without a contribution from $\mathbf{k}_3$, could be reproduced. Koseki and Matsubara [194] did Monte Carlo simulations of the magnetic ordering of $CsCoCl_3$ and $CsCoBr_3$ using a method called the "*cluster heat bath method*"[192, 193]. Monte Carlo simulations using this method still need to be implemented for $RbCoCl_3$, but could lead to a better insight into the magnetic ordering of $RbCoCl_3$. Also the relative intensity of

the Bragg peaks was not reproduced by the Monte Carlo simulations. This would lead to the relative magnetic moments. A good understanding of the magnetic order in the different phases is needed to understand the excitation spectrum of $RbCoCl_3$ in these phases. The excitation spectrum of Ising chains depends on the staggered field as seen in section 4.2.1. The staggered field is given by $h_{\mathrm{IC}} = n \times J_{\mathrm{IC}}$ where J_{IC} is the interchain interaction and n is a multiple arising from the magnetic structure. Nonetheless, the contribution from $\mathbf{k}_3$ is small, and may therefore be neglected in a first approximation to understand the magnetic excitations.

The diffuse scattering is remarkably strong at some temperatures, and studying it, as e.g. done by P. Manuel *et al.* for $YBaCo_4O_7$ [195], could teach us more about the magnetic order in $RbCoCl_3$, especially close to the phase transitions.

4.4 Excitations in $RbCoCl_3$

4.4.1 Experiments

In addition to the diffraction experiments described in section 4.3.1, mostly inelastic neutron scattering experiments were performed on $RbCoCl_3$. The samples used in these experiments were single crystals grown by Nora Hänni, see section 4.3.1, Figure 4.12, and [185]. For the time-of-flight experiment three single crystals were coaligned, while for the triple-axis-experiments only one crystal was aligned. Alignment was done on the two-axis neutron diffractometer Morpheus and the two-axis diffractometer Orion at PSI. The samples were sealed in an aluminum can filled with helium.

A high-resolution neutron scattering experiment was performed on the cold neutron multi-chopper time-of-flight spectrometer LET at ISIS [196]. High statistics scans were made at 4 K $< T_{N_2} <$ 18 K $< T_{N_1} <$ 35 K with an incoming energy of 25 meV, while lower statistics scans were collected at 8 K $< T_{N_2} <$ 10.5 K and 23 K $< T_{N_1}$ with an incoming energy of 20 meV . The time-of-flight data were prepared for data analysis by Mattia Mena [191].

A neutron scattering experiment was performed on the thermal neutron triple-axis-spectrometer IN22 at ILL. The main objective of this experiment was to study certain Q-points, which were identified in the time-of-flight experiment, over a wider temperature range. Several diffraction scans were also obtained. Using an orange cryostat, scans at temperatures between 2 K and 80 K were made in the energy range 8 - 20 meV. The scattering plane was given by (1 1 0) and (0 0 1). k_f was fixed to 1.97 $Å^{-1}$ for inelastic, and to 2.662 $Å^{-1}$ for elastic measurements. The instrument setting was source – monochromator – monitor 1 – slits – orange cryostat with sample – slits – PG filter – monitor 2 – analyzer – detector. The best resolution on IN22 is obtained at (2/3 2/3 1.2), therefore scans were made at this Q-point between 2 K and 80 K.

An experiment was performed on the thermal neutron triple-axis spectrometer EIGER at PSI. EIGER is a new instrument, and a high resolution mode which uses $\lambda/2$ on the monochromator was used for this experiment. The sample was the same one as used for the experiment on IN22. Temperatures were again between 1.5 K and 80 K, and the scattering plane was given by (0 0 2) and (2 2 0). The energy range was 8 - 20 meV. Diffraction scans were made. In this experiment complementary Q-points not studied on IN22 were measured, and especially the evolution of the excitation spectrum at elevated temperature was studied. For the inelastic scans k_f was fixed to 2.662 $Å^{-1}$. The instrument setting was source – monochromator PG – monitor 1 – slits – orange cryostat with sample – slits – monitor 2 – analyzer PG – detector.

From the triple-axis data the background as a function of A4 was subtracted, and a spurion was removed from the IN22 spectrum. The IN22 and EIGER data were

normalized for their average counting times (60 seconds for IN22 and 380 seconds for EIGER). The triple-axis data from IN22 were convoluted with the 4D resolution function using Trixfit [92, 93], see section 2.5.1.

4.4.2 Results

Measurements were done with L ranging from 1.0 to 1.5 [r.l.u.] at temperatures between 2 and 80 K.

Figure 4.21 shows color plots of scans at (2/3 2/3 L) with L = 1.0 - 1.5 [r.l.u.] at 2, 18, 35 and 60 K. Figure 4.22 shows scans at (2/3 2/3 1.2) made at 2 K, 18 K and 35 K. Each of these temperatures is in a different magnetic phase. The evolution of the excitations with temperature is shown in the color map in Figure 4.23. This color map illustrates the increasing intensity of the sharp mode with decreasing temperature.

Figure 4.24 shows the temperature dependence of the integrated intensity. The intensity is integrated at (2/3 2/3 1.2) over an energy range from 10 meV to 18 meV for temperatures up to 80 K to determine the integrated intensity. Figure 4.24 shows that the peak intensity decreases with increasing temperature. This can be explained by a two level system, where the ground state depopulates with increasing temperature and the excited state is populated. At low temperatures it is more likely for a neutron to create a soliton-pair state, because the excited states are not yet occupied. With increasing temperature the probability that excited states are occupied increases, and instead of creating a soliton-pair state a neutron becomes more and more likely to interact with a thermally excited soliton (Villain mode). The decrease in intensity can be fitted with an exponential function of the form $\mathrm{BG} - \mathrm{A}\exp\left(\frac{-\mathrm{E}}{\mathrm{k}_B\mathrm{T}}\right)$ with A = 458(17) [a.u.], E = 6.05(61) meV and BG = 476(4) [a.u.], where A and BG are given in the same "*arbitrary units* "as the intensity. The exponent E is of the magnitude of the energy scale $2J$ and 2E is approximately the size of the gap. In Figure 4.22 a continuum which does not change with temperature is visible above the main mode.

The three energy scans in Figure 4.22 back the observation from the color map in Figure 4.23 that at the first phase transition at $\mathrm{T}_{\mathrm{N}_1}$ the peak position changes, while at the second phase transition at $\mathrm{T}_{\mathrm{N}_2}$ the modes split. At 2 K two peaks are visible, and the splitting decreases when L approaches 1.5 [r.l.u.], see Figure 4.21 (a). The two peaks merge into a broader one at 18 K. The minimum of the mode is at L = 1.0 and around 12 meV for all temperatures, except for 1.5 and 2 K, where the splitting of the modes shifts the minimum of the lower mode down to 11 meV.

To determine peak positions, a Gaussian was fitted to the data. To extract reliable information about the width, one has to account for the possibility that multiple peaks may appear as a single peak due to limitations in resolution. Therefore, determining the width requires a physical model of the excitations.

Figure 4.25 (a) shows how the peak position at (2/3 2/3 1.2) changes with temper-

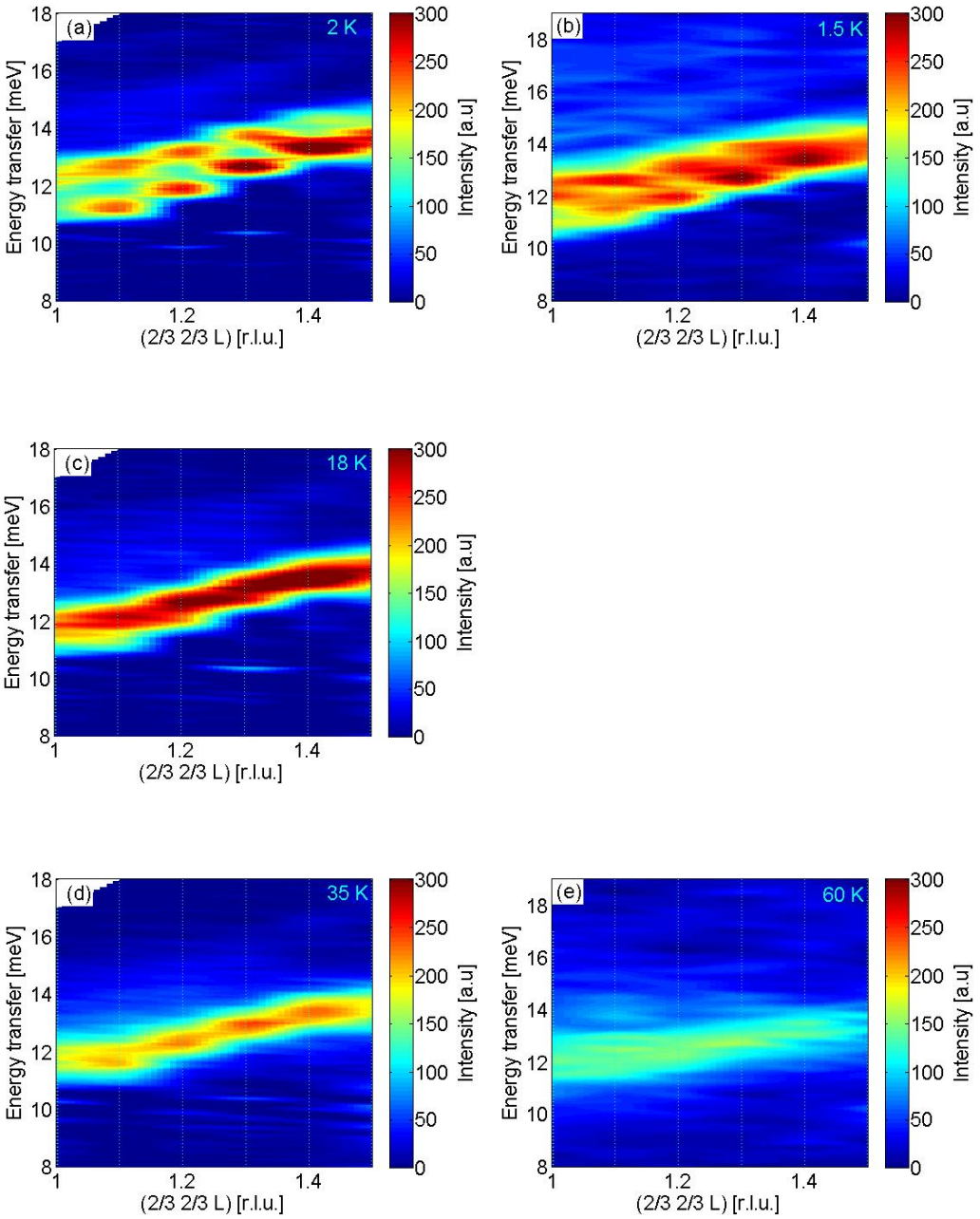

Figure 4.21: **Excitations in $RbCoCl_3$.** Color plots of full data sets for scans at (2/3 2/3 L) with L = 1.0 - 1.5 [r.l.u.] measured at (a) 2K, (b) 1.5 K, (c) 18 K, (d) 35 K and (e) 60 K. Panels (b) and (e) have been measured on EIGER and panels (a), (c) and (d) on IN22. The "blobs "at 2 K are an artifact from data interpolation for the color plot.

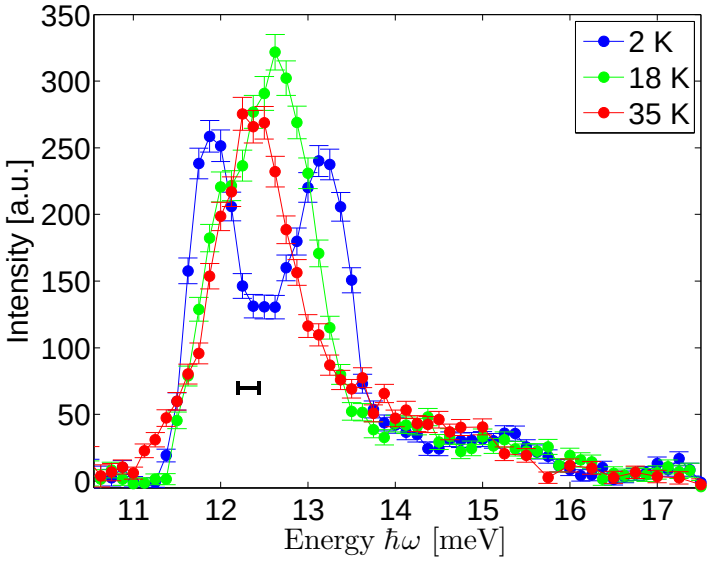

Figure 4.22: **Excitations in the three different phases** Energy scans made at (2/3 2/3 1.2) for three different temperatures. The black line indicates the resolution at 2 K.

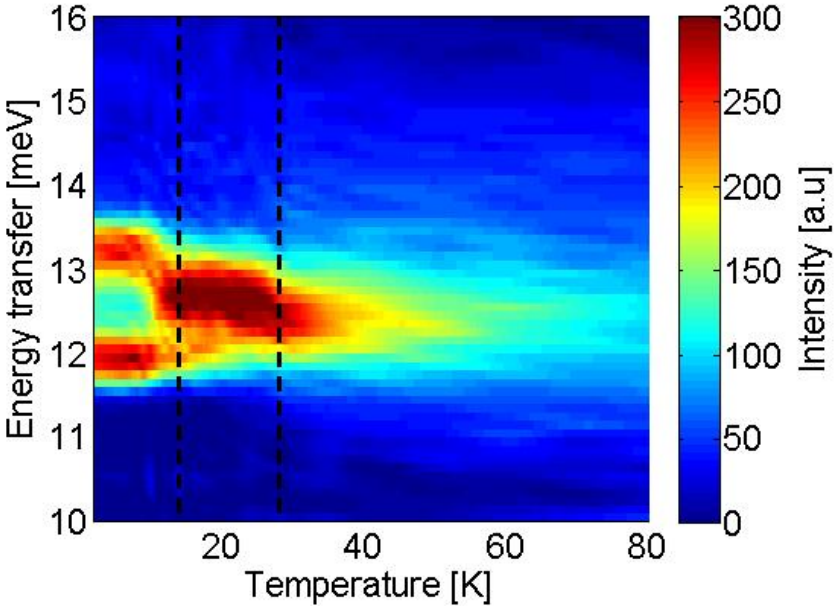

Figure 4.23: **Evolution of peak splitting** at L = 1.2 for temperatures between 2 K and 80 K measured on IN22. The dotted lines indicate 14 K and 28 K, the two transition temperatures.

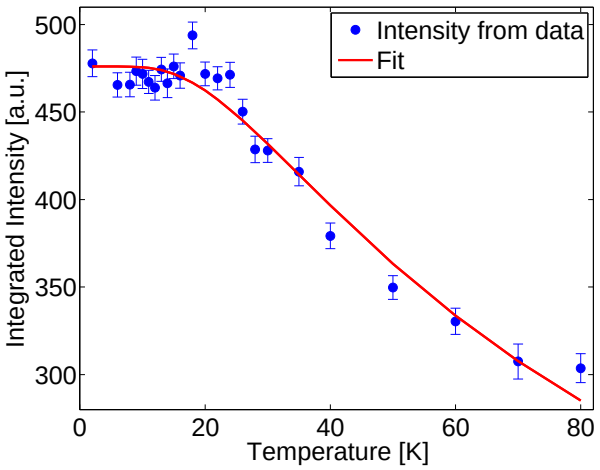

Figure 4.24: **Temperature dependence of the integrated intensity.** The integrated intensity is fitted with an exponential function of the form $BG - A \exp\left(\frac{-E}{k_B T}\right)$ with A = 458(17) [a.u.], E = 6.05(61) meV and BG = 476(4) [a.u.]. The dotted lines indicate the magnetic order transition temperatures.

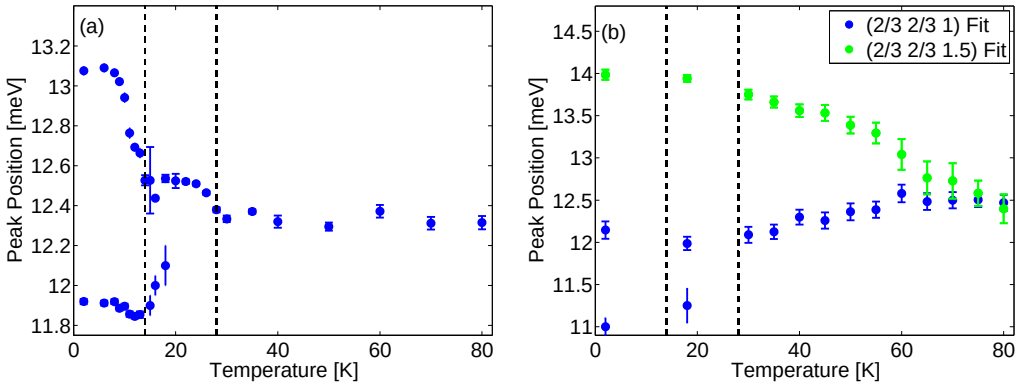

Figure 4.25: **Temperature dependence of the peak position.** (a) The position of maximum intensity at (2/3 2/3 1.2) for different temperatures. This illustrates how the split peaks merge with increasing temperature. (b) The positions of the maximum intensity at (2/3 2/3 1.0) and (2/3 2/3 1.5). The peak position changes with temperature. The peak positions at L = 1.0 and L = 1.5 move closer together, which means that the bandwidth of the dispersion decreases. The dotted lines indicate the magnetic order transition temperatures.

ature. The choice of this **Q**-value is favorable for studies limited by energy resolution because of resolution focusing. The peak positions were fitted with two Gaussians. The evolution and vanishing of the splitting is also shown in the color plot in Figure 4.23. The dotted lines indicate the approximate temperatures of the phase transitions, $T_{N_1} \approx 28$ K and $T_{N_2} \approx 14$ K. The color plot in Figure 4.23 shows how the peak intensity decreases with increasing temperature. The splitting which is resolved clearly at low temperatures vanishes around T_{N_2}. A clear shift of the peak position to lower energies is visible at T_{N_1}.

Figure 4.25 (b) shows how the bandwidth narrows with increasing temperature. This can also be seen in the color plots in Figure 4.21. Because the bandwidth increases with decreasing temperature, the maximum energy of the excitation is at lower energies for high temperatures. A dispersion with a big bandwidth, as seen at low temperature, signifies high mobility, while the narrower dispersion at high temperatures signifies low mobility. The decrease of mobility with increasing temperature is because there are more quasiparticles and thermally populated states at higher temperatures, so less free states are available. This was also observed in an interacting dimer spin system [197].

The results in the different phases are now presented in more detail.

$\mathbf{T > T_{N_1}}$

Data from inelastic neutron scattering were taken up to 80 K. However, the highest temperature where a complete set of inelastic data with (2/3 2/3 L) and L = 1.0 - 1.5 [r.l.u.] was obtained was 60 K. The second highest temperature where a complete data set was obtained is 35 K, color plots for these temperatures are shown in Figure 4.21.

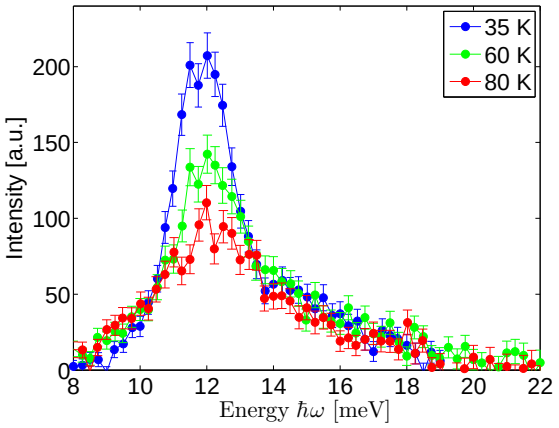

Figure 4.26: **Temperature evolution above $\mathbf{T_{N_1}}$.** Energy scans at (2/3 2/3 1.0) for three different temperatures above T_{N_1}. The sharp peak on top of the broad continuum decreases with increasing temperature, while the intensity of the continuum hardly changes.

Figure 4.26 shows three characteristic scans obtained on EIGER at (2/3 2/3 1.0) at 35, 60 and 80 K. At 35 K a sharp peak with a continuum at higher energies is visible. This sharp peak looses intensity at 60 and 80 K, while the intensity of the continuum decreases much less. This means that the excitation spectrum changes between T_{N_1} and 80 K, where a maximum in the magnetic susceptibility suggests that antiferromagnetic correlation along the chains set in.

In the diffraction pattern at 55 K, shown in Figure 4.14, no magnetic Bragg peaks are visible. This suggests that for temperatures above T_{N_1} no long range order is present, therefore no staggered field is present above T_{N_1}.

$\mathbf{T_{N1} > T > T_{N_2}}$

At the first transition T_{N_1} the peak position changes and the intensity increases with decreasing temperature, as can be seen in the color plot in Figure 4.23 and in Figure 4.27 which compares scans at 35 K, 26 K and 18 K. These changes can be explained by staggered fields arising due to the interchain coupling. The continuum at high energies appears not to be influenced by the change in temperature. The sharp peak at 18 K is a bit broader and has higher intensity than the excitation at 35 K. Also at 18 K the onset of a shoulder at low energies is visible. This may already be the first sign of the magnetic phase transition at $T_{N_1} \approx 14$ K. At the second phase transition the weights of the staggered fields will change.

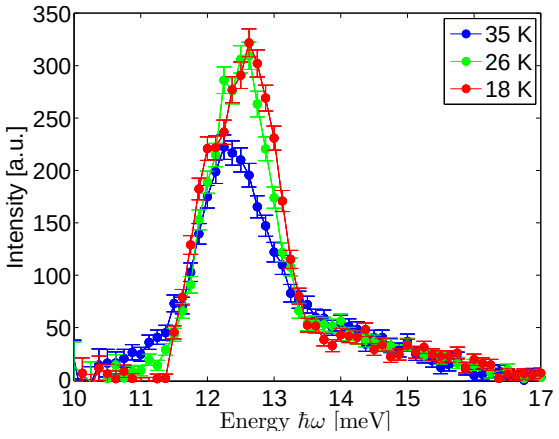

Figure 4.27: **Changes across the phase transition at $\mathbf{T_{N_1} \approx 28}$ K.** **Q** = (2/3 2/3 1.2) and T = 35 , 26 and 18 K. At the first magnetic phase transition the peak position changes and the intensity of the peak increases with decreasing temperature. The continuum at high energies does not change. The shoulder appearing at 18 K at low energies is already a precursor of the second magnetic phase transition at $T_{N_1} \approx 14$ K.

$T_{N_2} > T$

The second phase transition at T_{N_2} is illustrated in Figure 4.28 and can also be seen in Figure 4.23. In Figure 4.27 a shoulder appears at low energies already at 18 K. This shoulder grows in strength with decreasing temperature, and a second peak arises at high energies, see Figure 4.28. This change in peak position and intensity can be explained by changing weights of the staggered fields. Even though the transition temperature T_{N_2} is given to be 14 K [185], the scan at 11 K resembles more the data at 16 K than those at 6 K. While the phase transition takes place at a well defined temperature, the diffuse scattering visible in Figure 4.15 indicates that the correlations change. For example the uncorrelated chains in the magnetic structure for intermediate temperatures shown in Figure 4.17 become correlated with decreasing temperature.

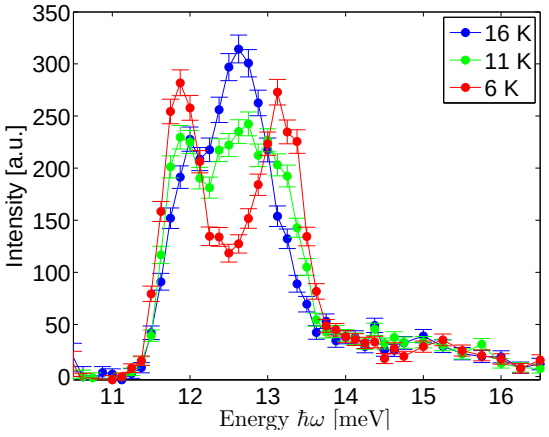

Figure 4.28: **Changes across the phase transition at $T_{N_2} \approx 14$ K.** **Q** = (2/3 2/3 1.2) and T = 16, 11 and 6 K. The intensity of the shoulder at low energies, which is already visible at 18 K, increases with decreasing temperatures. The broad peak in the middle looses intensity and a peak at higher energies appears.

Scans at (2/3 2/3 1.2) obtained on IN22 and EIGER at 2 K are shown in Figure 4.29 (a) and (b). At energies above the two intense peaks, additional weaker peaks are visible, especially in the data obtained on EIGER shown in Figure 4.29 (b). The onset of the intensity is at the first sharp peak, and no continuum is visible at lower energies. The only model discussed in section 4.2.1 which shows a similar sharp onset of intensity is the in-chain next nearest neighbor (nnn) model by Matsubara [182]. The relative intensity of the two high peaks at low energies is also best reproduced by this model. Figure 4.29 (c) shows the structure factor predicted by this model for L = 1.2.

Therefore, the in-chain next nearest neighbor (nnn) model by Matsubara [182] is used in the next section to fit our data.

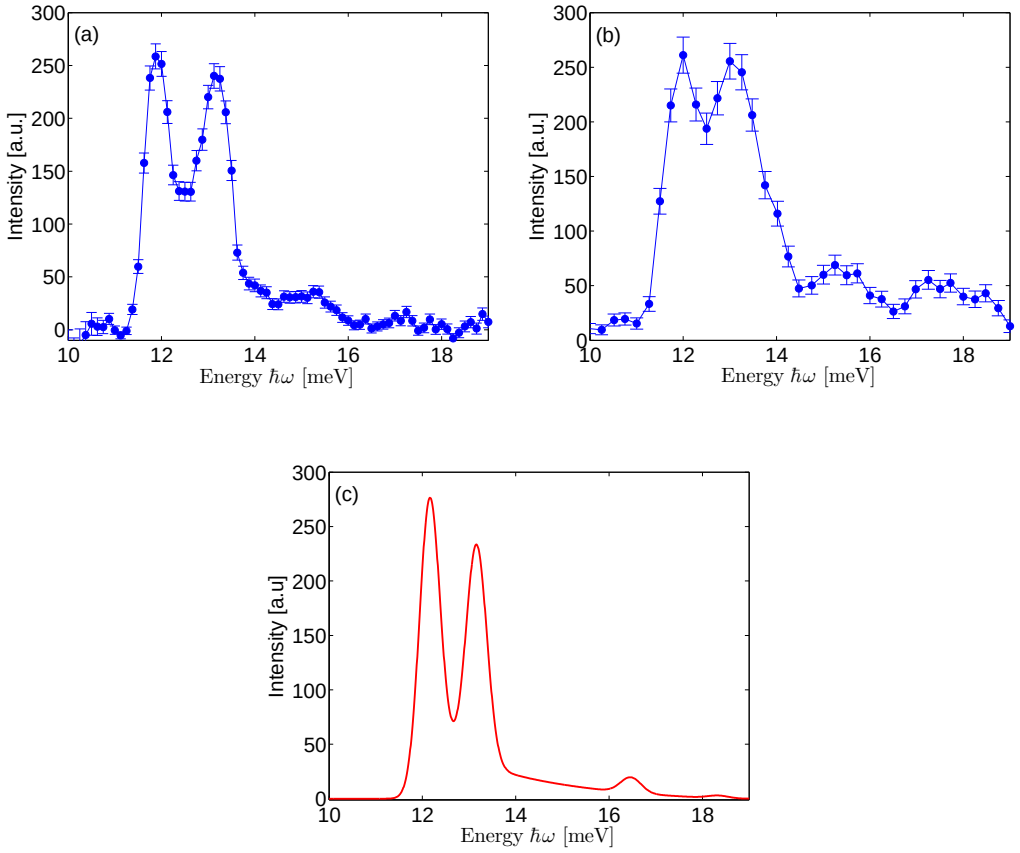

Figure 4.29: **Comparison between IN22 data at 2 K and the in-chain nnn model.** (a) Energy scan at (2/3 2/3 1.2) obtained on IN22 at 2 K with k_f = 1.97 Å^{-1} and (b) energy scan at (2/3 2/3 1.2) obtained on EIGER at 1.5 K with k_f = 2.662 Å^{-1}. (c) The in-chain nnn model by Matsubara [182] with L = 1.2 and the parameters J = 5.43 meV and J' = -1.07 meV, ϵ = 0.18 and h_{IC} = 0. The in-chain nnn model is the best model to describe our experimental data.

4.4.3 Results compared to the in-chain next nearest neighbor (nnn) model

The in-chain next nearest neighbor (nnn) model introduced by Matsubara is described in section 4.2.1, and by equations (4.5) and (4.6). In this section this model is fitted to the experimentally obtained data.

$\mathbf{T > T_{N_1}}$

For temperatures above T_{N_1} no magnetic order in the ab-plane is present and the staggered field is zero. Therefore, data obtained at temperatures above 30 K were fitted with the in-chain next nearest neighbor model where the interchain exchange was assumed to be zero.

Figures 4.21 (d) and (e) illustrate how the width increases with increasing temperature, while the bandwidth decreases. The change in width can be described by fitting the data with a Voigt, the convolution of a Lorentzian and a Gaussian. The Gaussian width describes the width arising from the resolution of the instrument and does not change with temperature. Therefore it is kept fixed to 0.6 meV, the Gauss width found at the lowest measured temperature, for all fits. The width of the Lorentzian is due to intrinsic damping of the excitations and increases with increasing temperature. The Lorentz width is left free to vary, and its change describes thermal broadening.

The decreasing bandwidth, which is a narrowing of the dispersion, is connected to a lower mobility of the solitons. In the in-chain next-nearest neighbor model this can be described by a change in ϵ. Unlike other parameters, such as width or intensity, ϵ was only fitted at temperatures where the entire dispersion along L was measured. In a second step the temperature dependence of ϵ so obtained was tested at other temperatures, where scans were available only for some values of L.

Figure 4.30 shows fits of the in-chain nnn model to energy scans at 35, 50 and 80 K. The interchain interaction was set to zero. The parameters obtained by the fits are given in table 4.2.

Parameter	Fitted value
J	5.64(7) meV
J'	0.83(6) meV
ϵ	0.182(1)-0.0008(1)*T
Lorentz Width	0.20(6)+0.010(1)*T

Table 4.2: Parameters found by fitting the in-chain next nearest neighbor model to experimental data for temperatures above T_{N_1}.

Figure 4.30 demonstrates the good agreement between the experimental data and the in-chain next nearest neighbor model over a broad temperature range. The peak position is reproduced well for the observed temperatures. Comparison to energy

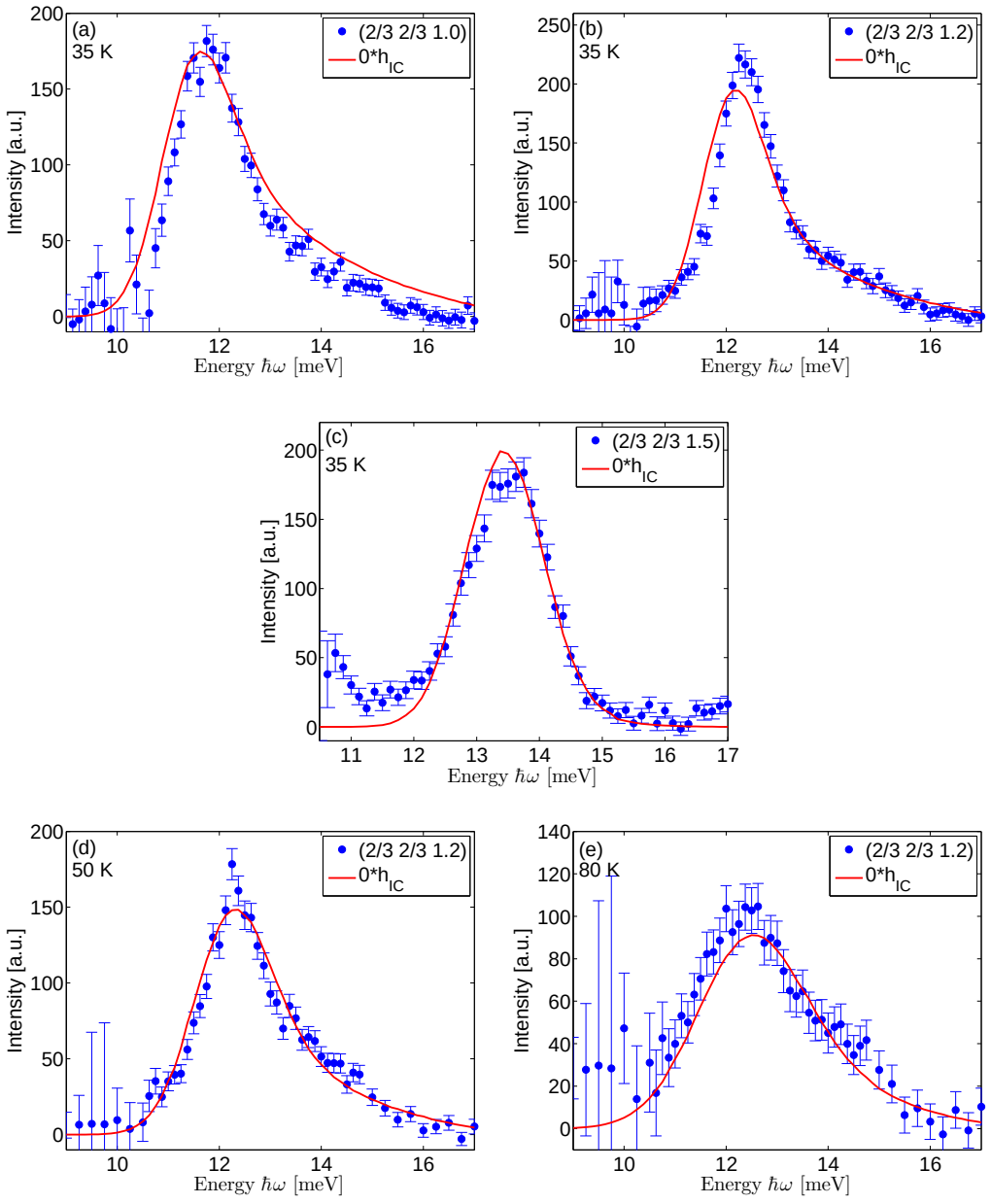

Figure 4.30: **Fits of the in-chain nnn model to data at $\mathbf{T > T_{N_1}}$.** Fits of the in-chain nnn model (red) without interchain interaction to experimental data (blue) at $\mathbf{Q}$ = (2/3 2/3 L). (a) 35 K, L = 1.0, (b) 35 K , L = 1.2, (c) 35 K, L = 1.5, (d) 50 K, L = 1.2 and (e) 80 K, L = 1.2. The parameters are $J = 5.64(7)$ meV and $J' = 0.83(6)$ meV. ϵ changes with temperature. At 35 K ϵ is 0.154(1), at 50 K it is 0.142(1) and at 80 K it is 0.118(1). The fits were convoluted with the resolution function using Trixfit [92, 93].

scans at 35 K which span the whole L range shows that the peak positions are also well reproduced for L different from 1.2. The peak position is also reproduced well for scans at (2/3 2/3 1.2) at temperatures not shown here. This shows that the temperature dependence found for ϵ is correct.

$\mathbf{T_{N_1} > T > T_{N_2}}$

The data at 18 K are fitted using the parameters obtained for $T > T_{N_1}$. 18 K is well away from the transition temperatures T_{N_1} and T_{N_2}, and data from LET, EIGER and IN22 are available. The staggered field is given by $h_{IC} = n \times J_{IC}$ where J_{IC} is the interchain interaction and n is a multiple arising from the magnetic structure. The possible staggered fields and their relative weights for the *intermediate* phase of $CsCoCl_3$ are given in Table 4.3. These staggered fields and their weights may also be used for $RbCoCl_3$, because the magnetic structures found for $CsCoCl_3$ and $RbCoCl_3$ at 18 K are equivalent except for a phase shift [185]. In the diffraction data a phase shift cannot be determined.

n	0	2	4	6
Weight	5/12	3/12	3/12	1/12

Table 4.3: Multiplicity and relative weights for the *intermediate* phase of $CsCoCl_3$ [60, 189].

When the structure reported by N. Hänni *et al.* [185] is used, the staggered fields arising and their weights are different. These values are given in table 4.4.

n	3/4	3
Weight	2/3	1/3

Table 4.4: Multiplicity and relative weights for the *intermediate* phase of $RbCoCl_3$ using the structure determined by N. Hänni *et al.* [185], shown in Figure 4.17 (a).

Figure 4.31 shows fits to the data at 18 K using the weights and staggered fields given in table 4.3. From these fits an interchain interaction of $J_{IC} = 0.0575(2)$ meV is obtained. The fit at (2/3 2/3 1.5) shows good agreement with the experimental data, width and peak position are reproduced excellently. For L = 1.2 the intensity is slightly too low. Still, the peak position and the continuum are reproduced correctly. At (2/3 2/3 1.0) the peak position of the fit is slightly displaced to higher energies, and the width and intensity of the continuum are overestimated.

Figure 4.32 shows fits to the data at 18 K, for which the multiplicities and weights given in table 4.4 are used. The interchain interaction obtained from these fits is $J_{IC} = 0.069(33)$ meV.

Fitting the data at 18 K with the multiplicities and weights from Table 4.4 shows even better agreement with the experimental data than the fits with the multiplicities

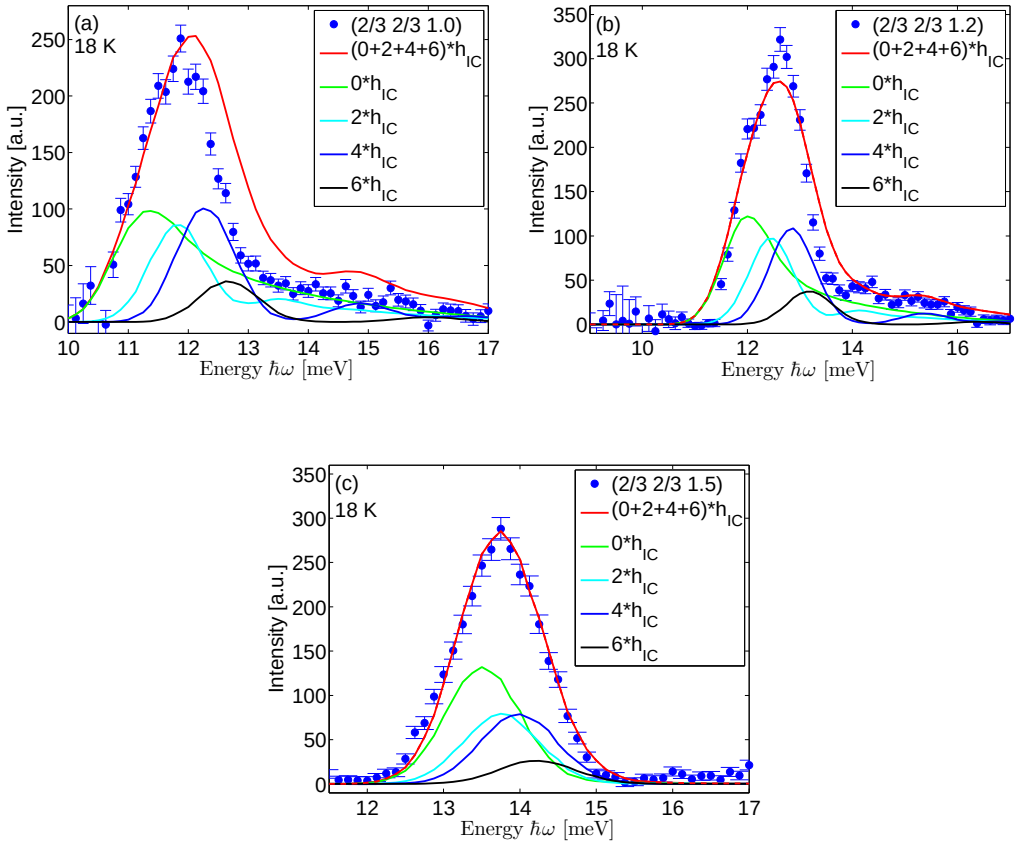

Figure 4.31: **Fits of the in-chain nnn model at $\mathbf{T_{N_1} > T > T_{N_2}}$.** Fits of the in-chain nnn model (red) with interchain interaction to experimental data (blue) obtained on IN22, at T = 18 K and **Q** = (2/3 2/3 L). The weights are given in Table 4.3. (a) L = 1.0, (b) L = 1.2 and (c) L = 1.5. The parameters used for the fits are J = 5.64 meV and J' = 0.83 meV, ϵ = 0.168 and J_{IC} = 0.0575(2) meV. The fits were convoluted with the resolution function using Trixfit [92, 93].

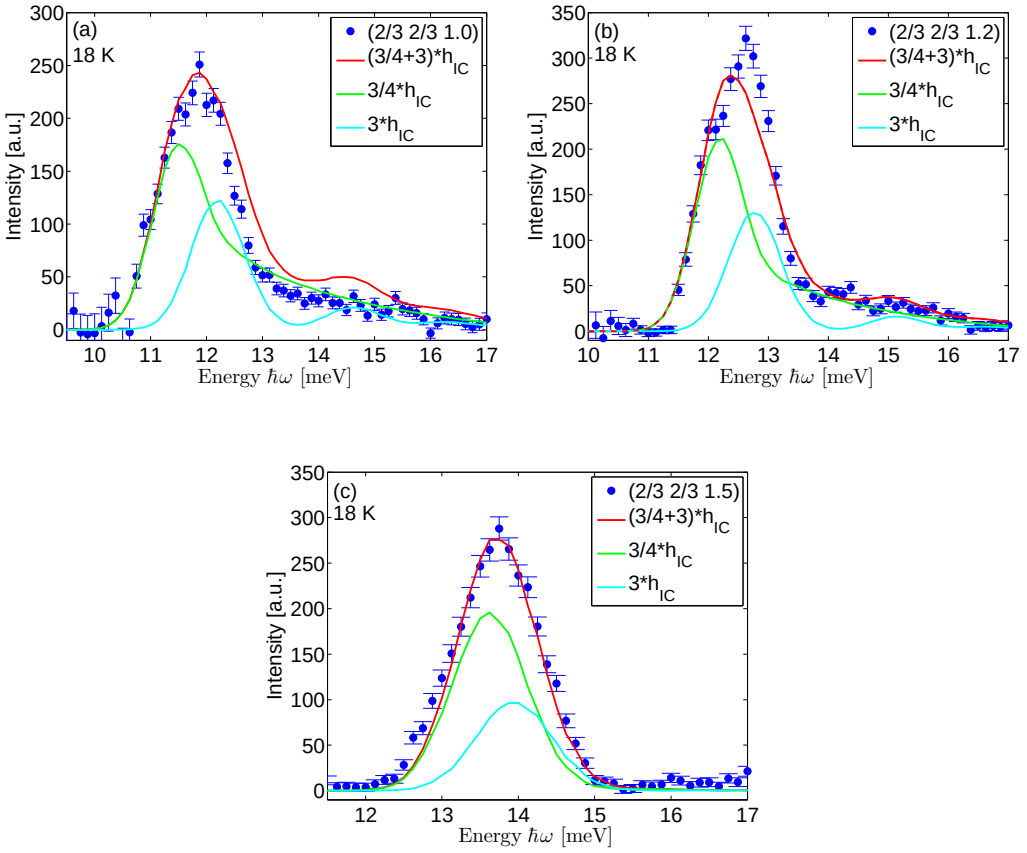

Figure 4.32: **Fits for the in-chain nnn model at $\mathbf{T_{N_2} < T < T_{N_1}}$.** Fits of the in-chain nnn model (red) with interchain interaction to experimental data (blue) obtained on IN22, at T = 18 K and **Q** = (2/3 2/3 L). The multiplicities and weights are given in Table 4.4. (a) L = 1.0, (b) L = 1.2 and (c) L = 1.5. The parameters used for the fits are $J = 5.64$ meV and $J' = 0.83$ meV, $\epsilon = 0.168$ and $J_{\mathrm{IC}} = 0.069(33)$ meV. The fits were convoluted with the resolution function using Trixfit [92, 93].

and weights from Table 4.3 shown in Figure 4.31. Again agreement between the fit and the experimental data is excellent at (2/3 2/3 1.5). At (2/3 2/3 1.0) the peak position and intensity of the sharp mode are reproduced better than in Figure 4.31. Only for $\mathbf{Q}$ = (2/3 2/3 1.2) the fitted peak position is at lower energies than in the experimental data.

$\mathbf{T_{N_2} > T}$

For temperatures below T_{N_2} the magnetic structure shown in Figure 4.19 has two components. Since the magnetic peak associated with $\mathbf{k}_3$ is far weaker than the one associated with $\mathbf{k}_2$, one may assume that the dominant structure is the same as found by Lockwood for $RbCoCl_3$ [190] and by Mekata for $CsCoCl_3$ [189]. Therefore, it is assumed that the possible staggered fields and their weights are similar to those given in table 4.5.

n	0	6
Weight	2/3	1/3

Table 4.5: Multiplicity and relative weights for the low temperature phase of $CsCoCl_3$. These staggered fields and weights also arise for $RbCoCl_3$ when $\mathbf{k}_3$ is neglected. Lockwood observed a structure which gives rise to these weights for $RbCoCl_3$ [190].

If the propagation vector $\mathbf{k}_3$ is included, the magnetic structure is the one found by N. Hänni *et al.*, and the staggered fields and their weights change. The new values are given in table 4.6.

n	1/2	2	-1/4	5
Weight	2/6	1/6	2/6	1/6

Table 4.6: Multiplicity and relative weights for the low temperature phase of $RbCoCl_3$ when the propagation vector $\mathbf{k}_3$ is included. The corresponding structure is shown in Figure 4.19 and described in reference [185].

Fig 4.33 shows fits to the data at 2 K using the staggered fields and weights for $CsCoCl_3$ given in table 4.5. The fits using the parameters found at higher temperatures reproduce the sharp modes observed at 2 K. At (2/3 2/3 1.0) the two sharp peaks and their relative intensities are reproduced correctly, but the peak positions are slightly shifted. The fit shows a small peak around 16 meV where no excitation is visible in the data. This peak also arises at (2/3 2/3 1.2), and there also the relative intensities of the two sharp modes are not reproduced correctly by the model. The fit at (2/3 2/3 1.5) reproduces the sharp mode at the correct energy, but its intensity is too low and the width too small.

Figure 4.34 shows fits to the data at 2 K using the weights and staggered fields given in Table 4.6. Agreement between experimental data and these fits is poor

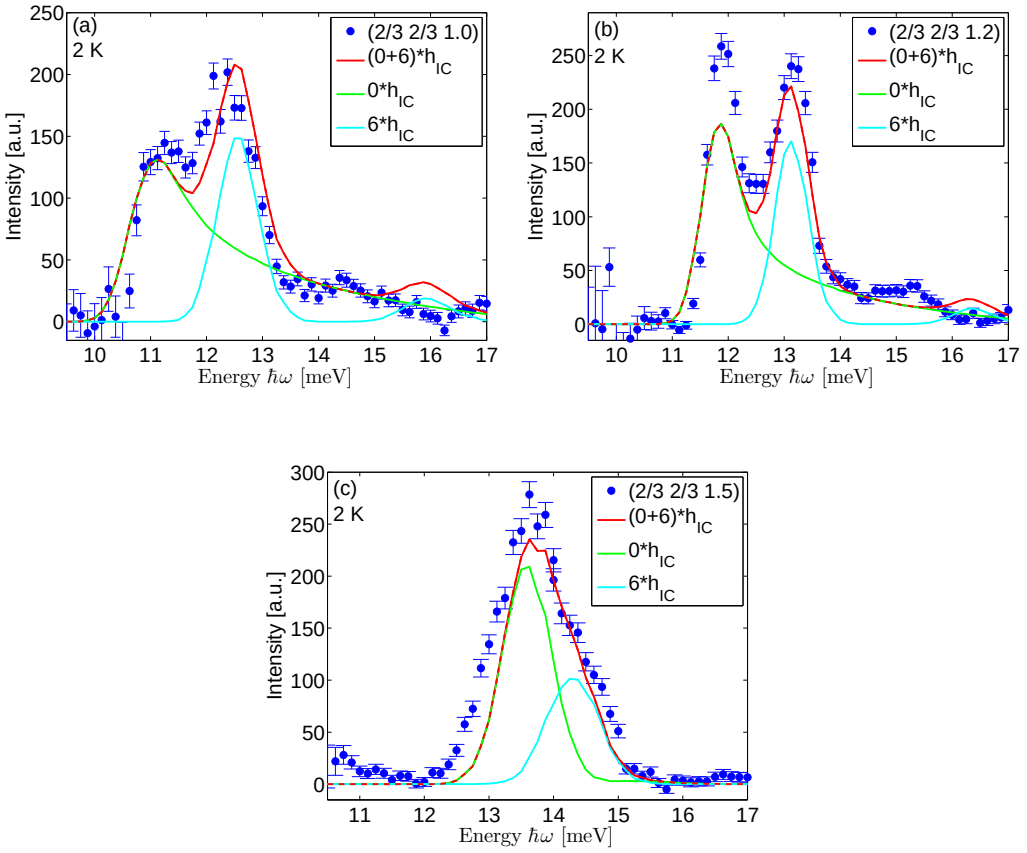

Figure 4.33: **Fits with the in-chain nnn model at $\mathbf{T_{N_2} > T}$.** Fits of the in-chain nnn model (red) to experimental data (blue) obtained on IN22, at T = 2 K and **Q** = (2/3 2/3 L). The staggered fields and their weights are given in Table 4.5. (a) L = 1.0, (b) L = 1.2 and (c) L = 1.5. The parameters used for the fits are $J = 5.64$ meV and $J' = 0.83$ meV, $\epsilon = 0.1804$ and $J_{\mathrm{IC}} = 0.0575$ meV. The fits were convoluted with the resolution function using Trixfit [92, 93].

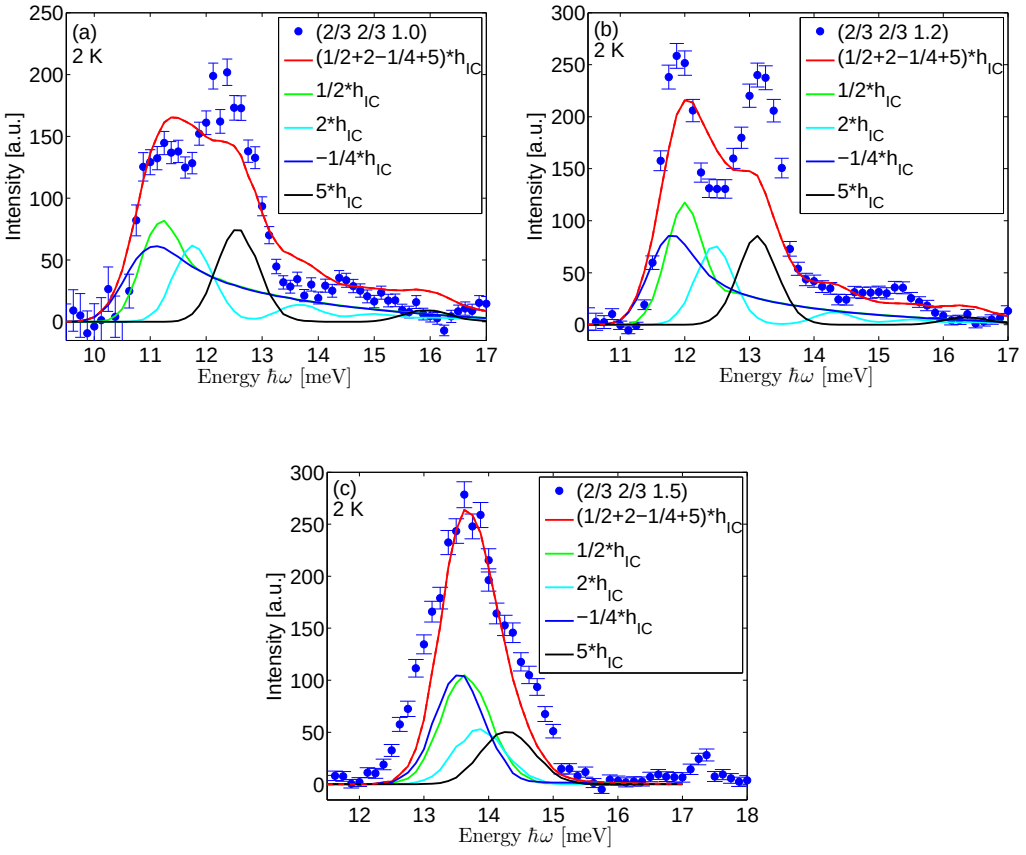

Figure 4.34: **Fits with the in-chain nnn model at $\mathbf{T} < \mathbf{T_{N_2}}$.** Fits of the in-chain nnn model (red) to experimental data (blue) obtained on IN22 at T = 2 K and **Q** = (2/3 2/3 L). The staggered fields and their weights are given in Table 4.6. (a) L = 1.0, (b) L = 1.2 and (c) L = 1.5. The parameters used for the fits are $J = 5.64$ meV and $J' = 0.83$ meV, $\epsilon = 0.168$ and $J_{\mathrm{IC}} = 0.069$ meV.

except for $\mathbf{Q} = (2/3\ 2/3\ 1.5)$. Both for $\mathbf{Q} = (2/3\ 2/3\ 1.0)$ and $(2/3\ 2/3\ 1.2)$ the two sharp modes visible in the experimental data are not reproduced by the fits.

4.4.4 Temperature dependence of the weights

So far only data above T_{N_1} and at specific temperatures well away from the magnetic order transition temperatures were studied. At the first magnetic ordering transition interchain interactions begin to play a role, and this leads to staggered fields. These staggered fields change at the second magnetic ordering transition. The staggered fields lead to a splitting of the continuum into bound states. In order to gain a better understanding of the behavior of $RbCoCl_3$, and how the staggered fields change as a function of temperature, the weights for all data at $\mathbf{Q}$ = (2/3 2/3 1.2) between 2 K and 80 K are analyzed. Since the fits with the staggered fields and weights given in Table 4.5 work much better, the multiplicities for the $CsCoCl_3$ structure [189] (which was also found for $RbCoCl_3$ by Lockwood [190]) and the parameters found in the corresponding fits are used in this section. The resulting temperature dependences of the weights are shown in Figure 4.35.

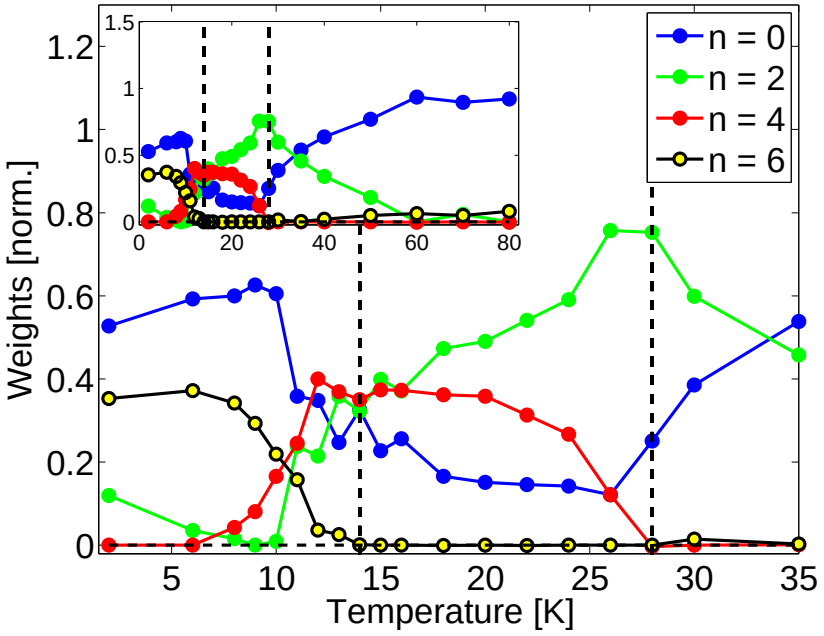

Figure 4.35: **Temperature dependence of the weights for staggered fields.** Weights for the staggered fields obtained by fitting experimental data at $\mathbf{Q}$ = (2/3 2/3 1.2). The total weight has been normalized to one. The error bars are omitted for better visibility. The dotted lines indicate the transition temperatures. The inset shows the whole temperature range from 2 to 80 K while the the weights for temperatures lower than 35 K are shown in more detail.

At 80 K, where correlations along the chains set in n = 0 carries the full weight (n = 0 is equal to no staggered field). The weights of the other multiplicities are negligible at this temperature. At 60 K the weight of n = 2 starts to increase. It is possible that a peak arising from a staggered field with n = 2 is covered by the broad

peak observed at temperatures above T_{N_1}. Close to the first transition temperature T_{N_1} the weight for n = 0 decreases, and below T_{N_1} the weight for n = 2 decreases while the weight for n = 4 increases. The weights for n = 2 and n = 4 should be equal, but the weight for n = 2 decreases continuously. Even though n = 0 should still account for about 40 % of the spectral weight, its weight is significantly smaller. At the second transition temperature T_{N_2} the weights change again. The biggest change in weights is below 14 K (indicated by a dotted line), which is the transition temperature. This indicates that the weights of the staggered fields change not only at T_{N_1} and T_{N_2}, but continuously as a function of temperature as the weights follow the development of correlations in the system.

4.5 Discussion

$RbCoCl_3$ is a quasi-one dimensional Ising-like antiferromagnet. It develops antiferromagnetic correlations along the c-axis below T ≈ 80 K, and undergoes two magnetic phase transitions around 28 K and 14 K. For temperatures above T_{N_1} a broad continuum is observed. Such a continuum is predicted for the excitation spectrum of isolated antiferromagnetic chains [182, 183]. Below T_{N_1} correlations develop in the ab-plane, as interchain interaction sets in. As a result bound states are observed. With decreasing temperature the maximum of the dispersion moves to higher energies. The increased bandwidth of the dispersion with decreasing temperature comes from a reduced mobility at higher temperatures, and has been observed also in other systems, e.g. in the dimer system $TlCuCl_3$. There, the temperature dependence of the dispersion was described by a mean field theory, see Troyer, Tsunetsugu and Würtz [197, 198].

To describe the temperature dependence of the bandwidth of the dispersion in $RbCoCl_3$, ϵ is varied with temperature. This is a purely phenomenological description of the temperature dependence of the data.

Goff [60] fits his $CsCoCl_3$ data at 25 K, which is above the first magnetic ordering temperature for $CsCoCl_3$, without a staggered field and the same ϵ for all temperatures, but the fits at lower temperatures are shifted in energy. 25 K is not far above 21 K, the transition temperature for $CsCoCl_3$. Therefore the bandwidth of the dispersion did not narrow much at 25 K, compared to the lowest observed temperature. This would also explain the shift of the fits at lower temperatures. On the other hand, Lehmann questions the idea of single ideal chains for temperatures above T_{N_1} [161]. In any case, a model is needed which takes the temperature into account in a more refined way than by just changing the staggered fields and their weights at each magnetic phase transition and incorporating a changing ϵ.

The change in width of the experimental $RbCoCl_3$ data due to thermal broadening has also been described as a function of temperature.

Comparing the experimental data at 2 K to the theoretical models introduced in section 4.2.1 leads to the conclusion that the in-chain next nearest neighbor (nnn) model fits the data best.

The in-chain nnn model without an interchain interaction shows good agreement with the experimental data for temperatures between 80 K and $T_{N_1} \approx 28$ K. In this temperature range $RbCoCl_3$ can be described by isolated Ising chains with an XY-component and next nearest neighbor in-chain exchange, which enables one to distinguish between spin wave and soliton states. The change of the spectrum within this temperature range indicates that correlations develop below 80 K, and that these correlations are getting stronger with decreasing temperature. The parameters for the in-chain next nearest neighbor model were obtained by fits with this model at temperatures above T_{N_1}. The energy scale $2J \approx 12.9$ meV is higher than expected from optical spectroscopy measurements, and is comparable to the energy scale $2J \approx$

12.8 meV for $CsCoCl_3$. This means that the critical magnetic field is not easier to reach experimentally for $RbCoCl_3$ than for $CsCoCl_3$.

The interchain interaction is determined by fitting the in-chain nnn model with an interchain interaction to experimental data obtained at 18 K, which is below T_{N_1}. For intermediate temperatures between T_{N_1} and T_{N_2} two magnetic structures, which differ only by a phase, are proposed [185, 189]. Fits with the staggered fields and weights arising from both structures show good agreement with the experimental data. The magnetic structure determined for $RbCoCl_3$ by N. Hänni *et al.* [185] leads to slightly better agreement with the data. But it cannot be unambiguously determined which of the two suggested magnetic structures is the correct one.

The remarkably strong diffuse scattering observed in diffraction scans at intermediate temperatures can be explained by both proposed magnetic structures. At intermediate temperatures, in the structure suggested for $CsCoCl_3$, 1/3 of the chains show no correlations within the chains. These uncorrelated chains lead to diffuse scattering, while the correlated chains give rise to Bragg scattering. The structure determined by N. Hänni *et al.* can be explained as consisting of different ordered domains. While the ordered domains lead to sharp Bragg peaks, the disorder at the boundaries gives rise to diffuse scattering. An example for a material where long-range order exists in chains along the c-axis, but not in the ab-plane, is the frustrated Ising-like magnet $Ca_3Co_2O_6$. Here the frustration in the ab-plane leads to a "partially disordered antiferromagnetic state", where only two out of three sublattices in the ab-plane are ordered [199].

When cooling further below T_{N_2}, the staggered fields change and in the structure for $CsCoCl_3$ the correlations in the unordered chains extend. In the structure determined by N. Hänni *et al.* the correlations in the ab-plane change, and the domains grow.

However, below T_{N_2} fits resulting from the structure determined by N. Hänni *et al.* [185] fail to reproduce the two intense modes correctly. Fits using the structure found for $CsCoCl_3$ at low temperatures do not show perfect agreement, especially for the continuum at energies above the sharp modes, but reproduce the main features of the excitation spectrum at 2 K correctly.

At high and intermediate temperatures, the excitation spectrum of $RbCoCl_3$ shows good agreement with the excitation spectrum of antiferromagnetic Ising chains with next nearest neighbor in-chain interaction and interchain interaction below T_{N_1} and changing anisotropy. Below T_{N_2} this model is not such a good description of the experimental data. Additional terms in the Hamiltonian may be necessary, such as a next nearest neighbor interchain interaction. The effect of this interaction, though small, would be a further splitting of the bound states at low temperatures. Fits to high-resolution neutron scattering data obtained on the time-of-flight spectrometer LET show that a next nearest neighbor interchain interaction is needed to describe the data at 18 K satisfactorily [191] when the magnetic structure determined for $CsCoCl_3$ is used. This also shows that the structure found by N. Hänni *et al.*

cannot explain the time-of-flight data at 18 K. Introducing a next nearest neighbor interchain interaction is supported by the fact that the perfect honeycomb structure is stabilized by a such an interaction [161, 183].

A better knowledge of the magnetic structure of $RbCoCl_3$ will help to identify the staggered fields which arise. Monte Carlo simulations with the *cluster heat bath method* [192, 193], as done by Koseki and Matsubara for $CsCoCl_3$ and $CsCoBr_3$ [194], and studying the diffuse scattering could provide further insight into the magnetic order in $RbCoCl_3$, especially close to the phase transitions.

Both magnetic ordering transitions can be described by changing the weights of the staggered fields. Fitting the weights of the different staggered fields shows that these weights deviate from the ideal values obtained for the magnetic structure, and indicates that the weights of the staggered fields change continuously as a function of temperature, as the weights follow the change of correlations in the system. The diffuse scattering at intermediate temperatures indicates that flucutations are important in this temperature range. Matsubara, who introduced the in-chain next nearest neighbor model, also determined weights from magnetic Raman scattering data for $RbCoCl_3$ which deviate from the ideal ones [182]. These weights are compared in Table 4.7.

n	0	2	4	6
$T < T_{N_2}$				
Ideal	66 %	0	0	33 %
Fit (2 K)	52 %	12 %	1 %	35 %
Matsubara (2 K) [182]	31 %	19 %	13 %	37%
$T > T_{N_2}$				
Ideal	42 %	25 %	25 %	8 %
Fit (18 K)	18 %	45 %	35 %	2 %
Fit (13 K)	25 %	38 %	35 %	2 %
Matsubara (13 K) [182]	18 %	40 %	29 %	13 %

Table 4.7: Weights for the different staggered fields above and below the second magnetic phase transition. The experimentally obtained weights deviate from the ideal ones.

The weights obtained by the fits at 2 K are different from both the ideal ones and those obtained by Matsubara. The experimentally obtained weights at 18 K are close to the ones obtained by Matsubara at 13 K (which are still effected by the magnetic phase transition at T_{N_2}). One problem with fitting the weights is that due to the experimental resolution, the contributions of the different staggered fields cannot be clearly separated. The high-resolution time-of-flight data obtained on LET have better resolution, and provide more information about the number of modes observed and therefore the number and strengths of the different staggered fields. Time-of-flight data for $RbCoCl_3$ are only available at a few temperatures,

but understanding the excitations of $RbCoCl_3$ at these temperatures will also help to understand the excitation spectrum as a function of temperature.

- $RbCoCl_3$ is a model material for the quasi-one dimensional Ising-like antiferromagnet.
- Below 80 K $RbCoCl_3$ develops antiferromagnetic correlations along the c-axis. A broad continuum is observed, as predicted for the excitation spectrum of isolated antiferromagnetic Ising-like chains. The energy gap is determined. The increasing bandwidth of the dispersion with decreasing temperature can be described phenomenologically by varying the anisotropy term ϵ with temperature.
- At a first magnetic ordering temperature $T_{N_1} \approx 28$ K correlations develop in the ab-plane due to interchain interaction. As a consequence bound states are observed. These bound states split at a second magnetic ordering temperature $T_{N_2} \approx 14$ K, where the magnetic structure changes as well. Fluctuations are important at intermediate temperatures.
- For temperatures above T_{N_2} good agreement is found between the excitation spectrum of $RbCoCl_3$ and theoretical predictions for the excitation spectrum of antiferromagnetic Ising chains with next nearest neighbor in-chain interaction consisting of soliton-pair states.
- Below T_{N_2} this model reproduces the rough features of the experimental data, but discrepancies in the details indicate additional terms in the Hamiltonian may be needed.
- Even though the magnetic ordering transitions can be described by changing weights of the staggered fields, fits indicate that the weights change continuously as a function of temperature.

Chapter 5

Summary and Outlook

For this thesis two spin chain materials were studied. One of them is a model Heisenberg chain, and the other a model Ising chain.

The spin-$\frac{1}{2}$ Heisenberg antiferromagnetic chain $CuSO_4$*$5D_2O$

By fitting the normalized and convoluted two- plus four-spinon dynamical structure factor, calculated by Caux [76], to the data at 0.15(2) K one is able to obtain the scaling factor for an absolute normalization of the experimental data. This, in turn, makes it possible to compare experimental data at higher temperatures to theoretical predictions using the same normalization. The finite temperature behavior of $CuSO_4$*$5D_2O$ is qualitatively and quantitatively well described by the quantum Monte Carlo data by Rahnavard and Brenig [115]. The experimentally obtained static and dynamic structure factor and susceptibility were also compared to scaling relations. Agreement is good over a wide temperature range, but not for all measured temperatures. Deviations occur especially at high temperatures. We show that the data at 31.5(6) K ($\sim$10 J) correspond to numerical data for T $\rightarrow \infty$, and that even at these temperatures a spinon continuum is observed. This indicates that the system behaves like a quantum system and not like a classical one, for which one would expect single spin flips at infinite temperatures. With increasing temperature, spectral weight decreases at the antiferromagnetic zone center and increases close to h $\rightarrow$ 0,1 at low energies. We were unable to show definitely that the origin of this scattering is spin diffusion. More detailed studies need to be done to reveal the origin of this increased intensity close to h $\rightarrow$ 0,1 and $\hbar\omega \rightarrow 0$. It would also be interesting to compare our experimental data at temperatures higher than 6.2(2) K to quantum Monte Carlo data by Rahnavard and Brenig, when available.

In summary the excitation spectrum of $CuSO_4$*$5D_2O$ is excellently described by the excitation spectrum of a spin-$\frac{1}{2}$ Heisenberg antiferromagnetic chain, and shows quantum behavior up to high temperatures.

The Ising-like antiferromagnetic chain $RbCoCl_3$

Neutron scattering was employed to study magnetic order and excitations in the quasi one-dimensional Ising system $RbCoCl_3$. The magnetic structure of $RbCoCl_3$ found in the intermediate phase agrees, up to a phase, with previous results, while the magnetic structure found below the second phase transition is different from the one previously assumed. A possible explanation is the existence of different domains. Diffuse scattering is remarkably strong close to the phase transitions, and studying it could provide insight into the magnetic order of $RbCoCl_3$. Monte Carlo simulations of the magnetic structure reproduced the main features, but failed to include all details. Improved Monte Carlos simulations incorporating the *cluster heat bath method* [192, 193] are planned.

Excitations in $RbCoCl_3$ are solitons. We observed the excitation spectrum of $RbCoCl_3$ at temperatures between 2 K and 80 K, where correlations in the chains set in. In this thesis the observed excitation spectrum was compared to a theoretical model introduced by Matsubara [182], the *in-chain next nearest neighbor model*. Agreement with this model is good at low energies, but discrepancies remain at higher energies, where it does not describe the observed continuum correctly. Both phase transitions can be described by modifying the weights of the different staggered fields, which corresponds to a change in the magnetic structure. Because the in-chain next nearest neighbor model only accounts for the temperature dependence through changes in the staggered fields, the increasing bandwidth of the dispersion with increasing temperature is described purely phenomenologically. A theoretical model which also takes temperature dependence into account is needed.

The different staggered fields still need to be understood better. Recently, simulations on the excitation spectrum of $RbCoCl_3$ with an applied external transverse field have become available from the Group of H.B. Braun from University College Dublin [200] and show interesting features. One such simulation is shown in Figure 5.1 (a). An experiment is planned to study the excitations in $RbCoCl_3$ with an applied transverse field. Figure 5.1 (b) shows LET data [191] where high statistics scans were made, the resolution of these scans should be sufficient to determine changes in the excitation spectrum when a transverse magnetic field is applied.

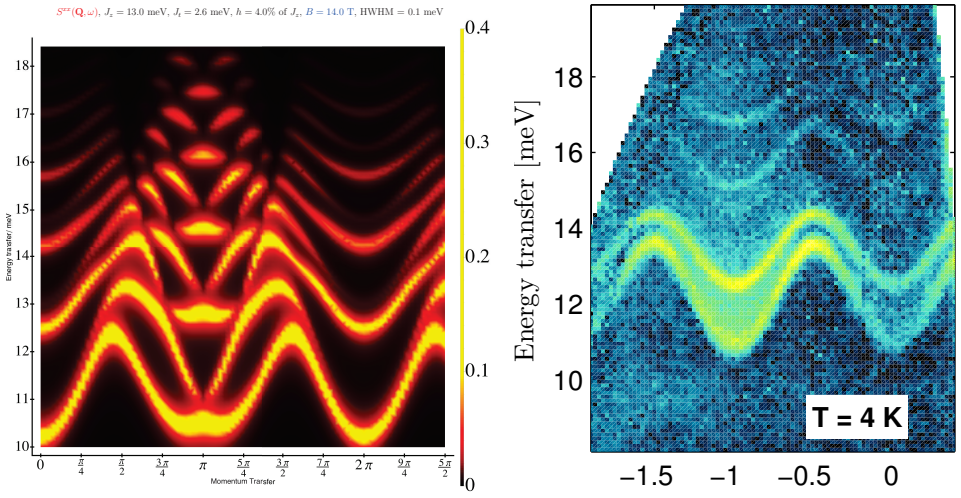

(a) (b)

Figure 5.1: **Excitation spectrum of $RbCoCl_3$**
(a) Simulation of the excitation spectrum of $RbCoCl_3$ with an external transverse magnetic field by L.P. English and H.B. Braun from University College Dublin [200]. (b) High statistics data from LET. Figure from M. Mena [191], the x-axis is the momentum transfer L [r.l.u]. The possible resolution at low temperatures at LET should be sufficient to distinguish the splitting arising from a transverse magnetic field.

Bibliography

[1] S. Sachdev. *Quantum Phase Transitions*. Cambridge University Press, 1999.

[2] M. Enderle. *Neutrons et Magnétisme: Neutrons and Magnetism*. EDP Sciences, 2012.

[3] Ch. Rüegg. private communication.

[4] S. Blundell. *Magnetism in Condensed Matter*. Oxford University Press, 2001.

[5] F. Bloch. *Z. Physik*, 61:206, 1930.

[6] K. Yosida. *Theory of magnetism*. Springer, 1998.

[7] T. Holstein and H. Primakoff. *Phys. Rev.*, 58:1908, 1940.

[8] C. Timm. Theory of magnetism. International Max Planck Research School for Dynamical Processes in Atoms, Molecules and Solids, 2011.

[9] N.B. Brockhouse. *Phys. Rev.*, 106:859, 1957.

[10] N.D. Mermin and H. Wagner. *Phys. Rev. Lett.*, 17:1133, 1966.

[11] L.J. De Jongh and A. R. Miedema. *Adv. Phys.*, 1:23, 1974.

[12] A.K. Bera *et al. Phys. Rev. Lett.*, 89:094402, 2014.

[13] R. Coldea *et al. Science*, 327:177, 2011.

[14] S.E. Nagler *et al. Phys. Rev. B*, 44:12361, 1991.

[15] D.A. Tennant *et al. Phys. Rev. B*, 52:13368, 1995.

[16] Y. Endoh *et al. Phys. Rev. Lett.*, 32:170, 1974.

[17] I.U. Heilmann *et al. Phys. Rev. B*, 18:3530, 1978.

[18] I.A. Zaliznyak *et al. Phys. Rev. Lett.*, 93:87202, 2004.

[19] H. Woo *et al. Physica B: Condensed Matter*, 350:e249, 2004.

[20] S. Sachdev. *Science*, 21:475, 2000.

[21] C. Rüegg *et al. Nature*, 423:62, 2003.

[22] P. Merchant *et al. Nature Physics*, 10:373, 2014.

[23] P.L.H. Merchant. *Excitations and Criticality in Quantum Magnets*. PhD thesis, University College London, 2013.

[24] S. Sachdev. *REv. Mod. Phys.*, 75:913, 2003.

[25] M.Greiner *et al. Nature*, 415:39, 2002.

[26] S. Mitsuda *et al. J. Phys. Soc. Jpn.*, 60:1885, 1991.

[27] O.A. Petrenko *et al. J. Phys. Cond. Matt.*, 17:2741, 2005.

[28] F. Ye *et al. Phys. Rev. Lett.*, 99:157201, 2007.

[29] M. Niel *et al. Physica*, 86B:702, 1977.

[30] K. Hirakawa *et al. J. Phys. Soc. Jpn.*, 51:1119, 1982.

[31] K. Hirakawa *et al. J. Phys. Soc. Jpn.*, 52:1799, 1983.

[32] K. Hirakawa *et al. J. Phys. Soc. Jpn.*, 52:2882, 1983.

[33] K. Hirakawa *et al. J. Phys. Soc. Jpn.*, 52:1814, 1983.

[34] J.N. Reimers. *Phys. Rev. B*, 45:7287, 1992.

[35] S.-H. Lee *et al. Nature*, 418:856, 2002.

[36] S. Ji *et al. Phys. Rev. Lett.*, 103:37201, 2009.

[37] Y.J. Uemura *et al. Phys. Rev. Lett.*, 73:3306, 1994.

[38] M.P. Shores *et al. J. Am. Chem. Soc.*, 127:13462, 2005.

[39] T.-H. Han *et al. Nature*, 492:406, 2012.

[40] M. Enderle *et al. Europhysics Letters*, 70:237, 2005.

[41] O. Mentré *et al. Phys. Rev. B*, 80:180413(R), 2009.

[42] A.P. Ramirez *et al. Nature*, 426:55, 2003.

[43] T. Kimura *et al. Phys. Rev. B*, 73:220401(R), 2006.

[44] T. Kimura *et al. Phys. Rev. B*, 68:60403(R), 2003.

[45] T. Kimura *et al. Nature*, 426:55, 2003.

[46] M. Mourigal *et al. Phys. Rev. B*, 83:100409(R), 2011.

[47] F.D.M. Haldane. *Physics Letters A*, 93:464, 1983.

[48] I. Affleck. *J. Phys.: Condens. Matter*, 1:3047, 1989.

[49] W.J.L. Buyers *et al. Phys. Rev. Lett.*, 56:371, 1986.

[50] M. Enderle *et al. Europhys. Lett.*, 25:717, 1994.

[51] M. Kenzelmann *et al. Phys. Rev. Lett.*, 87:17201, 2001.

[52] I.A. Zaliznyak *et al. Phys. Rev. Lett.*, 87:17202, 2001.

[53] F.D.M. Haldane. *Phys. Rev. Lett.*, 45:1358, 1980.

[54] S. Tomonaga. *Prog. Theor. Phys.*, 5:544, 1950.

[55] J.M. Luttinger. *J. Math. Phys.*, 4:1154, 1963.

[56] A.M. Tsvelik. *Quantum Field Theory in Condensed Matter Physics*. Cambridge University Press, 2 edition, 2003.

[57] I. Zaliznyak. *Nature Materials*, 4:273, 2005.

[58] B. Lake *et al. Nature Materials*, 4:329, 2005.

[59] S.E. Nagler *et al. Phys. Rev. B*, 27:1784, 1983.

[60] J.P. Goff *et al. Phys. Rev. B*, 52:22, 1995.

[61] J. Villain. *IOP Conference Series*, 64:239, 1982.

[62] S.E. Nagler *et al. Phys. Rev. Lett.*, 49:590, 1982.

[63] S.E. Nagler *et al. Phys. Rev. B*, 28:3873, 1983.

[64] H.B. Braun *et al. Nature Physics*, 1:159, 2005.

[65] A. Oosawa *et al. J. Phys. Soc. Jpn.*, 75:015002, 2006.

[66] Y. Nishiwaki *et al. J. Phys. Soc. Jpn.*, 75:034707, 2006.

[67] A. Oosawa *et al. J. Phys. Soc. Jpn.*, 75:074719, 2006.

[68] S.J. Blundell and K.M. Blundell. *Concepts in Thermal Physics*. Oxford University Press, 2009.

[69] F.D.M. Haldane. *Phys. Rev. Lett.*, 66:1529, 1991.

[70] P.A. Marchetti *et al. J. Phys.: Conf. Ser.*, 400:022066, 2012.

[71] L.D. Faddeev and L.A. Takhtajan. *Physics Letters*, 85A:375, 1981.

[72] M. Mourigal *et al. Nature Physics*, 9:435, 2013.

[73] M. Mourigal *et al.* arXiv:1306.4678, 2013.

[74] J.P. des Cloizeaux and J.J. Pearson. *Phys. Rev.*, 128:2131, 1962.

[75] B. Lake *et al. Phys. Rev. Lett.*, 111:137205, 2013.

[76] J.S. Caux and R. Hagemans. *J. Stat. Mech: Theory Exp.*, page P 12013, 2006.

[77] A.R. Miedema *et al. Physica*, 28:119, 1962.

[78] S. Wittekoek *et al. Physica*, 39:293, 1968.

[79] L.W. Lovesey. *Theory of Neutron Scattering from Condensed Matter*, volume 1. Oxford University Press, 1984.

[80] L.W. Lovesey. *Theory of Neutron Scattering from Condensed Matter*, volume 2. Oxford University Press, 1984.

[81] G.L. Squires. *Introduction to the Theory of Thermal Neutron Scattering*. Cambridge University Press, 1978.

[82] D.S. Sivia. *Elementary Scattering Theory*. Oxford University Press, 2011.

[83] P.J. Brown *et al.* International tables for crystallography, volume c, sections 4.5 and 6.1.

[84] J. Mesot A. Furrer and Th. Strässle. *Neutron Scattering in Condensed Matter Physics*. World Scientific Publishing, 2009.

[85] G. Shirane *et al. Neutron scattering with a triple-axis spectrometer : basic techniques*. Cambridge University Press, 2004.

[86] S. Grossjohann and W. Brenig. *Phys. Rev. B*, 79:94409, 2009.

[87] P.C. Hohenberg and W.F. Brinkman. *Phys. Rev. B*, 10:128, 1974.

[88] R.M. Moon *et al. Phys. Rev.*, 181:920, 1969.

[89] M. Blume. *Phys. Rev.*, 130:1670, 1963.

[90] R. Steward. Polarized neutrons. 12. Oxford School on Neutron Scattering, University of Oxford, St. Annes College, Sep 2011.

[91] J. Saroun and J. Kulda. *Physica B*, 234:1102, 1997.

[92] D.A. Tennant and D. McMorrow. Rescal for matlab, 1995.

[93] D. McMorrow. Trixfit function for fitting triple-axis data. Private Communication, 2001.

[94] M.J. Cooper and R. Nathans. *Acta Crystallographica A*, 24:619, 1968.

[95] M. Popovici. *Acta Crystallographica A*, 31:507, 1975.

[96] G.H. Lander. Neutron spectroscopy: the triple-axis spectrometer. 12. Oxford School on Neutron Scattering, University of Oxford, St. Annes College, Sep 2011.

[97] M. Monkenbusch. Time-of-flight spectrometers including nse. *Laboratory Course on Neutron Scattering*, Forschungszentrum Jülich, 2008.

[98] R. Ecclestone. *Neutron and X-ray spectroscopy*, chapter Time-of-Flight Inelastic Scattering. Springer, 2006.

[99] H. Bethe. *Z. Physik*, 71:205, 1931.

[100] L. Hulthen. *Arkiv Mat. Astron. Fysik*, 26A(11), 1938.

[101] C.N. Yang and C.P. Yang. *Phys. Rev.*, 150:321, 1966.

[102] C.N. Yang and C.P. Yang. *Phys. Rev.*, 150:327, 1966.

[103] G. Müller *et al. Phys. Rev. B*, 24:1429, 1981.

[104] H. J. Schulz. *Phys. Rev. B*, 34:6372, 1986.

[105] O.A. Starykh *et. al. Phys. Rev. B*, 55:14953, 1997.

[106] T. Barthel *et al. Phys. Rev. B*, 79:245101, 2009.

[107] D.C. Dender *et al. Phys. Rev. Lett.*, 79:1750, 1997.

[108] M. Arai *et al. Phys. Rev. Lett.*, 77:3649, 1996.

[109] A. Zheludev *et al. Phys. Rev. Lett.*, 89:197205, 2002.

[110] O.A. Starykh *et. al. Physica B*, 241:563, 1998.

[111] O.A. Starykh *et. al. Phys. Rev. Lett.*, 78:539, 1997.

[112] T. Barthel *et al.* arXiv:1212.3570v1, 2012.

[113] M. Karbach *et al. Phys. Rev. B*, 55:12510, 1997.

[114] R. Werner and A. Klümper. *Phys. Rev. B*, 64:174414, 2001.

[115] Y. Rahnavard and W. Brenig. Private Communication, 2013.

[116] K. R. Thurber *et al. Phys. Rev. Lett.*, 87:247202, 2001.

[117] J. P. Boucher *et al. Phys. Rev. B*, 13:4098, 1976.

[118] F.L. Pratt *et al. Phys. Rev. Lett.*, 96:247203, 2006.

[119] H. Maeter *et al. Journal of Physics: Condensed Matter*, 25:365601, 2013.

[120] T. Lancaster *et al. Phys. Rev. B*, 85:184404, 2012.

[121] N. Hlubek *et al. Phys. Rev. B*, 84:214419, 2011.

[122] J. Sirker *et al. Phys. Rev. Lett.*, 103:216602, 2009.

[123] J. Sirker *et al. Phys. Rev. B*, 83:35115, 2011.

[124] S. Grossjohann and W. Brenig. *Phys. Rev. B*, 81:12404, 2010.

[125] W. Marshall and R. D. Lowde. *Rep. Progr. Phys.*, 31:705, 1968.

[126] A.K. Bera *et al.* Presentation at SCES 2014, July 2014.

[127] C.G. Windsor and R.W.H. Stevenson. *Proc. Phys. Soc.*, 87:501, 1966.

[128] D.T. Teaney *et al. J. Appl. Phys.*, 37:1122, 1966.

[129] J.W. Stout and W.O.J. Boo. *J. Chem. Phys.*, 71:1, 1979.

[130] R.L. Carlin. *Magnetochemistry.* Springer, 1986.

[131] T. Hashimoto. *J. Phys. Soc. Jpn.*, 18:1140, 1963.

[132] S.R. Chinn *et al. J. Appl. Phys.*, 41:894, 1970.

[133] N. Achiwa. *J. Phys. Soc. Jpn.*, 27:561, 1969.

[134] J. Smith *et al. J. Chem. Phys.*, 53:418, 1970.

[135] D.A. Tennant *et al. Phys. Rev. Lett.*, 70:4003, 1993.

[136] A.C. Walters *et al. Nature Physics*, 5:867, 2009.

[137] M. Enderle *et al. Phys. Rev. Lett.*, 104:237207, 2010.

[138] G.E. Bacon and D.H. Titterton. *Zeitschrift für Kristallographie*, 141:330, 1975.

[139] K. Momma and F. Izumi. *J. Appl. Crystallogr.*, 44:1272, 2011.

[140] J.C. Bissey *et al. Solid State Communications*, 93:243, 1995.

[141] C.A. Beevers and H. Lipson. *Proc. R. Soc. A*, 146:570, 1934.

[142] T.H. Geballe and W.F. Giauque. *J. Am. Chem. Soc.*, 74:3513, 1952.

[143] J.C. Bonner and M.E. Fisher. *Phys. Rev.*, 135:A640, 1964.

[144] W.F. Giauque. *J. Chem. Phys.*, 53:3733, 1970.

[145] B. Fåk and M. Enderle. private communication.

[146] Local contact was Jacques Ollivier.

[147] Xavier Tonnon helped with the cryogenics.

[148] LAMP, the Large Array Manipulation Program. *www.ill.eu/data_treat/lamp/the-lamp-book/*.

[149] D. Richard *et al. J. Neutron Research*, 4:33, 1996.

[150] I. Bustinduy *et al. Nuclear Instruments and Methods in Physics Research Section A: Accelerators, Spectrometers, Detectors and Associated Equipment*, 546:498, 2005.

[151] P. Godfrey. Gamma, 2003.

[152] E. Ising. *Z. Physik*, 31:253, 1924.

[153] R. Peierls. *Mathematical Proceedings of the Cambridge Physical Society*, 32:477, 1936.

[154] L. Onsager. *Phys. Rev.*, 65:117, 1944.

[155] D. Gignoux *et al. Journal of Alloys and Compounds*, 191:139, 1993.

[156] J.C. Wright and H.W. Moos. *J. of Appl. Phys.*, 41:1244, 1970.

[157] C.J. Ellis *et al. J. Phys. C: Solid State Phys.*, 4:2937, 1971.

[158] J. Als-Nielsen. *Phys. Rev. Lett.*, 37:1161, 1976.

[159] D. Bitko *et al. Phys. Rev. Lett.*, 77:940, 1996.

[160] N. Hänni. *Crystal Structures and Magnetic Interactions of the Ising Type Co^{2+} Halides $RbCoCl_3$ and $Ba_4Co_2Cl_{12}$*. Master's thesis, Universität Bern, 2012.

[161] W.P. Lehmann *et al. J. Phys. C: Solid State Phys.*, 14:4655, 1981.

[162] A.B. Boeer. *Anisotropy in Molecular Magnetism - Magnetic Exchange Coupling of Octahedral Cobalt(II) Ions*. PhD thesis, University of Manchester, 2009.

[163] G. Nilsen. Private Communication, 2014.

[164] P. Pfeuty. *Annals of Physics*, 57:79, 1970.

[165] A. B. Zamolodchikov. *Int. J. Mod. Phys.*, A 4:4235, 1989.

[166] S.T. Carr and A.M. Tsvelik. *Phys. Rev. Lett.*, 90:177206, 2003.

[167] H.M. Ronnow *et al. Science*, 308:389, 2005.

[168] H. Shiba *et al. J. Phys. Soc. Jpn.*, 72:2326, 2003.

[169] S. Kimura *et al. Phys. Rev. Lett.*, 99:87602, 2007.

[170] K. Amaya *et al. J. Phys. Soc. Jpn.*, 59:1810, 1990.

[171] I.W. Johnstone *et al. Solid State Commun.*, 36:593, 1980.

[172] J. Villain. *Physica*, 79B:1, 1975.

[173] K. Hirakawa and H. Yoshizawa. *Journal of the Physical Society of Japan*, 46:455, 1979.

[174] H. Yoshizawa and K. Hirakawa. *Journal of the Physical Society of Japan*, 46:448, 1979.

[175] H.J. Mikeska. *J. Phys. C: Solid State Phys.*, 11:L29, 1978.

[176] J.K. Kjems and M. Steiner. *Phys. Rev. Lett.*, 41:1137, 1978.

[177] L.P. Regnault *et al. J. Phys. C: Solid State Phys*, 15:1261, 1982.

[178] J.P. Boucher *et al. J. Appl. Phys.*, 52:1956, 1981.

[179] N. Ishimura and H. Shiba. *Prog. Theor. Phys.*, 63:743, 1980.

[180] R. Jörke and U. Dürr. *J. Phys. C: Solid State Phys.*, 16:L1129, 1983.

[181] K. Maki. *Phys. Rev. B*, 24:335, 1981.

[182] F. Matsubara *et al. J. Phys.: Condens. Matter*, 3:1815, 1991.

[183] H. Shiba. *Prog. Theor. Phys.*, 64:466, 1980.

[184] F. Matsubara *et al. J. Phys. Soc. Jpn.*, 58:4284, 1989.

[185] N.P. Hänni, D. Sheptyakov, U. Stuhr, L. Keller, A. Cervellino, M. Medarde, M. Mena, E. Hirtenlechner, Ch. Rüegg, K. W. Krämer. Magnetic order in the quasi-one-dimensional ising system RbCoCl3. *submitted to Phys. Rev. B.*

[186] P. Fischer *et al. Physica B*, 276:146, 2000.

[187] P. Fischer *et al. Neutron News*, 11:19, 2000.

[188] Å. Engberg and H. Soling. *Acta Chem. Scand.*, 21:168, 1967.

[189] M. Mekata and K. Adachi. *J. Phys. Soc. Jpn.*, 44:806, 1978.

[190] D.J. Lockwood *et al. J. Phys. C: Solid State Phys.*, 16:6451, 1983.

[191] M. Mena. private communication.

[192] O. Koseki and F. Matsubara. *J. Phys. Soc. Jpn.*, 66:322, 1997.

[193] F. Matsubara *et al. Phys. Rev. Lett.*, 78:3237, 1997.

[194] O. Koseki and F. Matsubara. *J. Phys. Soc. Jpn.*, 69:1202, 2000.

[195] P. Manuel *et al. Phys. Rev. Lett.*, 103:037202, 2009.

[196] R.I. Bewley *et al. Nucl. Instr. and Meth. in Physics*, 637:128, 2011.

[197] Ch. Rüegg *et al. Phys. Rev. Lett.*, 95:267201, 2005.

[198] M. Troyer *et al. Phys. Rev. B*, 50:13515, 1994.

[199] K. Prsa *et al.* arXiv:1404.7398, 2014.

[200] L.P. English and H.B. Braun. private communication.

Acknowledgments

I'm nearly done... what is left is to thank everybody who made this thesis possible.

First of all I'd like to thank my supervisors Mechthild Enderle, Christian Rüegg and Joël Mesot. Each of you contributed essential parts to the work of the past three years. I am grateful for your continuous support and inspiration.

Many other people played a crucial part in my thesis. One of them is Bjorn Fåk, who was always prepared to answer my questions. A big thank you goes to the whole TAS group at ILL for creating such an enjoyable environment, amongst others Elisa, Jiri, Paul, Martin and, of course, Laurence. This applies also to the ILL directors, especially Helmut Schober, the science director. During my time at ILL I had the pleasure to share my office with a series of great office mates. Thanks to Adrien, Haifeng, Andre, Simon, Eron and Emanuel for being such pleasant colleagues and for never complaining when I put the heater on maximum. I am also very grateful to Philippe Chevallier, Olivier Losserand and Xavier Tonon, who provided invaluable support during experiments, and to Jacques Ollivier and Luis-Pierre Regnault for giving me the pleasure of working with them as local contacts. Sophie Rio from the library was always a big help when I was looking for a certain article, and the ladies from the pay office facilitated my life in France a lot by always being ready to answer my questions about all these forms one gets to fill out in France.

Another big thank you goes to Martin Mourigal, with whom I had the pleasure of working on $CuSO_4$*$5D_2O$. Nora Hänni grew the $RbCoCl_3$ single crystals. She turned out to be not only an inspiring coworker, but great company as well. The same can be said of Mattia Mena, who also taught me how to improve my Matlab code. I am grateful to Karl Krämer and Daniel Biner, with whom I worked on the $RbCoCl_3$ project. And thanks to Des McMorrow for inviting me to London to work with Mattia on this project. R. Bewley and T. Guidi were very helpful local contacts during the LET experiment. At ETH I am grateful to Professor Vaterlaus for agreeing to hold the chair of the doctoral examination.

At PSI Uwe Stuhr provided helpful advice as local contact on EIGER, and gave me lifts to the station when I missed the last bus to Brugg. I am also grateful to my office mate Simon Ward for sharing his vast knowledge of Matlab with me and wish him all the best for his thesis defense. Also at PSI I had the joy of having great office mates, who were, besides Simon, Simon Gerber, Martin Ruminy and Shang Gao. A big thank you also to everybody at LNS who always provided me with a

warm welcome in Villigen. Pamela Knupp earns a special mention, she has been incredibly helpful organizing my numerous trips to PSI.

In Grenoble I am also grateful to Ida, Diane, Alexis, Markus, Anton, Ingo, Eron and Goran for mental support, the good times and many nice evenings in the game cafe. Special thanks go to Goran for patiently answering all my questions about crystal fields and to Ingo for our nearly perfect food-symbiosis. You will both be missed. I am also grateful to Bernadette Delomenie, who provided me with a room to stay until I found a place in Grenoble. In Zürich this acknowledgment goes to my cousin Magdalena and her partner Johannes who always made me feel welcome at their place. I am also grateful to Karin for providing such a nice room in Wettingen where I could stay during my longer stints at PSI, and for being such enjoyable company.

Despite being more than 80 years old, my Grandma visited me in Grenoble every summer and even walked up to the Bastille(!). Her visits were always a happy occasion.

My Mum and Dad have been a seemingly infinite source of support. I am also grateful to my Dad for checking the spelling of the whole thesis, and to my Mum for her patience. My sister Bernadette proved again to be a great mental support in good and bad times, and also provided me with, by now, about half my wardrobe. So thanks for making me look good :-)

Even though my PhD had its ups and downs, it was an enjoyable experience. But the best thing which happened during this time was that I met Hamish.